On the complexity of energy landscapes

algorithms and a direct test of the Edwards conjecture

Stefano Martiniani

St John’s College
University of Cambridge

This dissertation is submitted for the degree of
Doctor of Philosophy

January 2017

On the complexity of energy landscapes
algorithms and a direct test of the Edwards conjecture

Stefano Martiniani

When the states of a system can be described by the extrema of a high-dimensional function, the characterisation of its complexity, *i.e.* the enumeration of the accessible stable states, can be reduced to a sampling problem. In this thesis a robust numerical protocol is established, capable of producing numerical estimates of the total number of stable states for a broad class of systems, and of computing the *a-priori* probability of observing any given state. The approach is demonstrated within the context of the computation of the configurational entropy of two and three-dimensional jammed packings. By means of numerical simulation we show the extensivity of the granular entropy as proposed by S.F. Edwards for three-dimensional jammed soft-sphere packings and produce a direct test of the Edwards conjecture for the equivalent two dimensional systems. We find that Edwards' hypothesis of equiprobability of all jammed states holds only at the (un)jamming density, that is precisely the point of practical significance for many granular systems. Furthermore, two new recipes for the computation of high-dimensional volumes are presented, that improve on the established approach by either providing more statistically robust estimates of the volume or by exploiting the trajectories of the paths of steepest descent. Both methods also produce as a natural by-product unprecedented details on the structures of high-dimensional basins of attraction. Finally, we present a novel Monte Carlo algorithm to tackle problems with fluctuating weight functions. The method is shown to improve accuracy in the computation of the 'volume' of high dimensional 'fluctuating' basins of attraction and to be able to identify transition states along known reaction coordinates. We argue that the approach can be extended to the optimization of the experimental conditions for observing certain phenomena, for which individual measurements are stochastic and provide little guidance.

To my wife Dilraj, love of my life.
Omnia Vincit Amor.

“The great tragedy of Science – the slaying of a
beautiful hypothesis by an ugly fact."
— Thomas H. Huxley, *Collected Essays,* **8**, *229*

Declaration

I hereby declare that this dissertation is the result of my own work and includes nothing which is the outcome of work done in collaboration except as declared in the preface and specified in the text. This dissertation is not substantially the same as any that I have submitted, or, is being concurrently submitted for a degree or diploma or other qualification at the University of Cambridge or any other University or similar institution except as declared in the preface and specified in the text. I further state that no substantial part of my dissertation has already been submitted, or, is being concurrently submitted for any such degree, diploma or other qualification at the University of Cambridge or any other University of similar institution except as declared in the preface and specified in the text. This dissertation contains fewer than 60,000 words.

Parts of this thesis are included in work that has either been published or is to be published:

1. S. Martiniani, K. J. Schrenk, J. D. Stevenson, D. J. Wales, D. Frenkel, *Turning intractable counting into sampling: computing the configurational entropy of three-dimensional jammed packings*, Phys. Rev. E **93**, 012906 (2016);

2. S. Martiniani, K. J. Schrenk, J. D. Stevenson, D. J. Wales, D. Frenkel, *Structural analysis of high dimensional basins of attraction*, Phys. Rev. E **94**, 031301 (2016);

3. S. Martiniani, K. J. Schrenk, K. Ramola, B. Chakraborty, D. Frenkel, *Are some packings more equal than others? A direct test of Edwards conjecture*, submitted, arXiv:1610.06328 (2016);

4. D. Frenkel, K. J. Schrenk, S. Martiniani, *Monte Carlo sampling for stochastic weight functions*, submitted, arXiv:1612.06131 (2016);

5. S.-W. Ye, S. Martiniani, K. J. Schrenk, J. D. Stevenson, D. Frenkel, E. Vanden-Eijnden, *Density propagation method for surveying energy landscape geometry*, submitted.

I have contributed to all aspects of research for papers 1-4. For paper 5 I contributed to designing the research and to developing the computational methods, I supervised the numerical experiments, contributed to the data analysis and to writing the manuscript. The mathematical basis of paper 5 was first derived by E. Vanden-Eijnden and the numerical experiments performed by S.-W. Ye as part of his Part III final year project.

Stefano Martiniani
January 2017

Acknowledgements

Thanks to my supervisor Daan Frenkel who is as great a human as he is a scientist. Working with a scholar of such stature, insight, vision, and not least wit, has been a privilege.

Thanks to David J. Wales for introducing me to the energy landscape and for his encouragements and guidance.

Thanks to Bulbul Chakraborty for her hospitality, guidance and for teaching me much about granular physics.

Thanks to Jacob D. Stevenson for teaching me many things (especially how to prioritize) and for pushing me to become a more careful scientist. Many were his contributions to the design and implementation of the vast software development project behind this thesis.

Thanks to Julian K. Schrenk for his essential contributions to every aspect of this work. Without Julian's contributions, persistence and words of encouragement this work would have not been possible. He has been a great collaborator and friend.

Thanks to Fabien Paillusson and Kabir Ramola for many fruitful discussions and for sharing their enthusiasm for this subject.

Thanks to my PhD co-authors and collaborators for making working an aesthetical pleasure: Shahar Amitai, Daniel A. Asenjo-Andrews, Andy Ballard, Raphael Blumenfeld, Bulbul Chakraborty, Daan Frenkel, Johannes Klicpera, Dhagash Mehta, Fabien Paillusson, Kabir Ramola, Levent Sagun, Julian K. Schrenk, Jacob D. Stevenson, Eric Vanden-Eijnden, David J. Wales, Shang-Wei Ye, Alessio Zaccone.

Thanks to the whole Cambridge Theoretical Chemistry group, office 360 and the machine learning and algorithms reading clubs for many useful interactions.

Thanks to Catherine Pitt and the IT support team for their assistance.

Thanks to the Gates Cambridge Trust, St John's college, the Department of Chemistry and the Frenkel research lab for financial support.

Thanks to Brian O'Regan, Svyatoslav Kondrat and John Seddon for first encouraging my young mind to pursue a career in research.

Thanks to my wonderful wife Dilraj for her love, care and support during these years and for always being by my side. I look forward to our future together.

Grazie ai miei genitori Gabriele e Nunzia, a mia sorella Daniela, ai miei nonni e a tutta la mia famiglia per il loro supporto incondizionato nonostante le grandi distanze che ci separano.

Grazie a Salvatore, per essere l'amico che è, e per le tante avventure vissute assieme.

Thanks to all my friends for being part of my life.

Table of contents

List of figures

List of tables

Nomenclature

Roman Symbols

A_d	d-dimensional asphericity factor
$\mathcal{B}$	Biased (observed) distribution
$\mathcal{C}(c)$	Intercept of power law relationship between pressure and basin volume (per particle)
d/D	Number of dimensions
Δt	Time step
$F(f)$	Basin's negative log-volume (per particle)
F_{har}	Harmonic reference dimensionless free energy
f_T	Fraction of unterminated trajectories
$\mathcal{H}$	Hamiltonian
H	Hessian matrix
J	Jacobian matrix
k_E	'Boltzmann-like' constant in definition of granular entropy
k_i	i-th harmonic coupling constant in TI
$k_{\max}$	Maximum harmonic coupling constant in TI
L	Length-scale ($N^{1/d}$)
λ_i	i-th eigenvalue
N	Number of particles

$\hat{\mathbf{n}}$	Surface normal vector
N_T	Number of trajectories
p_i	Probability of observing the *i*-th packing
p_J	Probability of jamming
Q_6	Bond orientational order parameter
$\mathcal{R}$	Overlap between basin volume and reference volume
R/r	Distance from minimum
R_γ	Radius of reference volume
W	Rosenbluth weight
$\mathcal{R}_x$	Set of random numbers of class x
S_γ	Surface area of γ
$S_B(s_b)$	Boltzmann entropy (per particle)
$S_G(s_G)$	Gibbs entropy (per particle)
$\mathcal{U}$	Unbiased distribution
U/u	Potential energy function
$\mathcal{W}$	Edwards' volume function
V_{box}	Volume of enclosing box with periodic boundary conditions
v_i	Volume of the *i*-th basin of attraction
$\mathcal{V}_J$	Total available volume of configurational space tiled by the basins of attraction of jammed configurations
Z	Partition function
z	Average contact number

Greek Symbols

$\hat{\alpha}$	Inverse angoricity tensor

$\chi_P(\chi_\Lambda)$	Extensive fluctuations of relative (log) pressures
$\hat{\sigma}$	Covariance matrix
σ_x^2	Variance of x
σ_{xy}^2	Covariance of x,y
Δ	Displacement vector
$\partial\gamma$	Surface of reference volume
$\mathrm{d}\sigma$	Element of surface
η	Polydispersity (Chapt. 4), relative error (Chapt. 5)
Γ	Basin of attraction manifold
γ	Reference manifold
κ^{-1}/λ	Slope of power law relationship between pressure and basin volume
Λ	Logarithm of the pressure
μ_x	Mean of x
ν	Correlation length critical exponent
$\nu_{\partial\gamma}$	Projected volumetric density onto reference surface
Ω	Total number of jammed packings
ω	Biasing weight
ϕ	Volume fraction
ϕ^J	Volume fraction at which (un)jamming occurs
ϕ^*	Equiprobability volume fraction
ρ	Density
ρ_{xy}	Linear correlation coefficient for x,y
$\hat{\Sigma}$	Force-moment (stress) tensor
$\hat{\Phi}$	Edwards' force-moment tensor function

τ_+	Time at which trajectory crosses $\partial\gamma$
$\Theta_\Gamma/\mathcal{O}$	Oracle
Θ_J	Jamming Satisfaction Problem constraint function
Θ	Parameter of density propagation method
X	Compactivity

Subscripts

acc	Acceptance
B	Backbone
conv	Convergence
ens	Ensemble
ex	Excess
gen	Generation
har	Harmonic
id	Ideal
iso	Isostaticity
n	New
nr	Non-rattlers
o	Old
poly	Polydisperse
sel	Selection
sig	Sigmoid
tr	Transition state
wr	Waste-recycling

Other Symbols

$\setminus$	Set theoretic difference

Acronyms / Abbreviations

BCa	Bias-corrected and accelerated
CBMC	Configurational-bias Monte Carlo
CD	Ceperley Dewing
CDF (c.d.f.)	Cumulative distribution function
CG	Conjugate gradient
CM	Centre of mass
CPU	Computing processing unit
CS	Carnahan Startling
CSK	Carnahan Startling Kolafa
det	Determinant
DOS	Density of states
EC	Einstein crystal
ECM	Einstein crystal method
EFE	Energy function evaluations
FCC	Face-centered cubic
FIRE	Fast inertial relaxation engine
FNE	Force network ensemble
GL	Gauss Lobatto
HS	Hard spheres
HS-WCA	Hard sphere - Weeks Chandler Anderson
KDE	Kernel density estimate
LSA	Lubachevsky-Stillinger algorithm

MBAR	Multi-state Bennet acceptance-ratio method
MBV	Mean basin volume
MCD	Minimum covariance determinant
MC	Monte Carlo
MCMC	Markov chain Monte Carlo
ML	Maximum likelihood
MMSE	Minimum mean square error
PCA	Principal component analysis
PDF (p.d.f.)	Probability density function
PEL	Potential energy landscape
PES	Potential energy surface
PT	Parallel tempering
RCP	Random close packing
SS	Soft spheres
SYH	Santos Yuste Haro
TI	Thermodynamic integration
Tr	Trace
WCA	Weeks Chandler Anderson
WHAM	Weighted histogram analysis method

Chapter 1

Introduction

1.1 Counting the uncountable

Predicting the state of the physical world is difficult because the number of possible realisations is so large. If we could compute such states and the probability of observing them, we would be able to quantify the likelihood of a wide range of phenomena. In some cases (e.g. in the statistical mechanical description of the formation of a crystal) we can perform such calculations, but in others (e.g in estimating the likelihood of the emergence of life, or even of the formation of a universe like ours), we cannot. But in the latter examples this may also be due to the fact that the question is ill-posed. However, even in the cases where we know in principle how to identify all possible states of a system, the number of states involved is so large that a full enumeration would *greatly* exceed the 'computational capacity' of the universe [1] – namely the maximum amount of information that the universe can register or the maximum number of operations that has performed over its history – and, therefore, would not be possible.

When the states of a system can be described by the invariant stable structures of some dynamics, be it the extrema of a high-dimensional function that can be reached by steepest descent, or the fixed points and limit cycles of a generic dynamical system, the enumeration problem can be reduced to a sampling one: The 'uncountable' number of possible states can be estimated by sampling a few of these states at random and measuring the average size of their basin of attraction, that is the set of all initial conditions leading to a particular stable structure. Moreover, since the probability of sampling a state is related to the size of its basin of attraction, estimating the probability of an unlikely – but known – state becomes equivalent to measuring the (high-dimensional) volume of its basin of attraction.

To illustrate the principle, imagine you were asked to estimate the number of buildings in a large city by looking at an aerial map. Since counting hundreds of thousands of buildings is out of the question, we turn the counting problem into a sampling one: we randomly drop our pencil onto the map and record the area of the building on which the pencil lands. Clearly, the probability of sampling a building is proportional to the area it covers and the observed distribution of areas will be biased. After collecting several samples, we can estimate the (unbiased) average size of the buildings by a weighted sum of the areas, where each element of the sum is weighted inversely proportional to its value. Finally, the total number of buildings can be estimated dividing the total urban area by the thus obtained average area of the buildings that tile it. This principle is completely general and it extends to any problem that aims to find the number of stationary points of a high-dimensional scalar cost function or stable structures of a dynamical system. One such cost function is the potential energy of a system, defining the *energy landscape* (or potential energy surface).

Enumerating the number of solutions or stationary points, and their distribution, for certain classes of random functions, is a classical problem in mathematics and statistics [2–15]. In statistical physics, *ad hoc* numerical and theoretical methods have been developed in the realms of random Gaussian and polynomial fields [16–24]. In this sense, particular attention has been devoted to the mean-field p-spin spherical model of a spin glass with quenched disorder [25–29]. A related area is the computation of the configurational contribution to the entropy of structural glasses [30, 31].

While in this work we focus mainly on the study of soft-sphere packings [32–36], the significance of the approach extends to the study of biological molecules [37, 38], marginally stable glasses [39, 40], dynamical system [41, 42], machine learning [43–48], and even cosmology [49–53] and string theory [54–56].

1.2 On Edwards' theory of powders

In the late 1980s Sir Sam Edwards proposed that a formalism analogous to classical statistical mechanics could be formulated to describe the states of a disordered granular material. In his proposition, which appeared under the title "Theory of powders" [57], Edwards stated that a statistical mechanics of granular matter could be derived on the basis that powders can be "*completely defined by a very small number of parameters [such as their density] and can be constructed in a reproducible way [say by tapping or shaking]*". Moreover, because granular media are typically made of a very large number of components, a statistical description would seem appropriate, and we may assume that "*when N grains occupy a volume V they do so in such a way that all configurations are equally weighted. We assume this; it is the analog of the ergodic hypothesis of conventional thermal physics*" [58]. In a succinct, and at times intuitive style[1] – not to be confused with lack of clarity, but rather originating from the intention of developing the simplest theory possible for granular powders [60] – Edwards had dared to describe a many-body, strongly interacting and out-of-equilibrium system – the archetype of complexity – using the standard tools of Gibbsian equilibrium statistical mechanics.

1.2.1 The volume ensemble

Edwards' great insight was to propose that the collection of all stable packings may play the role of an 'ensemble' and that a statistical mechanical formalism would result if one assumed all packings to be equally likely. Hence, drawing the analogy with classical 'Gibbsian' statistical mechanics, the Hamiltonian $\mathcal{H}(\{\boldsymbol{p}_i,\boldsymbol{x}_i\})$ corresponding to the total energy of the (closed) system, was replaced by a volume function $\mathcal{W}(\{\boldsymbol{x}_i,\hat{\boldsymbol{t}}_i\})$ corresponding to the volume of the system as a function of the particle positions $\boldsymbol{x}_i$ and the orientations $\hat{\boldsymbol{t}}_i$. One can then write the microcanonical density of states as

$$e^{-S_B(V)}\delta(V-\mathcal{W}(\boldsymbol{q}))\Theta_J(\boldsymbol{q}), \tag{1.1}$$

where S is the granular entropy of the system

$$S_B(V)=k_E\ln\Omega(V) \tag{1.2}$$

and

$$\Omega(V)=\int\delta(V-\mathcal{W}(\boldsymbol{q}))\Theta_J(\boldsymbol{q})\mathrm{d}\boldsymbol{q}, \tag{1.3}$$

is the total number of packings at volume V, and the B subscript stands for 'Boltzmann-like'. $\Theta_J(\boldsymbol{q})$ enforces that packing $\boldsymbol{q}\equiv\{\boldsymbol{x}_i,\hat{\boldsymbol{t}}_i,\boldsymbol{f}_{ij}\}$, where $\boldsymbol{f}_{ij}$ are the interparticle forces, is a solution to the "Jamming Satisfaction Problem" [59] or, in other words, the requirement that the constraints of statical mechanical equilibrium are satisfied; these are: force and torque balance, Newton's 3rd law, positivity of forces and, for frictional packings, Couloumb's law of friction. The latter two, being inequality constraints, are notoriously difficult to implement [61]. Note that the conjectured flat measure "à la Edwards" stems precisely from the definition of Θ_J. Unlike in thermal statistical mechanics, where (inverse) temperature and energy are measured in different units (if only statistical mechanics had been developed earlier!), k_E is not necessary but "*makes the equation more recognisable*" [59], in practice we assume $k_E=1$ everywhere.

---

[1] By his own admission, Edwards writes [59] "*[this work] is dedicated to Elliot Lieb, my first research student, who is as rigorous and accurate a worker as I am vague; but all sorts are needed in a world.*"

When the system is driven by external disturbances, *e.g.* vibrations, the density (volume) of the granular system will approach a steady state and enter a reversible branch where, by modulating the magnitude of the external disturbance, the system can move between two characteristic densities $\phi_{\text{min}}^{(\text{RCP})}$ and $\phi_{\text{max}}^{(\text{RCP})}$ and, at each point along the branch, fluctuate around a stationary value [62]. Thus, it seems natural to move to a canonical description of the granular system (although Edwards' proposition came a decade earlier than these experiments), where the canonical distribution takes the form

$$p(\boldsymbol{q}) = \frac{1}{Z(V)} e^{-\mathcal{W}(\boldsymbol{q})/X} \Theta_J(\boldsymbol{q}) \tag{1.4}$$

and the partition function is

$$Z(V) = e^{-S_B(V)+V/X} = \int e^{-\mathcal{W}(\boldsymbol{q})/X} \Theta_J(\boldsymbol{q}) \mathrm{d}\boldsymbol{q}, \tag{1.5}$$

where the temperature-like variable X, named *compactivity*, is defined such that

$$\frac{1}{X} = \frac{\partial S_B(V)}{\partial V}. \tag{1.6}$$

The compacitivity X is at its minimum (maximum) when the system is as closely (losely) packed as possible. For a system of monodisperse spheres, $X \to \infty$ at random loose packing and $X \to 0$ for the cubic close-packed (fcc) crystal.

1.2.2 The laws of granular thermodynamics

The parallelism with classical thermodynamics can be taken further and a set of laws of granular thermodynamics can be postulated [63]

Zeroth law. The basis of all thermometry, it establishes that if two systems A and B are in thermal equilibrium such that $X_A = X_B$, and A is also in thermal equilibrium with a third body C such that $X_A = X_C$, then a consistent definition of temperature requires that $X_B = X_C$.

First law. This can be expressed in differential form as

$$\mathrm{d}V = X\mathrm{d}S - \mathrm{d}A, \tag{1.7}$$

where dA has the dimensions of volume and is the analogue of the work done on the system. It is not clear how one should distinguish between the two terms on the right-hand side of Eq. (1.7) in a granular system.

Second law. Any irreversible process in a granular system is associated with an increase in granular entropy, such that

$$\mathrm{d}S \geq 0. \tag{1.8}$$

The second law proclaims the central position of entropy in Edwards' statistical mechanics.

Third law. In the limit of absolute zero temperature $X \to 0$, the system achieves a unique state with zero entropy. For a system of monodisperse hard spheres, this corresponds to the perfect crystal, however for a generic granular system one expects some residual entropy such that

$$\lim_{X \to 0} S = const. \tag{1.9}$$

A derivation of the second law was sketched via the H-theorem by defining an appropriate Boltzmann equation for dense granular packings [59].

1.2.3 The stress volume ensemble

Soon it was realised that volume alone was not sufficient to describe the state of the system and that the stress $\hat{\Sigma}$ exerted on the boundary must play a role [64–66]. Furthermore, in the presence of friction the forces between particles cannot be deduced from the particles' positions and orientations alone, and interparticle forces need to be specified for each microstate. Hence, the system subject to constraints on both V and $\hat{\Sigma}$ must have an entropy $S(V,\hat{\Sigma})$ defined via a generalised microcanonical density of states

$$e^{-S_B(V,\hat{\Sigma})}\delta(V - \mathcal{W}(\boldsymbol{q}))\delta(\hat{\Sigma} - \hat{\Phi}(\boldsymbol{q}))\Theta_J(\boldsymbol{q}) \tag{1.10}$$

such that

$$S_B(V,\hat{\Sigma}) = \ln\Omega(V,\hat{\Sigma}) = \ln\int \delta(V - \mathcal{W}(\boldsymbol{q}))\delta(\hat{\Sigma} - \hat{\Phi}(\boldsymbol{q}))\Theta_J \mathrm{d}\boldsymbol{q}, \tag{1.11}$$

where the macroscopic force-moment tensor is

$$\hat{\Phi}(\boldsymbol{q}) = \sum_{i=1}^{N}\sum_{j=1}^{z_i} \boldsymbol{r}_{ij} \otimes \boldsymbol{f}_{ij}, \tag{1.12}$$

$\boldsymbol{r}_{ij}$ is the contact vector between particles i and j and the inner sum is over all z_i contacts of particle i.

The generalised canonical distribution is therefore

$$p(\boldsymbol{q}) = \frac{1}{Z(V,\hat{\Sigma})} e^{-\mathcal{W}(\boldsymbol{q})/X - \mathrm{Tr}[\hat{\alpha}\hat{\Phi}(\boldsymbol{q})]} \Theta_J(\boldsymbol{q}) \tag{1.13}$$

and the partition function is

$$Z(V,\hat{\Sigma}) = e^{-S_B(V,\hat{\Sigma}) + V/X + \mathrm{Tr}(\hat{\alpha}\hat{\Sigma})} = \int e^{-\mathcal{W}(\boldsymbol{q})/X - \mathrm{Tr}[\hat{\alpha}\hat{\Phi}(\boldsymbol{q})]} \Theta_J(\boldsymbol{q}) \mathrm{d}\boldsymbol{q}, \tag{1.14}$$

where we have introduced the inverse *angoricity* tensor, another temperature-like variable, defined as

$$\hat{\alpha} = \frac{\partial S_B(\hat{\Sigma})}{\partial \hat{\Sigma}} \tag{1.15}$$

Many interesting results have been obtained by restricting theoretical treatment to only the volume or the stress ensemble (by assuming decoupling in certain limits, such as constant volume or constant pressure). However, in general, Eq. (1.14) is a function of both compactivity X and inverse angoricity $\hat{\alpha}$, which are interdependent, and it cannot therefore be factorised in terms of a pure volume and a pure stress partition function, $Z(X,\hat{\alpha}) \neq Z(X)Z(\hat{\alpha})$ [67].

1.2.4 The rheology of powders

One of the main aims of Edwards statistical thermodynamics of granular materials was to arrive at a formalism that would make it possible to derive the equations that describe the flow of powders. The original idea was to derive the equations of flow for a granular system by complementing the continuity equation and the equations of motion with an *ad-hoc* energy equation (analogous to the heat-conduction equation) of the form [60]

$$\frac{\partial X}{\partial t} + L(X) = F(\hat{e}), \tag{1.16}$$

where $\hat{e}$ is the deformation tensor, and a constitutive equation describing the stress tensor as a function of the deformation tensor and the system's thermodynamic state, that depends on the density ϕ and the compactivity X. The flow could then be modelled within a simple ϕ, $\boldsymbol{v}$, X framework.

An alternative approach to understand the dynamics of granular materials using a formalism analogous to that of the Boltzmann and Fokker-Plank equation was also developed, which allowed to derive under simplifying assumptions a relation between the diffusion constant and the compactivity [59, 65].

Edwards' fundamental idea was that the dynamics of slowly driven granular systems are controlled by the statistical properties of the jammed states. It seems plausible that if the system is driven slowly enough, then the transition from one jammed state to another will depend on the properties of the jammed states, in close analogy to well known models of glassy dynamics for thermal systems [68–70]. While still in its infancy, experimental and theoretical work in this avenue is promising [61, 71, 72].

1.2.5 Edwards' contested hypotheses: ergodicity and equiprobability

Edwards' formulation of granular statistical mechanics builds on two bold hypotheses, namely the assumptions of ergodicity and of equiprobability of all jammed states. Both hypotheses are at the origin of great controversy about the legitimacy of Edwards' proposal.

Assuming ergodicity became natural following the seminal work of "*the Chicago group*" [62] demonstrating, in an experimental study of the compaction of spherical glass beads as a function of tapping intensity, the existence of an irreversible and reversible branch in the response. After an initial transient response, the system reaches a steady state and as the tapping intensity is varied the system retraces a stable branch in the density versus tapping intensity plane. While these results were validated by a number of experimental [73–75] and theoretical [76–81] studies, their interpretation was challenged by studies testing ergodicity by directly comparing time averages with ensemble averages, which were found to be in agreement [82–85]. However, a more detailed analysis comparing identical realizations of the system prepared with the same preparation protocol, shows that the replicas do not sample the same stationary distributions [86–90]. The failure of ergodicity seems to be connected to the fraction of persistent contacts *viz.* contacts that do not break upon repeated disturbance [90], suggesting that the protocol might not allow the system to visit all regions of phase space, and therefore breaks ergodicity.

The hypothesis of equiprobability of jammed states, also known as Edwards' conjecture, was inspired by the analogous assumption of J. Willard Gibbs that at fixed total energy, the states of an equilibrium (closed) system are equally likely to be observed [91]. The unsophisticated way of testing the conjecture is by generating all possible packings and measuring the frequency with which each packing is visited. The problems with this approach should be obvious, the number of possible states is exceedingly large for all but the smallest system sizes and, particularly in experiments, it is extremely difficult to carefully control the effects of protocol, geometry and friction. Following the brute-force approach, simulation studies enumerating the number of minima in the energy landscape of small systems of soft frictionless disks, found highly non-uniform frequency distributions [85, 92]. These results for very small numbers of particles were corroborated by experiments [93]. On the other hand, exact results for a simplified 2-dimensional system of hard disks confined between two parallel hard walls confirmed Edwards' assumption and showed that two systems at contact will maximise entropy by attaining equal compactivities [94].

The resolution of this point is important as this assumption underlies the very definition of entropy proposed by Edwards, see Eq. (1.11). A significant step forwards was taken when Frenkel and co-workers introduced a numerical method with complete control on the sampling bias introduced by the protocol and capable of computing the *a-priori* probability of observing a jammed packing without recurring to extensive simulations [32, 34]. The numerical calculations of the total number of packings for a system of up to 128 soft disks confirmed that, for jammed packings at fixed volume fraction greater than the jamming density, equiprobability breaks down. Nonetheless, when properly defined, Edwards' definition of granular entropy is meaningful and extensive. Specifically, they propose a 'Gibbs-like' definition of entropy of the form

$$S_G = -\sum_{i=1}^{\Omega} p_i \ln p_i - \ln N! \tag{1.17}$$

where where p_i is the probability of observing packing i and the division by $N!$ ensures that two systems in identical macrostates are in equilibrium under exchange of particles [95–97]. The approach of Refs. [32, 34] exploited the fact that each soft sphere packing is a minimum energy configuration in an energy landscape. By measuring the size of the basin of attraction, they were able to compute the probability of a particular packing to occur, as well as the total number of packings. The results of the computation of the number of soft disks demonstrated that, at last, Edwards' conjecture could be tested conclusively.

1.3 Contributions of this thesis

Firstly we address the question of whether the conclusions of Refs. [32, 34] are valid in three-dimensions. In Chapt. 2 we perform the first direct computation of the number of packings for systems of three-dimensional soft spheres, and test whether Edwards' definition of granular entropy is meaningful. Going from two to three dimensions required substantial algorithmic improvements: the new algorithm implementation was computationally $\mathcal{O}(100)$ more efficient than the one used by Asenjo *et al.* [34], thus making the calculations tractable. Nonetheless, the calculations required hundreds of years of cpu-time.

In Chapt. 2 we also present a power-law relation between the basin volume and the pressure (energy) of a soft sphere packing, suggesting a hierarchical organization of the energy landscape, where low-energy minima have large basin volumes and high-energy minima have small basin volumes. This expression allowed us to compute the granular entropy at fixed volume and stress. The power-law exponent is a good measure of the strength of the correlation between a packing's structural parameters, such as the pressure, and its basin volume. This fact will be essential to test Edwards' conjecture in Chapt. 3.

When packings of soft disks are above the jamming density – the point where the system goes from a fluid to a disordered solid – they have been shown not to be equiprobable [32, 34], in clear violation of Edwards' conjecture. However, to our own surprise, in Chapt. 3 we are able to demonstrate that the conjecture becomes correct precisely at the (un)jamming threshold, which is the point that Edwards had taken into consideration. Furthermore, we find that if both stress and volume are taken into account then equiprobability holds beyond jamming, in what is known as the Edwards' stress-volume ensemble. In Chapt. 3 we also show that the relative pressure fluctuations are a suitable order parameter to identify the (un)jamming transition.

As argued in the opening, the problem of the enumeration of stationary points of a scalar cost function or stable structures of a dynamical system, as well as the characterisation of the geometry of their basins of attraction, is of broad interest. To this end, in a 2006 perspective article, Strogatz and collaborators put forward the characterization of the 'sync basin' volume as a new line of research to the non-linear dynamics community [41]. They write: "*the entire topic of basins is something of an enigma in dynamical systems theory [. . .] what we do not know is how to compute the total volume or "measure" of a basin, which is what determines the probability that a random initial state will be drawn toward the associated attractor.*" Much of this work is dedicated precisely to the problem of measuring, and characterising, the volume of basins of attraction in the energy landscape.

The remainder of this thesis is dedicated to a discussion of the algorithms *per se*. We present two novel techniques capable of measuring high dimensional volumes. In Chapt. 4 we present a method that relies on the multi-state Bennett acceptance-ratio method [98] and that allows a more accurate computation of the volume of basins of attraction, as well as yielding unprecedented insight into the structural properties of these high-dimensional bodies. We illustrate the method by studying the effect of structural disorder on the shape of the basins of attraction of soft sphere packings.

Because we evaluate the basin volume by performing a random walk *within* its body, we are required to test at each step of the walk if we have left the basin, in which case we reject the move. At present, the major obstacle to the scalability of the method is that the only way to test whether we have left the basin is by performing a full energy minimisation. This is wasteful because the trajectory of the path of steepest descent does not contribute in any way to the volume computation. In Chapt. 5 we present a density propagation method that addresses this issue by computing the basin volume precisely from the steepest descent trajectories. In a proof-of-principle demonstration, the technique is used to compute the volumes of Gaussian mixture potentials and of a one-dimensional XY-model of eight spins. The method also yields unique information on the geometry of high dimensional basins of attraction.

Finally, in Chapt. 6 we show that it is possible to construct a rigorous Monte Carlo algorithm that samples points in space proportionally to the average of a fluctuating weight function. The method is successfully used to measure the volume of basins of attraction that are fluctuating and therefore are only determined on average. This is a common situation, for instance, in machine learning when the “training” is performed by stochastic optimisation. We also demonstrate that the technique can be used to locate transition states along a known reaction coordinate. We argue that this new approach has the potential to transform the methodology of a certain class of high-throughput experiments.

Chapter 2

Turning intractable counting into sampling: Computing the configurational entropy of three-dimensional jammed packings

We present a numerical calculation of the total number of disordered jammed configurations Ω of N repulsive, three-dimensional spheres in a fixed volume V. To make these calculations tractable, we increase the computational efficiency of the approach of Xu *et al.* (Phys. Rev. Lett. **106**, 245502 (2011)) and Asenjo *et al.* (Phys. Rev. Lett. **112**, 098002 (2014)) and we extend the method to allow for the computation of the configurational entropy as a function of pressure. The approach that we use computes the configurational entropy by sampling the absolute volume of the basins of attraction of stable packings in the potential energy landscape. We find a surprisingly strong correlation between the pressure of a configuration and the volume of its basin of attraction in the potential energy landscape. This relationship is well described by a power law. Our methodology to compute the number of minima in the potential energy landscape should be applicable to a wide range of other enumeration problems in statistical physics, string theory, cosmology and machine learning, that aim to find the distribution of the extrema of a scalar cost function that depends on many degrees of freedom.

— This chapter is based on Ref. [35]: Stefano Martiniani, K. Julian Schrenk, Jacob D. Stevenson, David J. Wales, and Daan Frenkel, Phys. Rev. E **93**, 012906 (2016)

2.1 Introduction

Many questions in physics are easy to pose but difficult to answer. One such question is: how many microscopic states of a given system are compatible with its macroscopic properties? In statistical mechanics, knowledge of this number allows us to compute the entropy, and thereby predict the macroscopic properties of a system from knowledge of the interaction between atoms or molecules.

In granular matter we can similarly ask how many microstates are compatible with a given set of macroscopic properties. However, the computation of the corresponding absolute entropy has thus far proven to be extremely challenging. Without such knowledge, it is not possible to explore the analogies and differences between granular and Boltzmann entropy. Being able to compute the configurational entropy is therefore clearly important. The more so given that granular materials are ubiquitous in everyday life (sand, soil, powders). Many industrial processes involve granular materials. In the natural world, the Earth's surface contains vast granular assemblies such as dunes, which interact with wind, water, and vegetation [99]. Packings of particles that are soft or biological in nature, such as cells, hydrogels and foams are also known to undergo jamming [100] and their behaviour to be "granular" *viz.* not subject to thermal motion. Moreover, as glasses and granular materials share many properties it has been proposed that their physics may be controlled by the same underlying principles [101].

The study of granular materials is complicated by the fact that these materials are intrinsically out-of-equilibrium. In fact, thermal motion plays no role in granular matter. It maintains its configuration unless driven by external forces. As a consequence, the properties of granular materials depend upon their preparation protocol.

Granular materials are athermal and cannot therefore be described by statistical mechanics. However, these materials can exists in a very large number of distinct states and this fact inspired Edwards and Oakeshott [57] well over two decades ago to propose a statistical-mechanics-like formalism to describe the properties of granular matter. In its original version, the Edwards theory assumed that all mechanically stable configurations ('jammed' states) are equally probable and that the logarithm of the number of these states plays a role similar to that of entropy. In this theoretical framework, the volume of the system and its *compactivity* (*i.e.* the derivative of volume with respect to the configurational entropy) are the analogues of the energy and temperature in thermal systems, see Sec. 1.2.1 for a full discussion.

In the absence of explicit calculations (or measurements) of the absolute configurational entropy, a direct test of the Edwards hypothesis has proven difficult, and different authors have arrived at different conclusions based on direct and indirect tests in either simulations [92, 102–104] or experiments [93, 105, 106]. In addition, alternative definitions of entropy have been proposed to characterise the complexity of granular systems while circumventing explicit enumeration of states [107, 108].

Numerous tests of the Edwards volume ensemble have focused on the determination of the compactivity [67, 86, 109–115]. However, the role of compactivity as a temperature-like quantity is problematic as Puckett and Daniels [61, 116] have shown that it does not satisfy the equivalent of the zero-th law of Thermodynamics - the law that is the basis of all thermometry.

Edwards' theory has been generalised to include the distribution of stresses within the system through the force-moment tensor [65, 66, 117, 118] and another analogue of temperature emerged, known as *angoricity*, which is a measure of the change in entropy with stress, see Sec. 1.2.3 for a detailed description. The experiments by Puckett and Daniels [116] showed that angoricity, unlike compactivity, is a temperature-like quantity as it satisfies the zero-th law.

To date only a few examples of numerical tests of the generalised Edwards ensemble are available [66, 84, 85, 116]. Numerical tests of the stress ensemble focus on systems of soft spheres near jamming where the compactivity $X \to \infty$ and fluctuations in volume are negligible compared to stress fluctuations [66, 118]. Wang *et al.* [84, 85] proposed a unified test that compared ensemble averaged results over volume and stress with predictions for the jamming transition, finding agreement; we note, however, that in the latter approach the results rely significantly on the equiprobability assumption.

When the system is composed of very stiff grains, or is close to jamming, any small deformation will lead to a large change in the contact forces. In these limits the geometric and the force degrees of freedom can be decoupled, giving rise to the force network ensemble (FNE) [119]. In this framework, force networks are constructed on a given geometry and each force state is assumed to be equiprobable. The FNE has been utilised as a testing ground for statistical frameworks [120–122].

More than two decades after its introduction many fundamental questions concerning the Edwards hypothesis remain unanswered. This unsatisfactory state of affairs is at least partly due to the fact that no efficient methods existed to measure or compute the absolute configurational entropy directly. Until recently, the only way to determine the configurational entropy was by direct enumeration of the distinct jammed states of a system. This method is inefficient and cannot be used for systems that contain more than 10-20 particles. Over the past few years, the situation on the numerical front has changed: recent numerical work by Asenjo *et al.* [34, 89], based on an approach introduced by Xu *et al.* [32], has demonstrated that it is possible to compute the number of distinct jammed states of a system, even when this number is far too large (e.g. 10^{250}) to allow direct enumeration. The approach of Refs. [32,

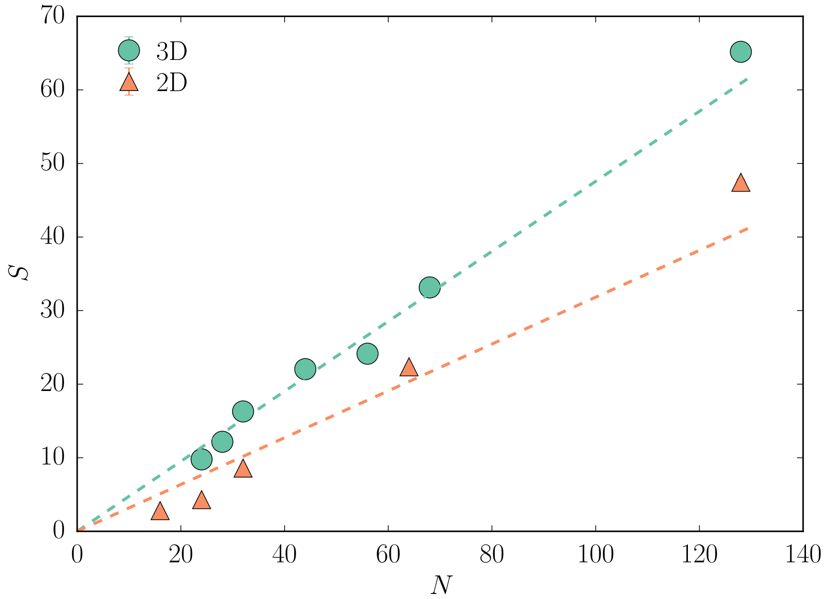

Fig. 2.1 Entropy as a function of system size N for two (Ref. [34]) and three-dimensional (this work) jammed sphere packings. Dashed curves are lines of best fit of the form $S = aN$.

34, 89] replaces an intractable enumeration problem by a tractable scheme to sample the (absolute) volume of the basins of attraction of stable states in the potential energy landscape.

We note that the geometrical structure of the basins of attraction of jammed states had been studied by O'Hern and co-workers [92, 123, 124]. O'Hern also reported direct enumeration estimates of the number of jammed states of small systems. A rather different technique ('basin sampling') to count the number of energy minima in the potential energy landscape of small clusters had been reported by Wales and co-workers [125, 126].

We note that, for the system (and protocol) considered by Asenjo *et al.*, not all packings are equally probable. However, as shown in Ref. [34], the equal-probability hypothesis is not needed to arrive at a meaningful definition of an extensive granular entropy, Eq. (1.17).

We stress that, even though the approach of Refs. [32, 34, 89] allows to solve enumeration problems which were far from possible using direct enumeration, it is still computationally expensive. Thus far, it had only been applied to two-dimensional packings. Substantial 'technical' improvements were needed to make the method fast enough to deal with three-dimensional systems.

In this chapter, we present the first enumeration of the number of jammed packings for three-dimensional systems consisting of up to 128 soft spheres. A direct comparison of the entropy measured as a function of system size for two and three-dimensional jammed sphere packings is shown in Fig. 2.1. Furthermore we show how our improved procedure

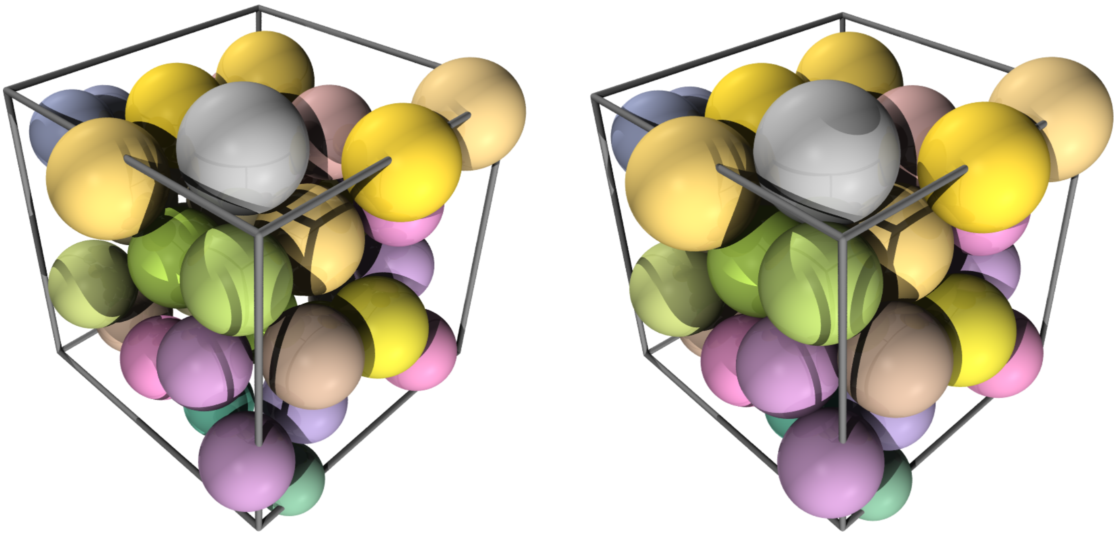

Fig. 2.2 Hard sphere fluid at $\phi_{\mathrm{HS}} = 0.5$, left, and HS-WCA jammed packing at $\phi_{\mathrm{SS}} = 0.7$, right, for a system of 44 polydisperse hard spheres with mean radius $\langle r_h \rangle = 1$ and standard deviation $\sigma_{\mathrm{HS}} = 0.05$. We prepare the polydisperse HS fluid configurations at fixed packing fraction $\phi_{\mathrm{HS}} = 0.5$ by a Monte Carlo simulation. Particles are then inflated by the same factor, proportional to their radius (spheres are coloured according to their radius), to obtain an over-compressed soft spheres jammed packing at $\phi_{\mathrm{SS}} = 0.7$ by an infinitely fast quench (energy minimisation).

allows first-principles computation of configurational entropy as a function of system size and pressure. The method and the technical improvements needed to overcome this numerical challenge are presented alongside the main results.

The remainder of the chapter is organised as follows. Sec. 2.2 describes the basic principle of the mean basin volume method for counting, and explains how that strategy can be applied to enumerate granular packings. Sec. 2.3 outlines our protocol for sampling different granular packings, and it describes the corresponding potential energy landscape and minimisation techniques. Application of thermodynamic integration to compute the volume of a basin of attraction in such a landscape is described in Sec. 2.4. Aspects of the data analysis tools used on the histograms of sampled basin volumes, and related configurational entropy definitions, are described in Sec. 2.6. The enumeration and entropy results for three-dimensional jammed sphere packings as a function of system size and pressure are reported in Sec. 2.7. Conclusions are drawn in Sec. 2.8. Further technical background is given in the appendices.

2.2 Basic principle: counting by sampling

In this section, we briefly review the numerical approach that we use to compute the number of distinct jammed states. We stress that the approach that we use has much wider applicability than the counting of granular packings [16–31, 33, 43–46, 49–55]. In the context of granular packings, our aim is to compute the number of ways Ω in which N spheres can be arranged in a given volume V_{box} of Euclidean dimension d. Knowledge of Ω allows us to compute configurational entropies and related quantities from first principles [34, 57]. Our approach is based on a rigorous mapping of the enumeration problem onto counting the number of minima of a potential energy landscape [32]. The approach makes no use of a harmonic [127] or quasi-harmonic [128] approximation. For a system of hard particles the potential energy function is discontinuous, that is, the energy of the system is either zero, if no two particles overlap, or infinity otherwise. Then, at jamming, in the absence of rattlers, basins of attraction are single points in configuration space and they have no associated volume, see Fig. 2.3a. This does not mean that we cannot sample the energy minima of a system of hard particles. The reason is that all jammed structures of hard particles correspond to the zero potential energy minima of a system with a continuous repulsive potential with the same range as the hard-core diameter of the hard particles [123, 129, 130], see Fig. 2.3c. In what follows, we focus on this class of systems, but consider the broader ensemble of both zero and non-zero potential energy minima of a soft-sphere system at fixed volume fraction. O'Hern *et al.* [123, 130] have addressed the question of whether studying such an ensemble of states is relevant to the study of hard-sphere systems and found that when approaching the hard sphere limit by making the potential harder, the probability distributions of finding jammed states as a function of volume fraction, as well as the jamming volume fraction in the thermodynamic limit ($\phi^J_{N\to\infty}$), remain identical. In particular, we consider spherical particles with a hard core and a short-ranged continuous repulsive interaction. Under conditions where this system is jammed, a system with *only* the hard-core interactions would still be fluid and would sample the accessible configuration space uniformly. This remaining accessible volume is partitioned in basins of attraction defined by the soft shells, see Fig. 2.3. The HS-WCA potential used to simulate hard-core plus soft-shell interactions and the packing preparation protocol are described in Sec 2.3.2. For an illustration of the packing preparation protocol refer to Figs. 2.2-2.3. As we argue below, using an HS-WCA model greatly improves the efficiency of determination of basin volumes.

Let us denote the total available volume in dN-dimensional space as $\mathcal{V}_J$. Note that $\mathcal{V}_J$ is not the total volume of configuration space (V^N_{box}), but just that part of the volume that is free of hard-core overlaps – the configurational part of the partition function of the hard-core system at the number density under consideration – and not in a fluid state, see Fig. 2.3b.

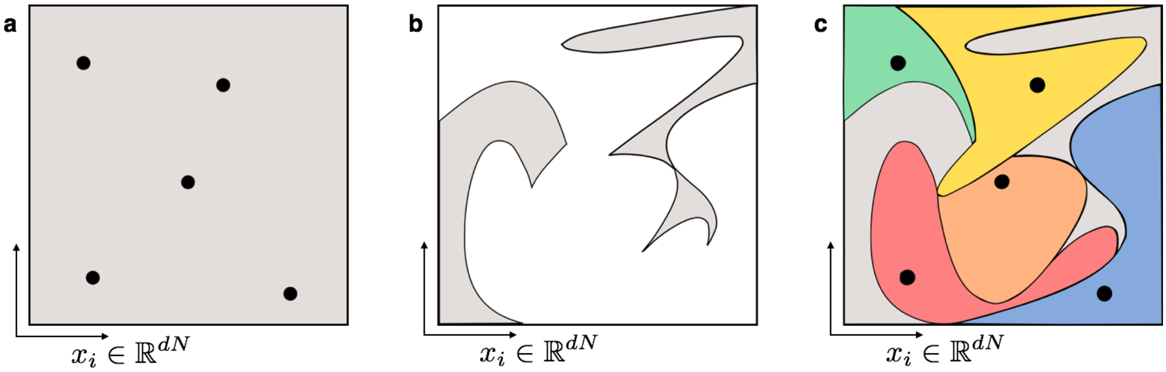

Fig. 2.3 (a) Simplified illustration of configurational space for a hard-sphere system at volume fraction $\phi_{\text{HS}} \geq \phi^J$. Solid dots and grey-shaded regions correspond to jammed packings and regions that are inaccessible due to hard core overlaps, respectively. (b) Configurational space for a hard-sphere system at volume fraction $\phi_{\text{HS}} < \phi^J$. The white regions correspond to accessible fluid states. The total volume of accessible fluid states $\mathcal{V}_J$ can be computed from the equation of state of the hard sphere fluid (see Appendix C). (c) Configurational space of the corresponding HS-WCA system at density $\phi_{\text{SS}} = \phi^J$. All jammed structures of the hard sphere system at the same density (solid dots in (a)) correspond to the zero potential energy minima of the HS-WCA system (solid dots in (c)). Single coloured regions correspond to the basins of attraction of individual minima. Basins of attraction tile the configurational space, such that $\mathcal{V}_J = \sum_{i=1}^{\Omega} v_i$, where v_i is the volume of the i-th basin. From the average volume of the basins of attraction we can find the total number of jammed packings Ω, as in Eq. 2.3.

Since the accessible configuration space is tiled by the basins of attraction of the distinct energy minima [127, 131–133] we can write:

$$\mathcal{V}_J = \sum_{i=1}^{\Omega} v_i, \tag{2.1}$$

where v_i is the volume of the i-th basin of attraction and Ω is the total number of distinct minima. We thus make the simple observation:

$$\sum_{i=1}^{\Omega} v_i = \frac{\Omega}{\Omega} \sum_{i=1}^{\Omega} v_i = \Omega \langle v \rangle, \tag{2.2}$$

where $\langle v \rangle$ is the *mean basin volume*, from which it follows immediately that

$$\Omega = \frac{\mathcal{V}_J}{\langle v \rangle}. \tag{2.3}$$

We note that, for sphere packings, $\mathcal{V}_J$ is known from the equation of state of the underlying hard sphere fluid (see Appendix C) and we can measure $\langle v \rangle$ by thermodynamic integration, as discussed in detail in the Sec 2.3. The approach of [32, 34] has thus turned the intractable enumeration problem of finding Ω into a sampling one, namely measuring $\langle v \rangle$.

2.3 Packing preparation protocol

2.3.1 Sampling packings

The physical properties of granular packings may depend strongly on the preparation protocol. This is illustrated by the Lubachevsky-Stillinger algorithm (LSA) procedure to prepare jammed packings of hard particles [134] by compression (or, equivalently, by 'inflation' of the particles). If a monodisperse HS fluid is compressed rapidly the LSA will generate a low volume-fraction disordered packing. However, for (very) slow compression rates, LSA will produce dense crystals [134, 135].

In the present work, we study a fluid of polydisperse spheres. We use a protocol related to a Stillinger-Weber quench that maps each fluid state to a local minimum, or "inherent structure", connected by a path of steepest descent [131, 136], see Appendix A for a discussion of paths of steepest descent.

To prepare the polydisperse fluid, we draw N particle radii $\{r\}_N$ from a Gaussian distribution $\mathrm{Normal}(1, \sigma_{\mathrm{HS}}) > 0$, truncated at $r = 0$ (note that in our application the standard deviation σ_{HS} is sufficiently small that it is extremely improbable to ever sample a negative radius). We set the box size to meet the target packing fraction of the hard sphere fluid ϕ_{HS} and then place the particles in a valid random initial hard spheres configuration. The initial configuration is then evolved by a MC simulation [137] consisting of single particle random displacements and particle-particle swaps, and after equilibration, new configurations are recorded at regular intervals. We choose the length of these intervals such that, on average, each particle diffuses over a distance equal to the diameter of the largest particle. As long as ϕ_{HS} is well below the volume fraction where the fluid undergoes structural arrest, the allowed configurations of the fluid can be sampled uniformly. Importantly, this volume fraction is well below the random close packing ($\phi_{\mathrm{HS}}^{(\mathrm{RCP,\ 3D})} \approx 0.64$ and $\phi_{\mathrm{HS}}^{(\mathrm{RCP,\ 2D})} \approx 0.84$ [123]).

Given these HS fluid configurations, we now switch on the soft, repulsive interaction to generate over-compressed jammed packings of the particles (see Fig. 2.2). The particles are inflated with a WCA-like potential [138] to reach the target soft packing fraction $\phi_{\mathrm{SS}} > \phi_{\mathrm{HS}}^{(\mathrm{RCP})} > \phi_{\mathrm{HS}}$. The hard spheres are inflated proportional to their radius, so that the soft sphere radius is

$$r_s = \left(\frac{\phi_{\mathrm{SS}}}{\phi_{\mathrm{HS}}} \right)^{1/d} r_h, \tag{2.4}$$

where d is the dimensionality of the box. Clearly, this procedure does not change the polydispersity of the sample.

2.3.2 Soft shells and minimisation

We define the WCA-like potential around a hard core as follows: consider two spherical particles with hard core distance r_h and soft core contact distance $r_s = r_h(1+\theta)$, with $\theta = (\phi_{\mathrm{SS}}/\phi_{\mathrm{HS}})^{1/d} - 1$. We can then write a horizontally shifted hard-sphere plus WCA (HS-WCA) potential as

$$u_{\text{HS-WCA}}(r) = \begin{cases} \infty & r \leq r_h, \\ 4\varepsilon\left[\left(\frac{\sigma(r_h)}{r^2 - r_h^2}\right)^{12} - \left(\frac{\sigma(r_h)}{r^2 - r_h^2}\right)^{6}\right] + \varepsilon & r_h < r < r_s, \\ 0 & r \geq r_s \end{cases} \tag{2.5}$$

where $\sigma(r_h) = (2\theta + \theta^2)r_h^2/2^{1/6}$ guarantees that the potential and its first derivative go to zero at r_s. For computational convenience (avoidance of square-root evaluations), the potential in Eq. (2.5) differs from the WCA form in that the inter-particle distance in the denominator of the WCA potential has been replaced with a difference of squares. Our potential still resembles as 12-6 potential and any difference, for our purpose, is immaterial: we just need a short-ranged repulsive potential that diverges at the hard-core diameter and vanishes continuously at the soft-core diameter. The functional form of this potential is very similar to the HS-WCA potential used by Asenjo *et al.* [34], but cheaper to compute. We note that this potential is a C^1 type function, *i.e.* its first derivative is continuous but not differentiable and its second derivative is discontinuous at r_s.

A power series expansion of Eq. 2.5 yields

$$\lim_{r \to r_s} u_{\text{HS-WCA}} = \varepsilon \left(\frac{12 r_s}{r_h^2 - r_s^2}\right)^2 (r - r_s)^2 + O\left((r - r_s)^3\right), \tag{2.6}$$

hence, in the limit of no overlap, the interaction is repulsive harmonic (harder than the repulsive Hertzian interactions with exponent $5/2$).

Numerically evaluating this potential, we match the gradient and linearly continue the function $u_{\text{HS-WCA}}(r)$ for $r \leq r_h + \delta$, with $\delta > 0$ an arbitrary small constant, such that minimisation is still meaningful if overlaps do occur.

The HS-WCA pair-potential was implemented using cell-lists [139, 140] with periodic boundary conditions, guaranteeing $\mathcal{O}(N)$ time complexity to the energy and gradient evaluations. Energy minimisations were performed with the CG_DESCENT algorithm [141–143] which, compared to FIRE [140, 144], reduces the average number of function evaluations for our system by a factor of 5, while preserving many of its desirable properties.

2.4 Basin volume by thermodynamic integration

The basin of attraction of a given minimum-energy configuration is the collection of all points connected to that minimum via a path of steepest descent [125, 145], see Appendix A. To measure the volume of a basin of attraction in the PES, we use thermodynamic integration [146, 147] and parallel tempering (PT) [137, 148–150].

The basic idea behind the method is that, but for the sign, the logarithm of the basin volume can be viewed as a dimensionless free energy. We cannot determine this free energy directly. We now switch on an increasingly steep harmonic potential that has its minimum at the minimum of the basin. In the limit of very large coupling constants (how large depends on the shape of the basin) the boundaries of the basin no longer affect the free energy of the system, which has effectively been reduced to a dN dimensional harmonic oscillator with known free energy (for more details, see Appendix B.1). For zero coupling constant, instead, the system is completely unconstrained and therefore in the state of interest. Thermodynamic integration allows us to compute the free energy difference between a reference state of known free energy and the (unknown) free energy associated with the original basin of attraction.

A closely related approach is often used to compute the free energy of crystals of particles with a discontinuous potential, such as hard spheres [146, 147, 151]. Details of that method are summarised in the Appendix B.2, and the extension of the technique to basin volume measurement is described below. Details of the Hamiltonian PT are discussed in Appendix B.3.

2.4.1 Free energy calculation for basin volumes

To measure the volume of a basin of attraction by thermodynamic integration, we perform a walk inside the basin, that is, we start the MCMC random walk from the minimum energy configuration $\mathbf{x}_i$ and we reject every move that takes us outside the basin [32–34]. This procedure can be cast in normal Monte Carlo language by defining an effective potential energy function (oracle) $U_B(\mathbf{x}|\mathbf{x}_i)$ which is zero inside the basin and infinite outside. We can then write the volume of the basin:

$$v_i = \int \mathrm{d}\mathbf{x}\, e^{-U_B(\mathbf{x}|\mathbf{x}_i)}. \tag{2.7}$$

In order for the oracle to test whether a proposed configuration is inside or outside the basin, a full energy minimisation must be performed. The numerous potential energy calls required for a full energy minimisation represent the major obstacle to the scalability of the method.

We view the basin negative log-volume as a dimensionless free energy $F_i \equiv -\ln(v_i)$ [32] and compute it by thermodynamic integration, as described in Appendix B.2. Therefore, we write, analogously to Eq. (B.13):

$$\begin{aligned} -\ln v_i &= F_{\text{har}}(k_{\text{max}}) + \Delta F \\ &\equiv F_{\text{har}}(k_{\text{max}}) - \frac{1}{2}\int_0^{k_{\text{max}}} \mathrm{d}k \, \langle |\mathbf{x} - \mathbf{x}_i| \rangle_k \,, \end{aligned} \tag{2.8}$$

where $\mathbf{x}_i$ denotes the coordinates of the i-th energy minimum and ΔF, defined above, is the dimensionless free energy difference between the reference state and the uncoupled random walker (with $k = 0$).

Unless k_{max}, the maximum spring constant of the harmonic reference system, is very large, a finite fraction of the points belonging to the purely harmonic reference system will be located in the region where $U_B = \infty$. We can correct for this effect in our calculation of $F_{\text{har}}(k_{\text{max}})$ by computing the ratio of the partition functions of a system with a harmonic spring constant k_{max}, both with and without the basin potential energy function U_B. This ratio is given by

$$\mathcal{R} \equiv \frac{\displaystyle\int \mathrm{d}\mathbf{x} \exp[-U(\mathbf{x}|\mathbf{x}_i, k_{\text{max}}) - U_B(\mathbf{x}|\mathbf{x}_i)]}{\displaystyle\int \mathrm{d}\mathbf{x} \exp[-U(\mathbf{x}|\mathbf{x}_i, k_{\text{max}})]}, \tag{2.9}$$

where U is the sum of the hard-core potential and the harmonic potential with spring constant k_{max}, see Eq. (B.12). We note that $\mathcal{R}$ can be computed using a 'static' (*i.e.* non-Markov chain) Monte Carlo simulation, sampling directly from the Boltzmann distribution of the harmonic oscillator with spring constant k_{max}. Since the integral in the denominator is known [see Eq. (B.2)], we write the dimensionless free energy of the harmonic reference state for a basin as

$$F_{\text{har}}(k_{\text{max}}) = -\frac{dN}{2} \ln\left(\frac{2\pi}{k_{\text{max}}}\right) - \ln \mathcal{R}. \tag{2.10}$$

We note that, in order to avoid a singularity in the integrand, it is useful to perform the simulations fixing the centre of mass. It follows that the same corrections to the free energy as derived in Refs.[146, 147, 151] must be applied: similarly to the expression obtained for

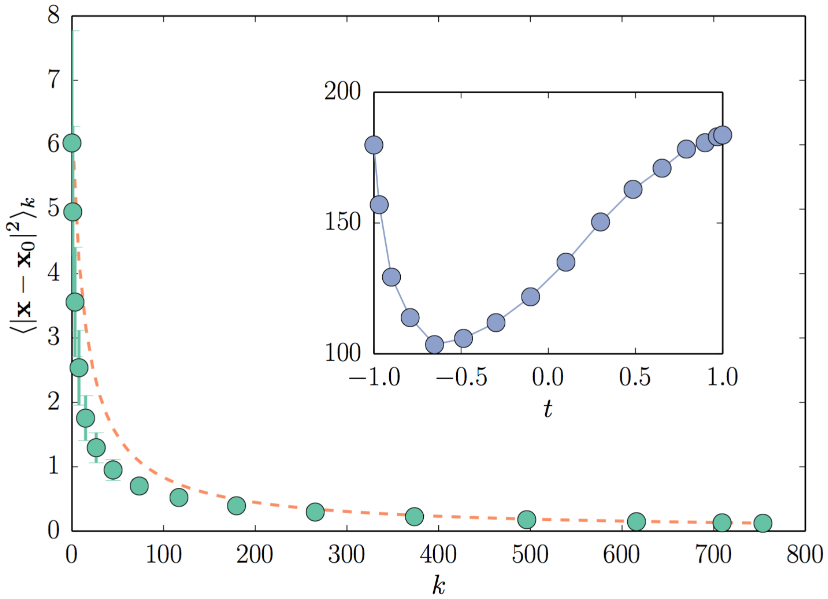

Fig. 2.4 Average squared displacement $\left\langle|\mathbf{x}-\mathbf{x}_0|^2\right\rangle_k$ as a function of the spring constant k (symbols). The dashed line shows the expression in Eq. (B.19). The data is measured for a packing of $N = 32$ spheres, with $\phi_{\mathrm{HS}} = 0.5$ and $\phi_{\mathrm{SS}} = 0.7$ via Hamiltonian PT. Inset: corresponding integrand for the thermodynamic integration, resulting from the change of variables in Eq. (B.24).

the free energy of solids Eq. (B.16), but with the additional correction defined in Eq. (2.10), we write the basin volume as:

$$\begin{aligned} -\ln v_i &= \Delta F^{(\mathrm{CM})} - \ln\left(V_{\mathrm{box}}\right) \\ &\quad - \frac{(N-1)d}{2}\ln\left(\frac{2\pi}{k_{\max}}\right) - \ln\mathcal{R}, \end{aligned} \tag{2.11}$$

where the dimensionless free energy difference $\Delta F^{(\mathrm{CM})}$ is defined as in Eq. (2.8) but with the ensemble averages (the integrand) computed with a constrained centre of mass and it is evaluated as in Eq. (B.24).

Figure 2.4 shows an example of the mean squared displacement $\left\langle|\mathbf{x}-\mathbf{x}_0|^2\right\rangle_k$, as a function of the spring constant k, along with the approximate expression in Eq. (B.19) used to construct the change of variables in Eq. (B.24). The resulting integrand, after the variable transform, is shown in the inset of Fig. 2.4.

2.5 Basin volume method summary

In summary, to count the number of ways spheres can pack into a given volume, we use the mean basin volume method outlined in Sec. 2.2. We perform the following simulations and analysis steps to obtain the required results:

1. Obtain a number of different snapshots of an equilibrated hard sphere fluid at the desired volume fraction ϕ_{HS}, as described in Sec. 2.3.1. This procedure fixes the number of measured basin volumes.
2. Over-compress the sphere configuration by adding a soft shell. This compression yields, upon energy minimisation, a jammed packing with soft volume fraction $\phi_{\mathrm{SS}} > \phi_{\mathrm{HS}}$.
3. Estimate the maximum spring constant for the PT simulations, $k_{\max}$ in Eq. (2.8), such that $\mathcal{R}$ in Eq. (2.9) reaches a value between 0.85 and 0.9. This is done by direct sampling and also gives the value of the average squared displacement for $k_{\max}$, $\left\langle |\mathbf{x}-\mathbf{x}_0|^2 \right\rangle_{k_{\max}}$.
4. Obtain a preliminary estimate of the average squared displacement without harmonic tethering, $\left\langle |\mathbf{x}-\mathbf{x}_0|^2 \right\rangle_0$, by performing a MCMC walk in the basin. Use this result, with the estimate of $k_{\max}$ from the previous step, to determine the spring constants k for the PT simulation, using Eqs. (B.22) and (B.25).
5. Perform a PT simulation to sample $\left\langle |\mathbf{x}-\mathbf{x}_0|^2 \right\rangle_k$, as described in Appendix B.3.
6. Compute the volume in Eq. (2.11) for each basin and analyse the distributions for all basins, at fixed volume fraction and number of particles, as discussed in Sec. 2.6. This makes use of the total accessible volume $\mathcal{V}^J$, computed in Appendix C.

Evaluation and minimisation of potential energy functions was performed with the pele [140] and PyCG_DESCENT [143] software packages. Monte Carlo simulations were performed with the mcpele package [137].

2.6 Basin volume distributions

Once the volumes of multiple basins have been sampled, these data can be used to compute the number of distinct packings [34], and from that, the Edwards entropy [57]. Furthermore we analyse the distribution of pressures of the different energy minima at given volume. In this work, we express pressure and volume in reduced units P/P^* and v/v^* everywhere with $v^* \equiv (4\pi/3)\langle r_h^3 \rangle$ and $P^* \equiv \varepsilon/v^*$ being the units of volume and pressure, respectively.

2.6.1 Gibbs configurational entropy

Let us first consider the ‘Gibbs-like’ configurational entropy, S_G, defined by Asenjo *et al.* [34]:

$$S_G = -\sum_{i=1}^{\Omega} p_i \ln(p_i) - \ln(N!), \tag{2.12}$$

where p_i is the probability to sample packing i. For our preparation protocol, packings are sampled according to the volume of their basin of attraction, such that $p_i = v_i/\mathcal{V}_J$. Then Eq. (2.12) gives

$$\begin{aligned} S_G &= -\sum_{i=1}^{\Omega} p_i \ln(v_i) + \ln(\mathcal{V}_J) - \ln(N!) \\ &= \langle F \rangle_{\mathcal{B}} + \ln(\mathcal{V}_J) - \ln(N!). \end{aligned} \tag{2.13}$$

The sum in Eq. (2.13) is the mean of the negative basin log-volumes (dimensionless free energies), as computed above, and weighted by the probabilities of preparing the corresponding basins. Therefore, the entropy can be obtained directly, and without approximation, from the sampled mean basin dimensionless free energy.

From Eq. (2.13) we can also write the entropy per particle in the thermodynamic limit as

$$s_G(\phi_{\mathrm{SS}}) = 1 + \langle f \rangle_{\mathcal{B}} - \ln(\phi_{\mathrm{SS}}) - f_{\mathrm{ex}}(\phi_{\mathrm{HS}}), \tag{2.14}$$

where $f_{\mathrm{ex}}(\phi_{\mathrm{HS}})$ is the excess free energy of the hard spheres fluid. In deriving this results we used Stirling’s approximation for large N and the fact that $V_{\mathrm{box}}/v^* = N/\phi_{\mathrm{SS}}$.

2.6.2 Edwards configurational entropy

Edwards [57] suggested a ‘Boltzmann-like’ entropy, where S equals the logarithm of Ω, the total number of packings. Asenjo *et al.* [34] showed that, even for polydisperse particles, indistinguishability of macrostates requires that

$$S_B = \ln(\Omega) - \ln(N!). \tag{2.15}$$

The subtraction of $\ln(N!)$ is necessary to guarantee extensivity of the entropy. Unlike the Gibbs definition of entropy, Eq. (2.15) makes the explicit assumption of equiprobability of states.

For a direct computation of the number of packings Ω, using Eq. (2.3), we need the average basin volume $\langle v \rangle$. Since our preparation protocol samples each minimum with a probability proportional to the volume of its basin of attraction, our samples of v are biased accordingly. Therefore, to obtain the unbiased average basin volume $\langle v \rangle$, the sampled basin volume distribution needs to be unbiased [33, 34, 89]. The unbiasing method used in the following work requires an analytical (or at least numerically integrable) description of the biased basin free energy distribution function. Different approaches to modelling this distribution give rise to somewhat different analysis methods, which all yield consistent results. Again, we stress that no such additional steps are needed to compute the 'Gibbs-like' version of the configurational entropy.

We distinguish between the biased, $\mathcal{B}(F|N,\phi_{\mathrm{SS}})$ (as sampled by the packing protocol), and the unbiased, $\mathcal{U}(F|N,\phi_{\mathrm{SS}})$, free energy distributions. Since the configurations were sampled proportional to the volume of their basin of attraction, we can compute the unbiased distribution as

$$\mathcal{U}(F|N,\phi_{\mathrm{SS}}) = \mathcal{Q}(N,\phi_{\mathrm{SS}})\mathcal{B}(F|N,\phi_{\mathrm{SS}})e^{F} \tag{2.16}$$

where $\mathcal{Q}(N,\phi_{\mathrm{SS}})$ is the normalisation constant

$$\mathcal{Q}(N,\phi_{\mathrm{SS}}) = \left[\int_{F_{\mathrm{min}}}^{\infty} \mathrm{d}F \mathcal{B}(F|N,\phi_{\mathrm{SS}})e^{F}\right]^{-1} = \langle v \rangle(N,\phi_{\mathrm{SS}}). \tag{2.17}$$

From Eq. (2.16), unbiasing of the raw free energy distribution seems straightforward, however Asenjo *at al.* [34] noted that the most probable basins are about $O(10^3)$ more probable than the small ones. Upon unbiasing, this factor is multiplied by a factor of about e^{-20}, hence they observe that small basins are much more numerous than large ones and grossly undersampled.

To overcome this problem, one can fit the biased measured free energy distribution $\mathcal{B}(F|N,\phi_{\mathrm{SS}})$ and perform the unbiasing via Eq. (2.16) on the best fitting distribution. $\mathcal{B}(F|N,\phi_{\mathrm{SS}})$ must be bounded, hence it should decay with a functional form $\exp(-F^{\nu})$ where $\nu > 1$.

Before performing the fit we remove outliers from the free energy distribution following the distance-based outlier removal method introduced by Knorr and Ng [152] described in Appendix E.4, with $D = 3\sigma$, $R = 0.5$.

2.7 Results: Counting disordered three-dimensional sphere packings

The mean basin volume method for enumerating the number of mechanically stable packings was introduced by Xu *et al.* [32], and tested on a small system of soft disks. Asenjo *et al.* [34] then made a number of modifications to the algorithm that allowed them to apply it to larger systems of up to 128 disks. As was the case with Ref. [32], the calculations of Ref. [34]

focused on two-dimensional systems because of the high computational costs involved in studying 3D systems. Here we present results for systems of three-dimensional soft spheres. We are thus in a position to compute the configurational entropy of a real (but idealised) three-dimensional system.

We first describe an analysis similar to the one reported by Asenjo *et al.* [34] to verify the extensivity of the entropy $S(V)$ at constant packing fraction. Next, we extend our approach to the generalised Edwards ensemble, *i.e.* one based on a description of the system in terms of its volume and pressure, to compute the generalised entropy $S(V,P)$.

We investigate three-dimensional packings with system sizes ranging from 24 to 128 HS-WCA particles, see Eq. (2.5), at $\phi_{\mathrm{HS}} = 0.5$ hard-sphere fluid packing fraction and $\phi_{\mathrm{SS}} = 0.7$ soft sphere packing fraction, corresponding to a ratio of the soft and hard-sphere radii ratio $r_{\mathrm{SS}}/r_{\mathrm{HS}} = 1.12$, prepared following the protocol outlined in Sec. 2.3. For each system size we compute the volume of the basin of attraction of approximately 1000 packings. Each PT run (see Sec. 2.4) was performed on 15 parallel threads of a single eight-core dual Xeon $\mathrm{E5}-2670$ (2.6GHz, Westmere) node. Our choice of convergence criterion was such that when the uncorrelated statistical error for each of the replicas' mean square displacement fell below 5% the calculations were terminated. This set-up translated in run times ranging from 10 to 300 hours per basin depending on system size, which amounts to $\mathcal{O}(10^6)$ hours of total run time and $\mathcal{O}(10^7)$ total cpu hours. We then analyse the corresponding distribution of dimensionless free energies following the protocol described in Sec. 2.4 and 2.6 and summarised in Sec. 2.5.

2.7.1 Extensivity of the entropy

We first computed two alternative definitions of entropy: the Gibbs entropy $S_G = -\sum_{i=1}^{\Omega} p_i \ln(p_i) - \ln(N!)$ and Edwards (Boltzmann) entropy $S_B = \ln(\Omega) - \ln(N!)$, where p_i is the probability to sample packing i and Ω is the total number of mechanically stable states (or minima in the energy landscape). A detailed discussion of these definitions is outlined in Sec. 2.6. The results of these calculations are summarised in Fig. 2.5. Our results strongly suggest that, also in three dimensions, the entropy thus defined is extensive. Note that extensivity requires not only that the entropy scales linearly with system size, but also that it crosses zero at the origin. The slightly higher value of the Edwards entropy compared to the Gibbs entropy is consistent with the observation that Edwards' equiprobability corresponds to the maximum possible entropy of a system with Ω states. We also show that our estimates for the Edwards' entropy are relatively insensitive to the precise strategy used to compute it. In Fig. 2.5, we compare three methods: a parametric fit to a generalised Gaussian cumulative distribution function (c.d.f.) using a non-linear least squares method, a fit to the corresponding probability density function (p.d.f.) using maximum likelihood, and a non-parametric fit by kernel density estimation, which makes no a priori assumption about the shape of the distribution, other than the choice of the kernel function. We note, once again, that no post-processing is needed to compute the Gibbs version of the configurational entropy. Our results are in line with those reported by Asenjo *et al.* [34] for two-dimensional systems.

The number of mechanically stable states Ω required by the Edwards' definition of entropy is obtained subsequently to fitting the numerically obtained distribution of basin log-volumes (dimensionless free energies) to a generalised Gaussian distribution and unbiasing it appropriately, as described in Sec 2.6. We observe that the best-fit mean and squared scale parameters of the generalised Gaussian for the distribution of dimensionless free energies, μ and σ^2 in Eq. (E.1) respectively, are also extensive, which although in line with what was found in two dimensions, is not *a priori* obvious. Finally we find that the shape parameter, ζ in Eq. (E.1), appears to depend only weakly on system size. The statistics are poor, but the data are compatible with the assumption that $\zeta \to 2$ (Gaussian distribution) as $N \to \infty$. In 2D, the same limiting distribution of ζ, but with a much stronger size dependence, was observed.

2.7.2 Entropy in the generalised Edwards ensemble

We next consider the situation where the configurational entropy is a function of both the volume V and the stress tensor $\hat{\Sigma}$ of the system. The number of packings with fixed V and $\hat{\Sigma}$ is denoted by $\Omega(V,\hat{\Sigma})$.

In the generalised Edwards ensemble [61, 66, 118], we fix the variables conjugate to V and $\hat{\Sigma}$, *viz.* the compactivity X and the inverse angoricity tensor $\hat{\alpha}$. The generalised 'partition function' can then be written as [61]:

$$Z = \sum_{\nu} \omega(V_\nu, \hat{\Sigma}_\nu) e^{-V_\nu/X} e^{-\mathrm{Tr}(\hat{\alpha}\hat{\Sigma}_\nu)}, \tag{2.18}$$

where V_ν and $\hat{\Sigma}_\nu$ are the volume and the force-moment (stress) tensor for state ν. The weights ω account for the protocol dependence of the probability to generate a state, and the sum runs over all mechanically stable states ν.

We can rewrite this partition function in terms of the density of states:

$$Z = \prod_{l,k>l} \iint \mathrm{d}\hat{\Sigma}^{lk}\, \mathrm{d}V\, \Omega(V,\hat{\Sigma}) e^{-V/X} e^{-\mathrm{Tr}(\hat{\alpha}\hat{\Sigma})}. \tag{2.19}$$

For a system under hydrostatic pressure, and in the absence of shear, we can write the force-moment tensor as $\hat{\Sigma} = \hat{I}\Gamma$, where $\Gamma = PV = \mathrm{Tr}(\hat{\Sigma})/3$ is the internal Virial of the system. The

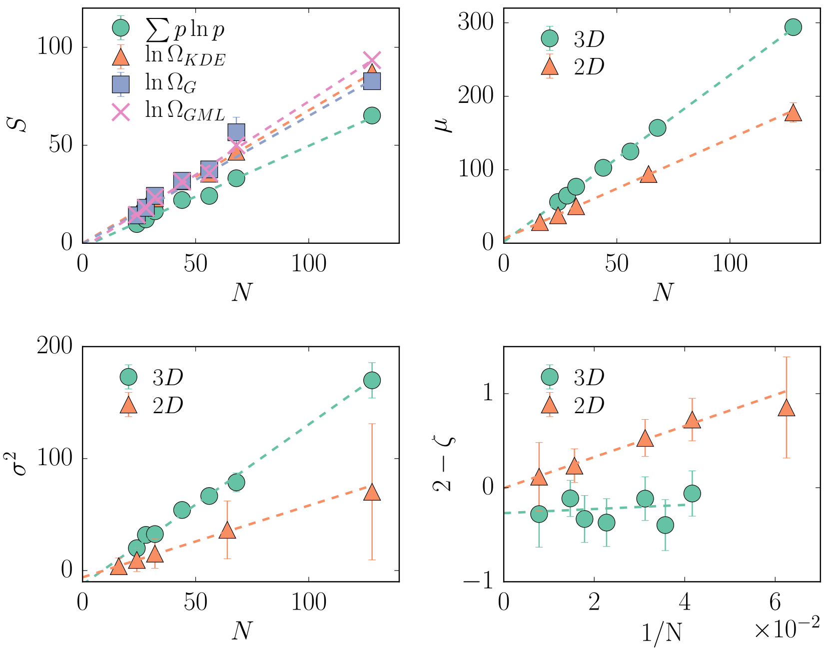

Fig. 2.5 Top left, entropy as a function of the system size N computed, in order, according to the Gibbs configurational entropy and the Edwards configurational entropy using a non-parametric fit by kernel density estimation (KDE), a parametric fit to a generalised Gaussian c.d.f. using a non-linear least squares method and a fit to the corresponding p.d.f. using maximum likelihood (ML). Comparison of generalised Gaussian best-fit parameters for 2D (see Ref. [34]) and 3D sphere packings: squared scale parameter σ^2 (bottom left) and mean log-volume μ (top right) scale linearly with system size N; distributions are more peaked for 2D packings. In 2D we observe much stronger dependence of the shape parameter ζ (bottom right) as a function of system size than in 3D.

inverse angoricity tensor $\hat{\alpha}$ becomes a scalar $\alpha = \partial S/\partial \Gamma$ [118]. This result allows to simplify the notation significantly and at fixed volume, through the mean basin volume method, we obtain the number of states integrated over all pressure states, $\Omega(V) = \int \mathrm{d}P \Omega(V,P)$. We now discuss how to generalise this procedure so that one can compute $\Omega(V,P)$, and therefore the configurational entropy, in the context of the generalised Edwards ensemble.

Pressure to basin volume power-law relation

To compute $Z(X,\alpha)$ directly, we would have to evaluate $\Omega(V,P)$ as a function of both P and V. Whilst, with the tools that we have, this calculation is in principle possible, the computational costs would be several orders of magnitude larger than the, already quite substantial, costs of computing $\Omega(V)$. This would suggest that the computation of $Z(X,\alpha)$ is not possible at present.

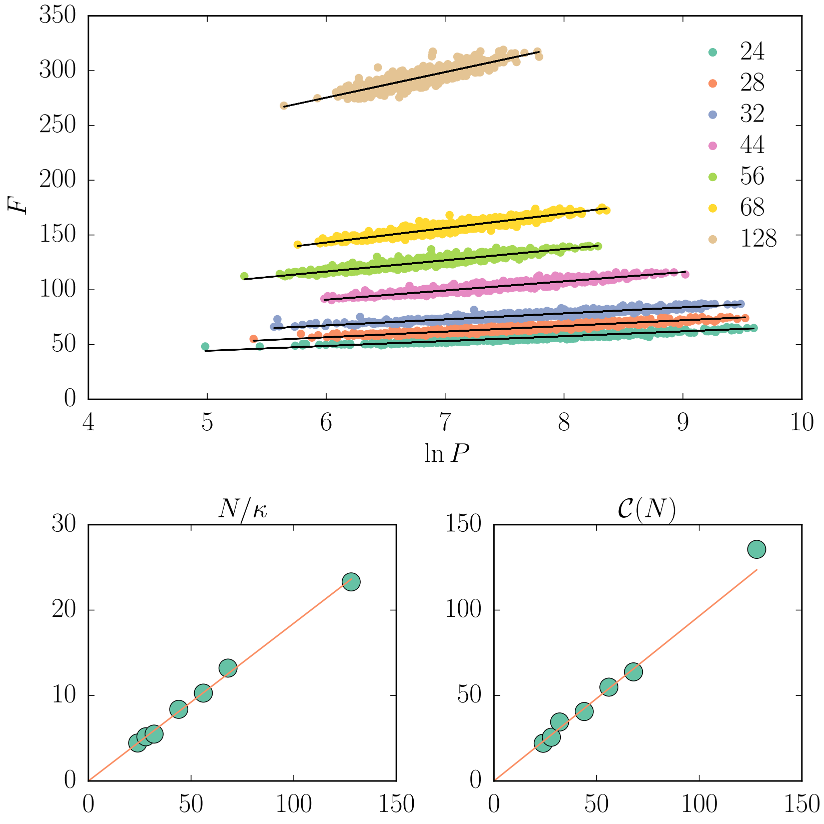

Fig. 2.6 Top: basin log-volume versus log-pressure of mechanically stable states at fixed volume for several system sizes. Best fit lines are in black. In the bottom left and right plots we show slope and intercept for each of the best fit lines as a function of system size. Both slope and intercept scale linearly with system size.

However, it turns out that we can still estimate the generalised configurational entropy because, as we discuss below, we observe a surprisingly strong correlation between pressure and basin volume.

From Fig. 2.6 we see that the basin volume for a given pressure state at fixed volume is strongly correlated with the pressure P. As the figure suggests, the relation between $F \equiv -\ln(v)$ and $\Lambda \equiv \ln(P)$ is approximately linear, and hence we can write the conditional expectation of F given Λ, as

$$\langle F \rangle_{\mathcal{B}}(\Lambda | N, \phi_{\mathrm{SS}}) = \frac{N}{\kappa}\Lambda + \mathcal{C}(N), \tag{2.20}$$

where $\langle F \rangle_{\mathcal{B}}(\phi;\Lambda)$ represents the average over all basins at a given Λ, κ denotes the slope of the linear fit, and $\mathcal{C}(N)$ its value at $\Lambda = 0$. As can be seen see from Fig. 2.6, Eq. (2.20) is valid for any N. Under the assumption that the joint probability $\mathcal{B}(F,\Lambda)$ is a bivariate

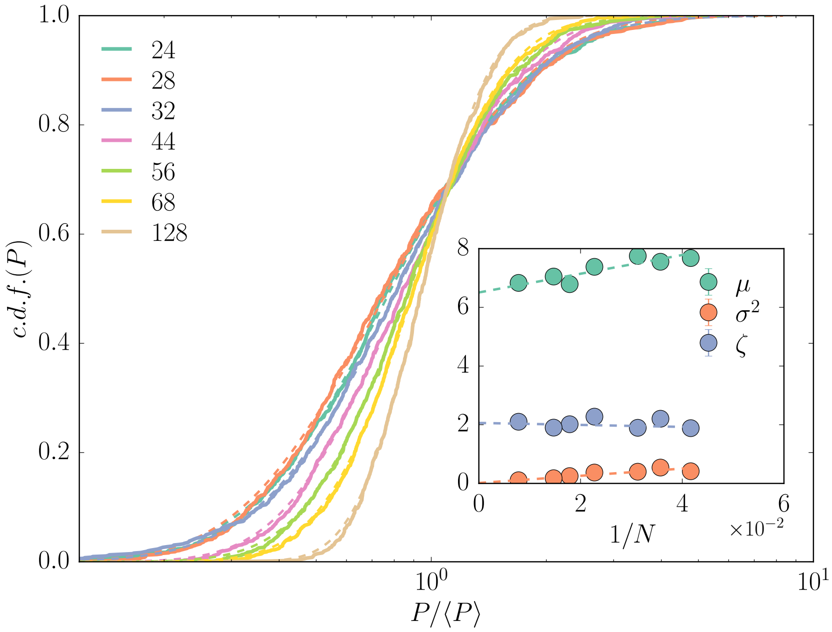

Fig. 2.7 Empirical cumulative distribution functions of the pressures for several system sizes. Dashed lines in the corresponding colour are curves of best fit to a generalised log-normal distribution. The curves are mostly indistinguishable. Inset: best fit parameters for the generalised log-normal distribution as a function of system size. The mean μ and squared scale parameter σ^2 scale linearly with $1/N$, while the shape parameter ζ is approximately insensitive with respect to system size.

Gaussian, consistent with the elliptical distribution in Fig. 2.6, one can gain further insight into the significance of the fit parameters κ and $\mathcal{C}$, a full discussion is given in Appendix D. This expression survives in 2D over a wide range of volume fractions and forms the basis of much of Chapt. 3.

Gibbs configurational entropy

Using our approximate relation between pressure and basin volume, we can now rewrite Eq. (2.20) in terms of the probabilities for each jammed state

$$\ln(p_i) = -\frac{N}{\kappa}\Lambda_i - \mathcal{C}(N) - \ln(\mathcal{V}_J), \tag{2.21}$$

which when substituted in the definition for the Gibbs entropy Eq. (2.13), gives the configurational entropy at a given volume in terms of the biased mean log-pressure

$$S_G = \frac{N}{\kappa}\langle\Lambda\rangle_{\mathcal{B}} + \mathcal{C}(N) + \ln(\mathcal{V}_J) - \ln(N!). \tag{2.22}$$

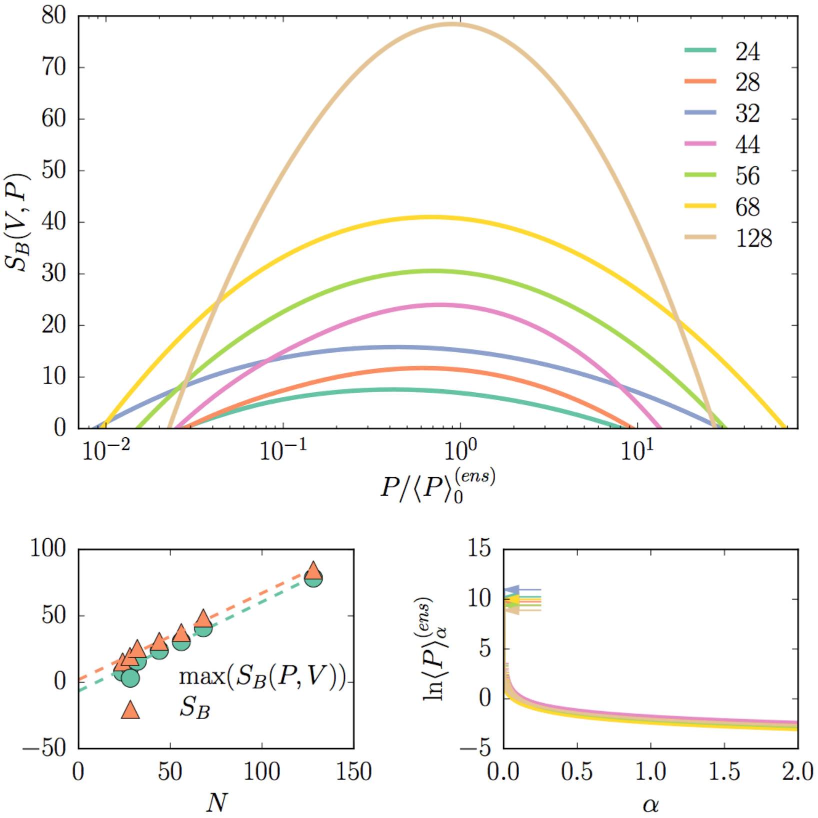

Fig. 2.8 Top: generalised Edwards entropy at fixed volume fraction for various system sizes. The curves show a well defined maximum for all sizes, while their shape depends on the specific parameters of the generalised log-normal that best fits the underlying distribution of pressures. Bottom left: comparison between the Edwards entropy and the maximum value attained by each curve: $\max[S_B(V,P)]$ scales linearly with size and its value is progressively closer to the marginal (total) Edwards entropy $S_B(V)$, consistent with the fact that $S_B(V,P)$ is a negative exponential function, and the area under the curve is dominated by the mode for increasing system size. $S_B(V)$ should constitute an upper limit to $\max[S_B(V,P)] \leq S_B(V)$ and the two should be equivalent only in the thermodynamic limit. Bottom right: ensemble average of the pressure computed as a function of inverse angoricity α and system size. The curves, in the same colour as the top figure, do not diverge and the arrows indicates their value at $\alpha = 0$.

The significance of this equation should be apparent: for a sufficiently over-compressed packings of soft spheres at a given packing fraction, the Gibbs configurational entropy can be approximately computed from sole knowledge of the average pressure, provided that κ is known.

Generalised Edwards configurational entropy

To recover the number of states as a function of volume and stress we note that

$$\Omega(V,P) = \Omega(V) \int_P^{P+\delta P} \mathcal{U}(x|V)\,\mathrm{d}x, \tag{2.23}$$

where $\mathcal{U}(P|V)$ is the unbiased probability distribution function of stresses at some specified volume. The directly measured distribution of pressures depends on the protocol with which packings are generated.

We distinguish between the biased, $\mathcal{B}(P|N,\phi_{\mathrm{SS}})$ (as sampled by the packing protocol), and the unbiased, $\mathcal{U}(P|N,\phi_{\mathrm{SS}})$, pressure distributions. Since the configurations were sampled proportional to the volume of their basin of attraction, using Eq. (2.20) we can compute the unbiased distribution analogously to Eq. (2.16) as

$$\mathcal{U}(P|N,\phi_{\mathrm{SS}}) = \mathcal{Q}(N,\phi_{\mathrm{SS}})\mathcal{B}(P|N,\phi_{\mathrm{SS}})e^{\mathcal{C}(N)}P^{N/\kappa}, \tag{2.24}$$

where $\mathcal{Q}(N,\phi_{\mathrm{SS}}) = \langle v\rangle(N,\phi_{\mathrm{SS}})$ is the normalisation constant.

Upon substitution of $\ln\Omega(V) = \ln(\mathcal{V}_J) - \ln(\langle v\rangle)$ and of Eq. (2.24) for $\mathcal{U}(x|V)$, we write an expression for the Edwards entropy as a function of volume and pressure

$$\begin{aligned} S_B(V,P) = &\ln\left(\int_P^{P+\delta P} \mathcal{B}(x|V)x^{N/\kappa}\,\mathrm{d}x\right) \\ &+ \ln(\mathcal{V}_J) + \mathcal{C}(N) - \ln(N!). \end{aligned} \tag{2.25}$$

We fit the empirical cumulative distribution function (c.d.f.) of $\mathcal{B}(P)$ with the generalised log-normal c.d.f. corresponding to Eq. (E.2) (see Fig. 2.7). We then numerically evaluate the generalised Edwards entropy $S_B(V,P)$ at fixed volume, as shown in Fig. 2.8.

In the thermodynamic limit we find (derived next in Sec. 2.7.3)

$$s_B(\phi_{\mathrm{SS}}) = 1 + c + \frac{\langle\Lambda\rangle_{\mathcal{B}}}{\kappa} - \ln(\phi_{\mathrm{SS}}) - f_{\mathrm{ex}}(\phi_{\mathrm{HS}}) + \mathcal{O}\left((1/\kappa)^2\right), \tag{2.26}$$

where $c = \mathcal{C}(N)/N$. The $\mathcal{O}((1/\kappa)^2)$ correction amounts to residual difference between the Gibbs and Boltzmann entropy in the thermodynamic limit. This is due to the fact that 2.20

survives the limit and the two quantities are identical only if $1/\kappa \to 0$. It will be shown in Chapter 3 that for two-dimensional systems this condition is satisfied only at the unjamming density, as $\phi_{\mathrm{SS}} \to \phi^J_{N\to\infty}$.

In Fig. 2.8 we also show the predicted expectation value for the pressure obtained via the ensemble average at arbitrary inverse angoricity α,

$$\langle P \rangle_\alpha^{(ens)} = \frac{\displaystyle\int_0^\infty P\mathcal{B}(P|V)P^{N/\kappa}e^{-\alpha PV}\,\mathrm{d}P}{\displaystyle\int_0^\infty \mathcal{B}(P|V)P^{N/\kappa}e^{-\alpha PV}\,\mathrm{d}P}. \tag{2.27}$$

2.7.3 Thermodynamic limit of the generalised configurational entropy

From the fit to the empirical c.d.f. of $\mathcal{B}(P)$ with the generalised log-normal cumulative distribution function, corresponding to Eq. (E.2), we obtain the set of parameters μ, σ, and ζ. From the inset in Fig. 2.7, we observe that the mean μ and squared scale parameter σ^2 scale linearly with $1/N$. In particular we note that σ^2 seems to approach zero in the thermodynamic limit, as expected. Furthermore we note that the shape parameter ζ seems to be approximately independent of $1/N$ and to have a value of approximately 2 for all system sizes, thus suggesting that the distributions of pressures are consistent with a log-normal distribution.

Therefore, under the reasonable assumption (supported by the data) that the biased distribution of pressures $\mathcal{B}(x|V)$ is log-normal, we write the integrand in Eq. (2.25) as

$$\begin{aligned} I(x;\mu,\sigma,N) \equiv\ & \mathcal{B}(x|V)x^{N/\kappa} = \\ \frac{1}{x\sqrt{2\pi\sigma^2}} & \exp\left(-\frac{(\ln(x)-\mu)^2}{2\sigma^2}+\frac{N}{\kappa}\ln(x)\right), \end{aligned} \tag{2.28}$$

which is a unimodal distribution with mode $x_M = \exp(N\sigma^2/\kappa+\mu-\sigma^2)$. The distribution is such that

$$\Xi(\mu,\sigma,N) = \int_0^\infty I(x;\mu,\sigma,N)\,\mathrm{d}x = \exp\left[\frac{\sigma^2N^2}{2\kappa^2}+\frac{N\mu}{\kappa}\right]. \tag{2.29}$$

Since $\sigma^2 = s/N$ and $\mu = \mu_\infty + m/N$, where s and m are some constants, for large N we have

$$\lim_{N\to\infty}\frac{\Xi(\mu,\sigma,N)}{N} = \frac{\mu_\infty}{\kappa}+\frac{s}{2\kappa^2}. \tag{2.30}$$

Thus in the thermodynamic limit ($N, V, 1/\sigma^2 \to \infty$) we obtain the expression for the Boltzmann configurational entropy per particle, Eq. (2.26).

By replacing $c = \langle f \rangle_{\mathcal{B}} - \langle \Lambda \rangle_{\mathcal{B}}/\kappa$ from Eq. (D.4) into Eq. (2.26), we find

$$s_B(\phi_{\mathrm{SS}}) = 1 + \langle f \rangle_{\mathcal{B}} - \ln(\phi_{\mathrm{SS}}) - f_{\mathrm{ex}}(\phi_{\mathrm{HS}}) + \mathcal{O}\left((1/\kappa)^2\right), \tag{2.31}$$

hence the Gibbs and Boltzmann entropy per particles are identical in the thermodynamic limit up to a factor $s_B - s_G \propto (1/\kappa)^2 \geq 0$. In Chapter 3 we discuss how this bound is saturated in two dimensional systems as the unjamming density is approached.

Comments on the choice of fitting distributions

We note that, since the unbiased distribution $\mathcal{U}(P|N, \phi_{\mathrm{SS}})$ is peaked around high pressure states that are under-sampled by our biased protocol (low pressure states have typically larger basin volumes), the choice of fitting distribution for the observed (biased) distribution $\mathcal{B}(P|N, \phi_{\mathrm{SS}})$ and the quality of fit on the tails may have a significant effect on our numerical predictions. The same considerations are valid for the observed distributions of basin negative log-volumes $\mathcal{B}(F|N, \phi_{\mathrm{SS}})$ discussed in Sec. 2.6.2. To address the first issue, we make use of generalised Gaussian (Eq. E.1) and generalised log-normal (Eq. E.2) distributions: these families of distributions allow either for heavier than normal tails (shape factor $\zeta < 2$) or lighter than normal tails ($\zeta > 2$). The generalised Gaussian distribution allows to model a continuum of symmetric distributions going from the Laplace distribution ($\zeta = 1$) to the normal distribution ($\zeta = 2$) to the uniform distribution ($\zeta = \infty$) [153, 154]. The issue of the quality of fit on the tails can be essentially reduced to how accurate our estimate of the fitted shape parameter ζ is. While we are somewhat limited by the available statistics, our results show clear trends (in accordance with intuition) in the fitted parameters, see Fig. 2.5 and the inset of Fig. 2.7, suggesting that the results are meaningful. Furthermore, extrapolation in the thermodynamic limit indicates that the distributions are indeed Gaussian or log-normal ($\zeta_{N\to\infty} = 2$). For the case of the distribution of F, in Fig. 2.5 we also show that different fitting procedures for the generalised Gaussian model, or a non-parametric Kernel Density Estimate (KDE) model that relaxes the assumption of a symmetric distribution (described in Appendix E.3), yield results in good agreement. In the case of KDE with Gaussian kernels, the details of the tails of the distributions will depend on the bandwidth – acting as a smoothing parameter controlling the trade-off between bias and variance (which we optimize by cross-validation) – and the way the samples are distributed (the KDE density is simply the sum of the kernels located at the sample points, see Eq. E.3).

2.8 Conclusions

The study of a statistical mechanics of granular materials has been complicated by the impossibility of directly computing fundamental thermodynamic quantities. In this chapter we have shown that configurational entropies of three-dimensional packings can, in fact, be computed.

We have presented a method for the direct enumeration of the mechanically stable states of systems consisting of up to 128 frictionless soft three-dimensional spheres and we have shown that a definition of extensive entropy is possible, in line with the results for two dimensional systems reported by Asenjo *et al.* [34]. Compared to with Asenjo *et al.* [34], thanks to extensive algorithmic optimisation, our data benefit from more accurate basin volume estimations and improved statistics overall. A direct comparison of the Gibbs entropy in Fig. 2.1 (which does not rely on fits) clearly shows that our conclusions on the extensivity of the entropy are better supported by the data. Our analysis of the distribution of basin negative log-volumes $\mathcal{B}(F|N,\phi_{\mathrm{SS}})$, summarised in Fig. 2.5, is also consistent with that reported by Asenjo *et al.*, except for the shape parameter ζ that seems to be roughly constant ($\zeta \approx 2$) for all system sizes in 3D. Furthermore, as discussed in Sec. 2.7.1, we have tested the reliability of our results for the Boltzmann entropy S_B by fitting $\mathcal{B}(F|N,\phi_{\mathrm{SS}})$ using different fitting procedures and a non-parametric KDE model, finding excellent agreement between the different methods, see Fig. 2.5. In addition to Asenjo *et al.* we have also extended the discussion to the Edwards generalised (volume-stress) ensemble.

The study of 3D packings is computationally demanding: the computational time required for each packing ranged between 10 and 10^4 cpu hours, depending on system size. The present study therefore required substantial algorithmic optimisation.

We find that there is an approximately linear relationship between the logarithm of the pressure of a mechanically stable configuration and the logarithm of the volume of its basin of attraction.

The unexpected power law relationship between pressure and basin volume provides a way to extend our approach to the generalised Edwards ensemble. We can analytically unbias the observed distribution of pressures and compute the entropy as a function of pressure at a given volume. Hence we have obtained consistent expressions for the entropy in the thermodynamic limit. Knowledge of this distribution enables the first direct computation of angoricity.

Tackling the study of granular materials from the energy landscapes point of view is rather advantageous, although this does not come without burdens. This sort of approach is limited to soft frictionless particles, and we expect it to be reliable only at $\phi > \phi^J$ when the system is at least slightly over-compressed. Other theoretical approaches are useful in more limiting situations, see for instance the discussion of the stress ensemble in the limit $\phi \to \phi^J$ by Henkes and Chakraborty [66, 118] and the work on the force network ensemble for systems of almost hard grains [120–122].

Chapter 3

Are some packings more equal than others? A direct test of the Edwards conjecture

In the late 1980s, Sir Sam Edwards proposed a possible statistical-mechanical framework to describe the properties of disordered granular materials. A key assumption underlying the theory was that all jammed packings are equally likely. In the intervening years it has never been possible to test this bold hypothesis directly. Here we present simulations that provide direct evidence that at the unjamming point, all packings of soft repulsive particles are equally likely, even though generically, jammed packings are not. This is precisely the point at which experimental realisations of jammed granular systems are typically observed. Our results therefore support Edwards' original conjecture. We also present evidence that at unjamming the configurational entropy of the system is maximal.

— This chapter is based on Ref. [155]: Stefano Martiniani, K. Julian Schrenk, Kabir Ramola, Bulbul Chakraborty and Daan Frenkel, arXiv:1610.06328

3.1 Introduction

In science, most breakthroughs cannot be derived from known physical laws: they are based on inspired conjectures [156]. Comparison with experiment of the predictions based on such a hypothesis allows us to eliminate conjectures that are clearly wrong. However, there is a distinction between testing the consequences of a conjecture and testing the conjecture itself. A case in point is Edwards' theory of granular media. In the late 1980s, Edwards and Oakeshott [57] proposed that many of the physical properties of granular materials ('powders') could be predicted using a theoretical framework that was based on the assumption that all distinct packings of such a material are equally likely to be observed.

The logarithm of the number of such packings was postulated to play the same role as entropy does in Gibbs' statistical-mechanical description of the thermodynamic properties of equilibrium systems. However, statistical-mechanical entropy and granular entropy are very different objects. Until now, the validity of Edwards' hypothesis could not be tested directly – mainly because the number of packings involved is so large that direct enumeration is utterly infeasible – and, as a consequence, the debate about the Edwards hypothesis has focused on its consequences, rather than on its assumptions. Here we present results that show that now, at last, it is possible to test Edwards' hypothesis directly by numerical simulation. Somewhat to our own surprise, we find that the hypothesis appears to be correct precisely at the point where a powder is just at the (un)jamming threshold. However, at higher densities, the hypothesis fails. At the unjamming transition, the configurational entropy of jammed states appears to be at a maximum.

The concept of 'ensembles' plays a key role in equilibrium statistical mechanics, as developed by J. Willard Gibbs, well over a century ago [91]. The crucial assumption that Gibbs made in order to arrive at a tractable theoretical framework to describe the equilibrium properties of gases, liquid and solids was that, at a fixed total energy, every state of the system is equally likely to be observed. The distinction between, say, a liquid at thermal equilibrium and a granular material is that in a liquid, atoms undergo thermal motion whereas in a granular medium (in the absence of outside perturbations) the system is trapped in one of many (very many) local potential energy minima. Gibbsian statistical mechanics cannot be used to describe such a system. The great insight of Edwards was to propose that the collection of all stable packings of a fixed number of particles in a fixed volume might also play the role of an 'ensemble' and that a statistical-mechanics like formalism would result if one assumed that all such packings were equally likely to be observed, once the system had settled into a mechanically stable 'jammed' state. The nature of this ensemble has been the focus of many studies [57, 61, 63, 157].

Jamming is ubiquitous and occurs in materials of practical importance, such as foams, colloids and grains when they solidify in the absence of thermal fluctuations. Decompressing such a solid to the point where it can no longer achieve mechanical equilibrium leads to unjamming. Studies of the unjamming transition in systems of particles interacting via soft, repulsive potentials have shown that this transition is characterized by power-law scaling of many physical properties [158–163]. However, both the exact nature of the ensemble of jammed states and the unjamming transition remain unclear.

We present a *direct test* of the Edwards conjecture, using a numerical scheme for computing basin volumes of distinct jammed states (energy minima) of N polydisperse, frictionless disks held at a constant packing fraction ϕ. Uniquely, our numerical scheme allows us to

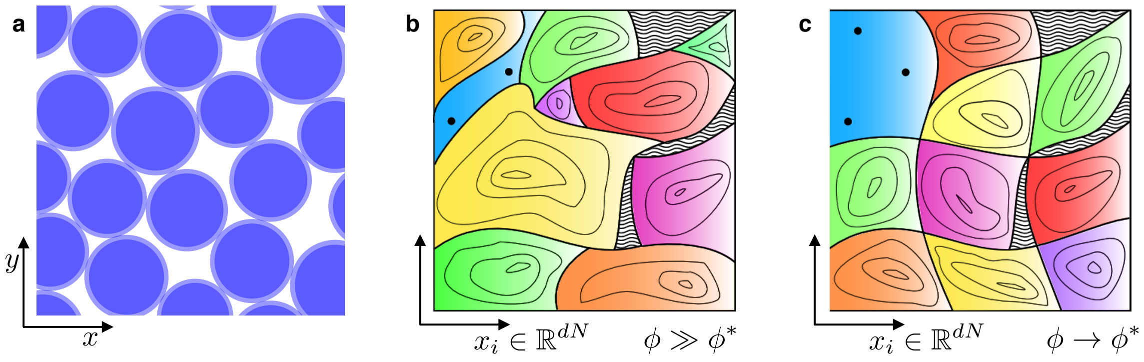

Fig. 3.1 (a) Snapshot of a jammed packing of disks with a hard core (dark shaded regions) plus soft repulsive corona (light shaded regions). (b)-(c) Illustration of configurational space for jammed packings. The dashed regions are inaccessible due to hard core overlaps. Single coloured regions with contour lines represent the basins of attraction of distinct minima. The dark blue region with solid dots indicates the coexisting unjammed fluid region and hypothetical marginally stable packings, respectively. The volume occupied by the fluid V_{unj} is significant only for finite size systems at or near unjamming. When $\phi \gg \phi^*$ (b) the distribution of basin volumes is broad but as $\phi \to \phi^*$ (c) the distribution of basin volumes approaches a delta function satisfying Edwards' hypothesis.

compute Ω, the number of distinct jammed states, and the individual probabilities $p_{i\in\{1,\ldots,\Omega\}}$ of each observed packing to occur. Fig. 3.1a shows a snapshot of a section of the system, consisting of particles with a hard core and a soft shell. Details of the system were discussed in Sec. 2.3.2.

3.2 Packing preparation protocol

We obtain jammed packings by equilibrating a hard disk fluid and inflating the particles instantaneously to obtain the desired soft-disk volume fractions (ϕ), followed by energy minimization using FIRE [144], as described in Sec 2.3.1. The particle radii are sampled from a truncated Gaussian distribution with mean $\mu = 1$ and standard deviation $\sigma_{\text{HS}} = 0.1$. In our simulations, we considered all mechanically stable packings, irrespective of the number of 'rattlers'. To guarantee mechanical stability we required that the total number of contacts is sufficient for the bulk modulus to be strictly positive, $N_{\text{min}} = d(N_{nr} - 1) + 1$ [164], where N_{nr} is the number of non-rattlers and d the dimensionality of the system.

The minimization procedure finds individual stable packings with a probability p_i proportional to the volume v_i of their basin of attraction. Averages computed using this procedure, represented by $\langle \ldots \rangle_{\mathcal{B}}$, would then lead to a bias originating from the different v_i's. The numerical methods introduced in Refs [32, 34–36] and discussed in Chapt. 2, 4, 5 have enabled the direct computation of v_i, and therefore, an unbiased characterization of the phase space.

3.3 Results: Equiprobability of states

We report a detailed analysis of the distribution of basin volumes v_i for a system of $N = 64$ disks. We compute v_i using a thermodynamic integration scheme [32, 34–36] described in Sec. 2.4 and summarised in Sec. 2.5, and compute the average basin volume $\langle v \rangle(\phi)$. The number of jammed states is, explicitly, $\Omega(\phi) = \mathcal{V}_J(\phi)/\langle v \rangle(\phi)$, where $\mathcal{V}_J(\phi)$ is the total available phase space volume at a given ϕ, see Appendix C for details of its derivations. Furthermore, we perform finite size scaling analysis to locate the (un)jamming density and to establish a relation with Edwards' hypothesis.

3.3.1 Summary of calculations

For the basin volume calculations we consider systems of $N = 64$ disks sampled at a range of 8 volume fractions $0.828 \leq \phi \leq 0.86$ and for each ϕ we measure the basin volume for about $365 < M < 770$ samples.

For the finite size scaling analysis of the relative pressure fluctuations we study system sizes $N = 32, 48, 64, 80, 96, 128$ for 48 volume fractions in the range $0.81 \leq \phi \leq 0.87$. For each system size we generate up to 10^5 hard disk fluid configurations and compute the pressure for between approximately 10^3 and 10^4 jammed packings (depending on the probability of obtaining a jammed packing at each volume fraction).

Simulations were performed using the open source libraries PELE [140] and MCPELE [137]. While presenting data from our computations, we express pressure and volume in reduced units as P/P^* and v/v^* respectively. The unit of volume is given by $v^* \equiv \pi \langle r_{HS}^2 \rangle$, where $\langle r_{HS}^2 \rangle$ is the mean-squared hard sphere radius. The unit of pressure is then $P^* \equiv \varepsilon / v^*$, where ε is the stiffness of the soft-sphere potential, defined in Eq. (2.5). The pressure is computed as $P = \mathrm{Tr}(\hat{\Sigma})/2V_{\mathrm{box}}$ where $\hat{\Sigma}$ is the Virial stress tensor and V_{box} the volume of the enclosing box.

Errors were computed analytically where possible and propagated using the 'uncertainties' Python package [165]. Alternatively, intervals of confidence were computed by bootstrap for the covariance estimation [166] and by BCa bootstrap otherwise using the 'scikit-bootstrap' Python package [167, 168]

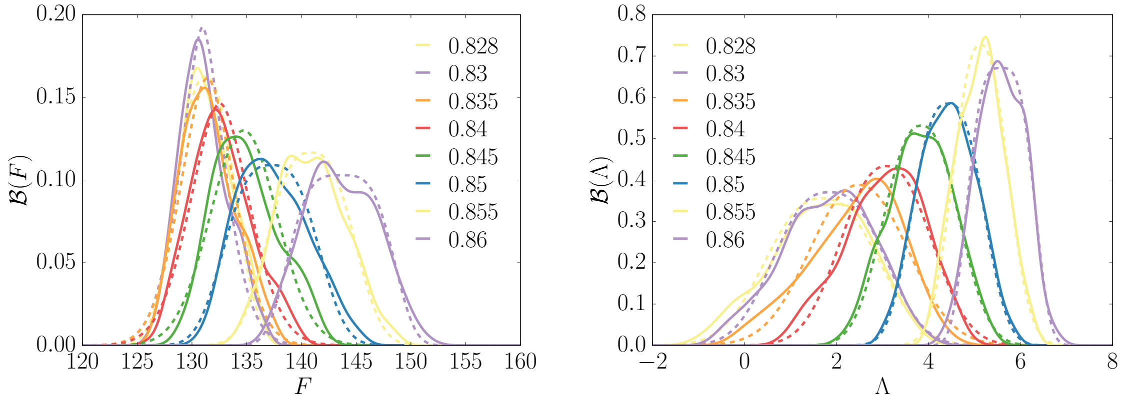

(a) (b)

Fig. 3.2 Observed distribution of the basin negative log-volume F (a) and log-pressure Λ (b) for jammed packings of $N = 64$ HS-WCA polydisperse disks at various volume fractions $0.828 \le \phi \le 0.86$. Solid lines are Kernel Density Estimates and dashed lines are generalised Gaussian fits.

We remove outliers from the log-volume and pressure distributions following the distance-based outlier removal method introduced by Knorr and Ng [152] described in Appendix E.4, with $D = 4\sigma$, $R = 0.5$.

Distributions of basin negative log-volumes ($F = -\ln v_{\text{basin}}$) were fitted using either a generalised Gaussian distribution (Eq. E.1) or non-parametric Kernel Density Estimates (described in Appendix E.3). A discussion of the choice of fitting distributions has been given in Sec. 2.7.3. Note that we also prefer KDE to histograms to circumvent the influence of binning on the visualisation and interpretation of the data[1].

3.3.2 Distributions of basin volumes and pressures

To characterize the distribution of basin volumes, we analyse the statistics of v_i along with the pressure P_i of each packing. It is convenient to study $F_i \equiv -\ln v_i$ as a function of $\Lambda_i \equiv \ln P_i$. Before fitting the marginal distributions, we perform an additional step of outlier detection based on an elliptic (Gaussian) envelope criterion described in Appendix E.5.1. The procedure is strictly unsupervised and allows us to achieve robust fits despite the small sample sizes. In Fig. 3.2 we show the biased distributions $\mathcal{B}(F)$ and $\mathcal{B}(\Lambda)$ of the basin log-volumes and log-pressure, which are the marginal distributions of the joint distribution $\mathcal{B}(F,\Lambda)$ shown in Fig. 3.4. We fit the marginal distributions using both a (parametric) generalised Gaussian

---

[1] As far as visualisation is concerned, the choice of kernel will also have an effect but, if properly cross-validated, less serious than the arbitrary choice of binning.

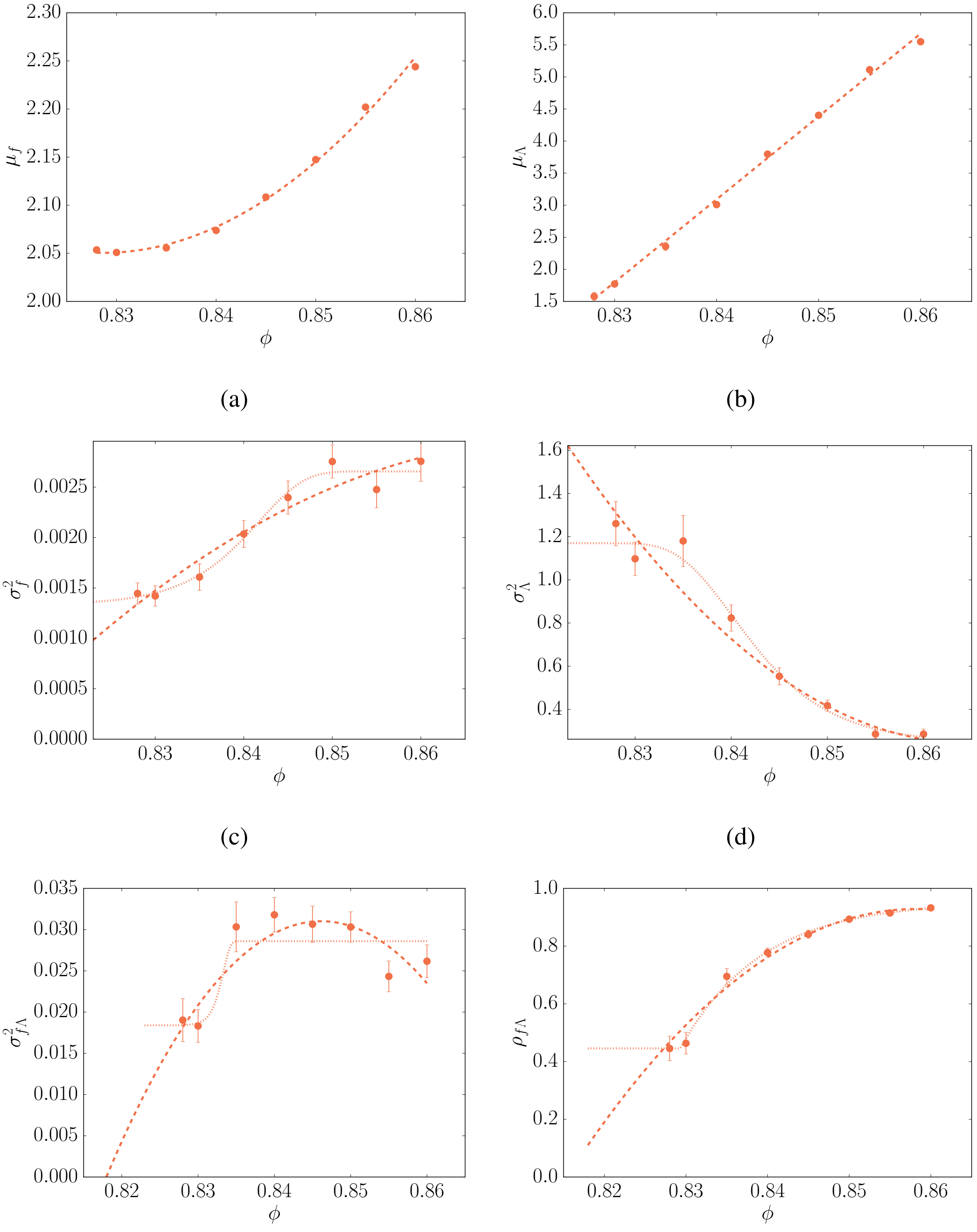

(a) (b)

(c) (d)

(e) (f)

Fig. 3.3 Moments of the joint distribution $\mathcal{B}(f,\Lambda)$ for jammed packings of $N = 64$ HS-WCA polydisperse disks at various volume fractions $0.828 \leq \phi \leq 0.86$. Elements of the mean $\boldsymbol{\mu} = (\mu_f, \mu_\Lambda)$ are shown in (a) and (b) respectively. Elements of the covariance matrix $\hat{\sigma} = ((\sigma_f^2, \sigma_{f\Lambda}^2), (\sigma_{f\Lambda}^2, \sigma_\Lambda^2))$ are shown in (c)-(e). The linear correlation coefficient $\rho_{f\Lambda} = \sigma_{f\Lambda}^2/(\sigma_f \sigma_\Lambda)$ is shown in (f). All values are computed by the MCD estimator with 0.99 support fraction over 1000 bootstrap samples. Error bars are standard errors computed by bootstrap. Dashed lines are second order polynomial fits and dotted lines are sigmoid fits (Eq. (E.4)). Curves of best fit are meant as guide to the eye.

model [154] and a (non-parametric) kernel density estimate (KDE), see Appendix E for a description. We compute the Boltzmann entropy S_B by unbiasing and integrating the resulting fits for $\mathcal{B}(F)$ as described in Sec. 2.6.2.

In has been shown [169] that in the limit $N \to \infty$ the shape parameter for the generalised Gaussian fit to $\mathcal{B}(F)$ approaches that of a standard Gaussian distribution $\zeta = 2$, consistently with our findings for three-dimensional packings, see Fig. 2.5. Since we also have that $\sigma_F^2 \sim N$ and $\mu_F \sim N$, we can write

$$e^{-(F-\mu_F)^2/(2\sigma^2)} \sim e^{-N(f-\mu_f)^2} \to \delta(\mu_f) \text{ as } N \to \infty, \tag{3.1}$$

where δ is the Dirac delta function and $f = F/N$. The distribution of basin volumes thus becomes infinitely narrow in the thermodynamic limit. However, this is not sufficient for the Edwards conjecture to be correct, in fact we also require that the basin volumes are uncorrelated with respect to any structural observables in this limit, consistently with what has been found in Sec 2.7.3. In what follows we show that this occurs only as $\phi \to \phi^*$.

In Fig. 3.3 we plot the moments of $\mathcal{B}(f,\Lambda)$, namely the elements of the mean $\boldsymbol{\mu} = (\mu_f, \mu_\Lambda)$ and the elements of the covariance matrix $\hat{\sigma} = ((\sigma_f^2, \sigma_{f\Lambda}^2), (\sigma_{f\Lambda}^2, \sigma_\Lambda^2))$, as well as the linear correlation coefficient $\rho_{f\Lambda} = \sigma_{f\Lambda}^2/(\sigma_f \sigma_\Lambda)$. Mean and covariance estimates of $\mathcal{B}(f,\Lambda)$ are computed using a robust covariance estimator described in Appendix E.5 with support fraction $h/n_{\text{samples}} = 0.99$. We use these robust estimates of the location and of the covariance matrix (computed over 1000 bootstrap samples [166]) to fit our observations by linear minimum mean square error (MMSE) [170], see Fig.3.4, and to compute the Gibbs entropy S_G.

3.3.3 Convergence of Gibbs and Boltzmann entropy

A convenient way to check equiprobability is to compare the Boltzmann entropy $S_B = \ln\Omega - \ln N!$, which counts all packings with the same weight, and the Gibbs entropy $S_G = -\sum_i^\Omega p_i \ln p_i - \ln N!$, see Sec. 2.6 for a detailed discussion. The Gibbs entropy satisfies $S_G \leq S_B$, saturating the bound when all p_i are equal, namely $p_{i\in\{1,\ldots,\Omega\}} = 1/\Omega$. As shown in Fig. 3.4a, S_G approaches S_B from below as $\phi \to \phi_{N=64}^{*(S)} \approx 0.823$. Fig. 3.1b-c schematically illustrates the evolution of the basin volumes as the packing fraction is reduced.

3.3.4 Decoupling of basin volume and pressure

As shown in Fig. 3.4b, we observe a strong correlation between F_i and Λ_i which we quantify by fitting the data to a bivariate Gaussian distribution. The conditional expectation of F given Λ then yields a linear relationship (denoted by solid lines in Fig. 3.4b) such that

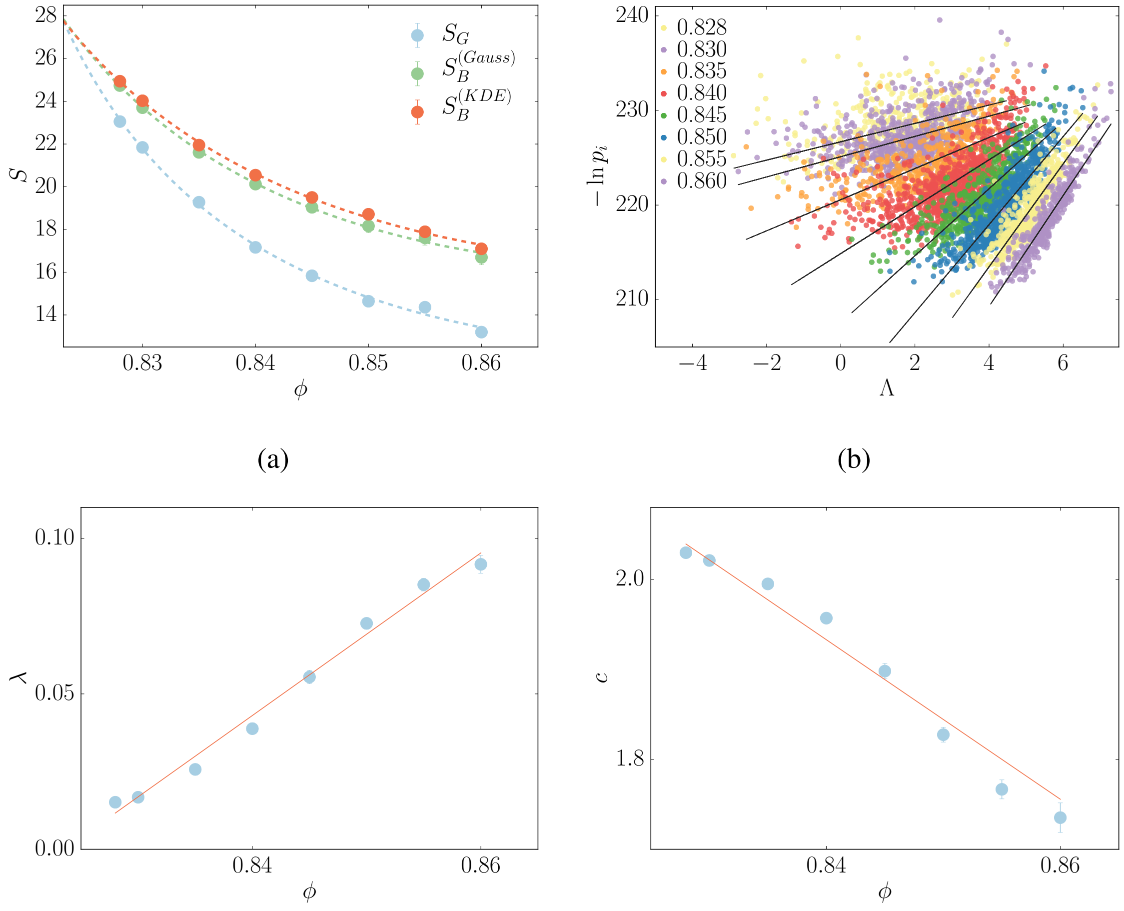

(a) (b)

(c) (d)

Fig. 3.4 (a) Gibbs entropy S_G and Boltzmann entropy S_B as a function of volume fraction. S_B is computed both parametrically by fitting $\mathcal{B}(f)$ with a generalised Gaussian function (‘Gauss’) and non-parametrically by computing a Kernel Density Estimate (‘KDE’) as in Ref.[35]. Dashed curves are a second order polynomial fit. (b) Scatter plot of the negative log-probability of observing a packing, $-\ln p_i = F_i + \ln \mathcal{V}_J(\phi)$, where $\mathcal{V}_J$ is the accessible fraction of phase space (see Appendix C) as a function of log-pressure, Λ. Black solid lines are lines of best fit computed by linear minimum mean square error using a robust covariance estimator and bootstrap (see Appendix E.5). (c) Slopes $\lambda(\phi)$ and (d) intercepts $c(\phi)$ of linear fits for Eq. (3.2). Solid lines are lines of best fit and error bars refer to the standard error computed by bootstrap.

	λ	$S_B^{(Gauss)}$	$S_B^{(KDE)}$
$\phi^*_{N=64}$	0.824 ± 0.070	0.823	0.823
$\langle z \rangle_{\mathrm{sig}}(\phi^*_{N=64})$	4.050 ± 0.24	4.048	4.048

Table 3.1 Predicted values of $\phi^*_{N=64}$ obtained from the linear extrapolation of $\lambda \to 0$ and from the point of intersection of the Gibbs entropy S_G with the Boltzmann entropy S_B, computed both parametrically by fitting $\mathcal{B}(f)$ with a generalised Gaussian function (‘Gauss’) and non-parametrically by computing a Kernel Density Estimate (‘KDE’) of the distribution. The corresponding average contact number has been computed using a sigmoid fit to the data.

$\langle F \rangle_{\mathcal{B}}(\phi;\Lambda) \propto \lambda(\phi)\Lambda^2$, where $\langle F \rangle_{\mathcal{B}}(\phi;\Lambda)$ represents the average over all basins at a given Λ. In Chapt. 2 we have shows that this relationship also exists for three-dimensional packings and that it is preserved in the thermodynamic limit. Defining $f = F/N$, we have (see Appendix D for a derivation):

$$\begin{aligned} \langle f \rangle_{\mathcal{B}}(\phi;\Lambda) =& \lambda(\phi)\Lambda + c(\phi) \\ =& \lambda(\phi)\Delta\Lambda + \langle f \rangle_{\mathcal{B}}(\phi) \ , \end{aligned} \tag{3.2}$$

where $\Delta\Lambda = \Lambda - \langle \Lambda \rangle_{\mathcal{B}}(\phi)$. For Edwards’ hypothesis to be valid, we require that in the thermodynamic limit (i) the distribution of volumes approaches a Dirac delta, which follows immediately from the fact that the variance $\sigma_f^2 \sim 1/N$ [34], see Sec. 3.3.2 for a derivation, and (ii) F_i needs to be independent of Λ_i, as well as of all other structural observables, and therefore $\lambda(\phi)$ must necessarily vanish. As can be seen from Fig. 3.4c-d, within the range of volume fractions studied, $\lambda(\phi)$ decreases but saturates to a minimum as $\phi \to \phi^{*(\lambda)}_{N=64}$. We argue below that the saturation is a finite size effect. An extrapolation using the linear regime in Fig. 3.4c indicates that $\lambda \to 0$ at packing fraction $\phi^{*(\lambda)}_{N=64} = 0.824 \pm 0.070$, remarkably close to where our extrapolation yields $S_G = S_B$ (extrapolated densities are summarised in Table 3.1). The analysis of basin volumes, therefore, strongly suggests that equiprobability is approached only at a characteristic packing fraction and that the vanishing of $\lambda(\phi)$ can be used to estimate the point of equiprobability.

We next show that $\lambda(\phi)$ does indeed tend to zero in the thermodynamic limit. We use the fluctuations σ_f^2, σ_Λ^2, and the covariance $\sigma_{f\Lambda}^2$, obtained from the elements of the covariance matrix $\hat{\sigma} = ((\sigma_f^2, \sigma_{f\Lambda}^2), (\sigma_{f\Lambda}^2, \sigma_\Lambda^2))$ of the joint distribution of f and Λ to define λ and c (see

---

[2] Note we relabelled $\lambda \equiv 1/\kappa$ from Sec. 2.7.2

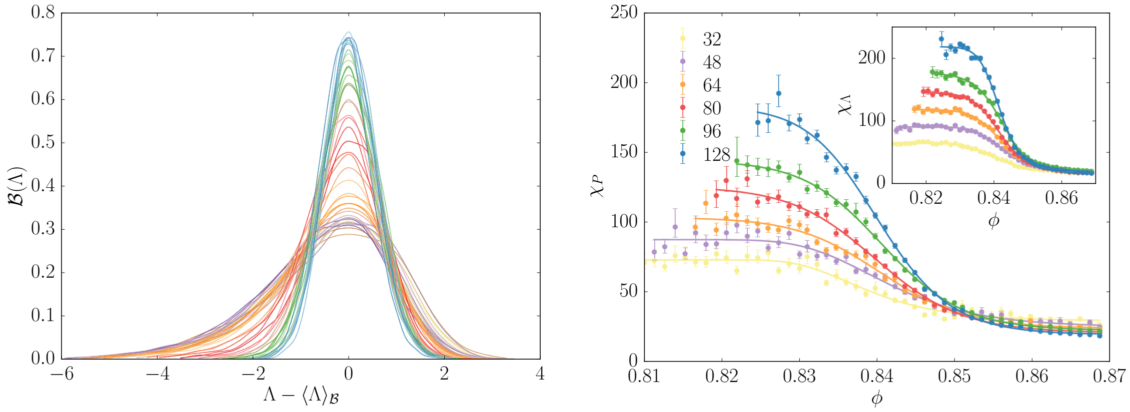

(a) (b)

Fig. 3.5 (a) Log-transformed observed (biased) distribution of pressures for jammed packings of $N = 64$ HS-WCA polydisperse disks, centred around the mean. The variance grows for decreasing volume fractions and becomes more skewed towards low pressures. The overall Gaussian shape is consistent with a log-normal distribution of pressures. Curves are kernel density estimates with Gaussian kernels, see Appendix E for a description. (b) $\chi_P \equiv N\sigma^2(P/\langle P\rangle_{\mathcal{B}})$ and (inset) $\chi_\Lambda \equiv N\sigma^2_\Lambda$, plotted as a function of volume fraction ϕ. For $\phi \gg \phi^*_N$, χ_P approaches a constant value indicating the absence of correlations far from the transition. Error bars, computed by BCa bootstrap [167], refer to 1σ confidence intervals. Solid lines are generalised sigmoid fits defined as in Eq. (E.4). We only show values of ϕ where the probability of finding a jammed packing is at least 1%, so that the observables are computed over sufficiently large samples.

Appendix D) as:

$$\begin{aligned} \lambda(\phi) &\equiv \frac{\sigma^2_{f\Lambda}(\phi)}{\sigma^2_\Lambda(\phi)}, \\ c(\phi) &\equiv \langle f\rangle_{\mathcal{B}}(\phi) - \frac{\sigma^2_{f\Lambda}(\phi)}{\sigma^2_\Lambda(\phi)}\langle\Lambda\rangle_{\mathcal{B}}(\phi). \end{aligned} \tag{3.3}$$

From Fig. 3.4b we observe that the decrease of λ is driven by σ^2_Λ increasing to a maximum, while σ^2_f and $\sigma^2_{f\Lambda}$ decrease, see Fig. 3.3. We expect the main features of these distributions to be preserved as the system size N is increased [35], which suggests that for larger N, where basin volume calculations are still intractable for multiple densities, the maximum in σ^2_Λ can be used to identify ϕ^*_N. We have directly measured $\chi_\Lambda = N\sigma^2_\Lambda$ using our sampling scheme – that samples packings with probability proportional to the volume of their basin of attraction – for systems of up to $N = 128$ disks (see inset of Fig. 3.5b) and finite size scaling indicates that χ_Λ diverges as $\phi \to \phi^*_{N\to\infty} = 0.841(3)$, see Sec. 3.3.6. The saturation of λ to a minimum as $\phi \to \phi^*_N$, for small N, is determined by the fact that χ_Λ only diverges in the thermodynamic limit, a detailed discussion is given in Sec. 3.3.7.

Returning to the $N = 64$ case that we have analysed using the basin volume statistics, we find that our estimate $\phi^*_{N=64} = 0.824(70)$ where $S_G = S_B$ and $\lambda \to 0$, falls precisely in this region where χ_Λ saturates to its maximum value. In addition, the average number of contacts $\langle z \rangle_{\mathcal{B}}(\phi^*_{N=64}) = 4.05 \pm 0.24$ is close to the isostatic value $z^{(iso)}_{N=64} \equiv 2d - 2/64 \approx 3.97$ [161].

3.3.5 Correlations with other structural parameters

We analyse the correlation of the basin negative log-volume with a number of structural parameters other than the pressure, that we have just discussed. For all observables Y we assume a linear correlation defined analogously to Eq. (3.2), namely

$$\langle f \rangle_{\mathcal{B}}(\phi; Y) = \lambda_Y(\phi) \ln Y + c_Y(\phi). \tag{3.4}$$

We perform the analysis for the individual elements of the stress tensor $\hat{\Sigma}_{ij}$, the average contact number z and the Q_6 bond-orientational order parameter [171]. Scatter plots with bootstrapped linear MMSE fits are shown in Fig. 3.6 (except for the diagonal elements of $\hat{\Sigma}$ that are essentially identical to Fig. 3.4b), and the fitted parameters are plotted as a function of volume fraction in Fig. 3.7. The results are qualitatively similar to those obtained for the pressure in that λ_Y is decreasing towards 0 as $\phi \to \phi^*$, indicating that the basin volumes decorrelate from Y in this limit, this being a necessary condition for the equiprobability of jammed states.

In Fig. 3.6b, we observe that λ_{Q_6} becomes precisely zero at the lowest ϕ, while for larger volume fractions $\lambda_{Q_6} < 0$, implying that larger basins correspond to more ordered structures. At the same time we note from Figs. 3.6c-d that larger volumes correspond on average to lower average contact numbers z, and that z and Q_6 are (therefore) negatively correlated for disordered packings.

3.3.6 Finite size scaling analysis

Interestingly, we find evidence that in the thermodynamic limit, the point of equiprobability $\phi^*_{N\to\infty}$, coincides with the point at which the system unjams, $\phi^J_{N\to\infty}$. We use two characteristics of the unjamming transition to locate $\phi^J_{N\to\infty}$ (i) the probability of finding jammed packings, p_J, goes to zero (see Fig 3.8a) and (ii) the average pressure of the packings goes to zero, and therefore $\langle \Lambda \rangle \to -\infty$ (see Fig 3.9a).

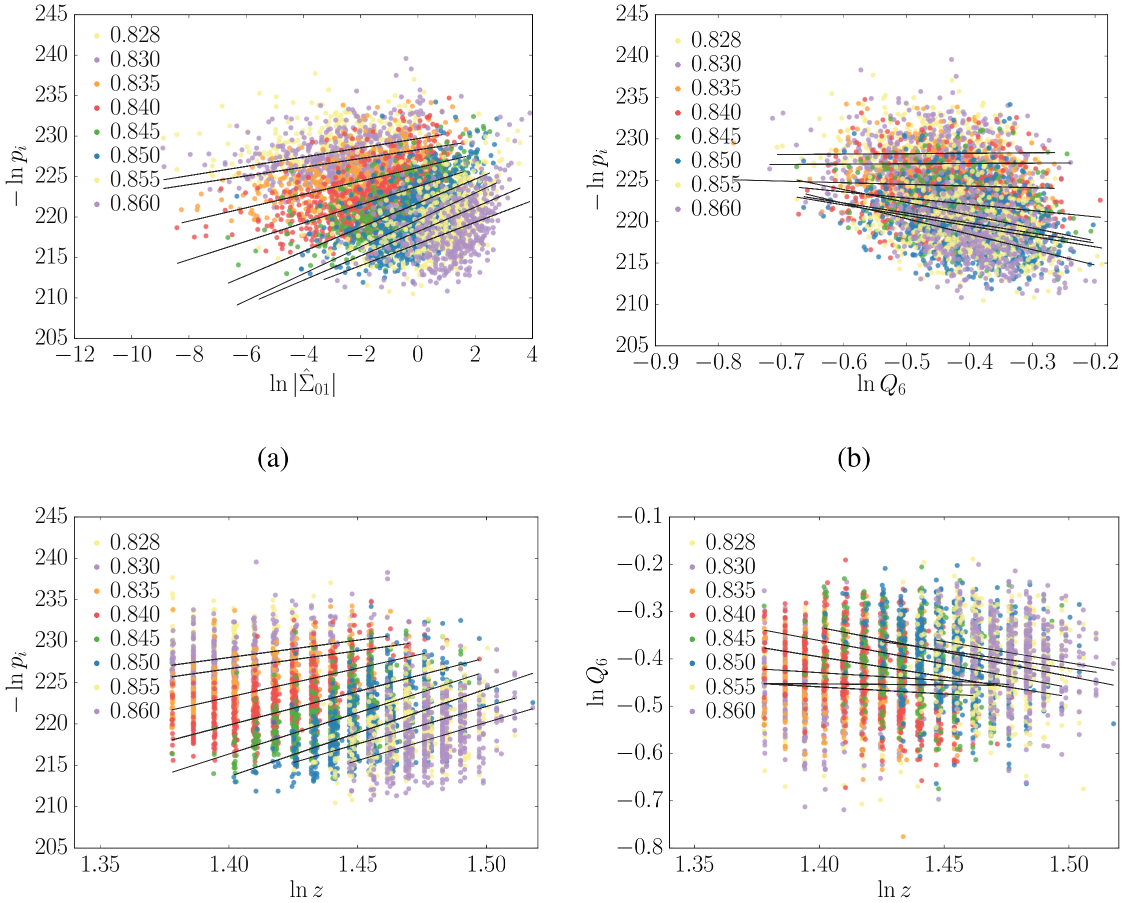

(a)

(b)

(c)

(d)

Fig. 3.6 Scatter plots of the negative log-probability of observing a packing, $-\ln p_i = F_i + \ln \mathcal{V}_J(\phi)$, where $\mathcal{V}_J$ is the accessible fraction of phase space, as a function of $\hat{\Sigma}_{01}$ (a), the Q_6 bond-orientational order parameter (b) and the average contact number z (c). The scatter plot in (d) shows the Q_6 bond-orientational order parameter as a function of the average contact number z. Black solid lines are lines of best fit computed by bootstrapped linear MMSE using a robust covariance estimator.

A finite size scaling collapse for $p_J L^{\beta/\nu}$ vs. $L^{1/\nu}\left(\phi/\phi^J_{N\to\infty} - 1\right)$, shown in the inset of Fig. 3.8a, yields critical exponents $\nu \approx 1$, $\beta = 0$ and critical volume fraction $\phi^{J(p_J)}_{N\to\infty} = 0.844(2)$, in agreement with Vagberg et al. [172]. O'Hern *et al.* [123, 173] produced similar estimates of the correlation length exponent and of the critical volume fraction by fitting the function $\phi^0_N - \phi^J_{N\to\infty} = \delta_0 L^{-1/\nu}$, where ϕ^0_N corresponds the position of the peaks for $\partial_\phi p_J$, shown in Fig. 3.8b. For a system of bidisperse disks O'Hern *et al.* found $\nu = 0.71(8)$ and $\phi^J_{N\to\infty} \approx 0.842$. A similar analysis of our data produces results in agreement with O'Hern *et al.*, namely $\nu = 0.6(3)$ and $\phi^J_{N\to\infty} \approx 0.840(3)$, but less accurate due to the smaller system

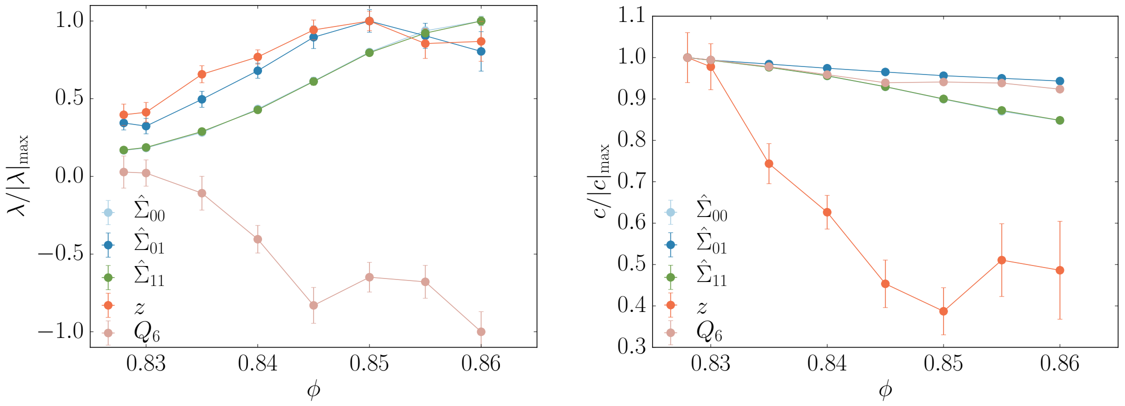

(a) (b)

Fig. 3.7 Slopes λ_Y (a) and intercepts c_Y (b) of Eq. (3.4) for the individual components of the stress tensor $\hat{\Sigma}$, the Q_6 bond-orientational order parameter, and the average contact number z. Estimates were obtained by bootstrapped linear MMSE fits using a robust covariance estimator and error bars refers to the standard error computed by bootstrap. Solid lines are guides to the eye.

sizes and the smaller sample size that we consider. Vagberg *et al.* [172] have shown that finite size corrections to scaling are important, such that when taken into account $\nu \approx 1$, in agreement with the scaling collapse for $\nu = 1$ shown in the inset of Fig. 3.8a. A finite size scaling collapse for $\langle\Lambda\rangle_{\mathcal{B}} L^{\xi/\nu}$ vs. $L^{1/\nu}\left(\phi/\phi^{J}_{N\to\infty}-1\right)$, shown in Fig. 3.9b, yields $\nu = 0.50(5)$, $\xi = 0.62(3)$ and critical volume fraction $\phi^{J(\Lambda)}_{N\to\infty} = 0.841(3)$.

We then analyse the relative pressure fluctuations $\chi_P = N\sigma^2(P/\langle P\rangle_{\mathcal{B}})$ and the log-pressure fluctuations $\chi_\Lambda = N\sigma^2_\Lambda$. A scaling collapse for different system sizes of $\chi_P L^{-\gamma/\nu}$ vs. $L^{1/\nu}\left(\phi/\phi^{*}_{N\to\infty}-1\right)$ with $L = N^{1/d}$, shown in Fig. 3.10a, yields $\nu = 0.5(3)$, $\gamma = 0.47(5)$ and $\phi^{*(P)}_{N\to\infty} = 0.841(3)$. An analogous scaling collapse of $\chi_\Lambda L^{-\gamma/\nu}$ vs. $L^{1/\nu}\left(\phi/\phi^{*}_{N\to\infty}-1\right)$, shown in Fig. 3.10b, yields $\nu = 0.5(3)$, $\gamma = 0.89(5)$ and $\phi^{*(\Lambda)}_{N\to\infty} = 0.841(3)$.

O'Hern *et al.* [123] measured the exponent with which the pressure vanishes for each individual packing as a function of $P \sim (\phi - \phi_c)^{\Psi}$, where ϕ_c is the unjamming volume fraction found by decompressing quasi-statically each individual configuration. They find that $\psi = \alpha - 1$, where α is the exponent of a short-range inverse power potential. Near unjamming we find $\alpha = 2$, as shown in Sec. 2.3.2, and therefore we expect $\psi = 1$. Our finite size scaling analysis is performed with respect to a unique ϕ^J (for all configurations) and we have not performed a systematic study for different potentials to establish a precise relationships between α and β or γ, which seem to fall approximately in the range 0.5 to

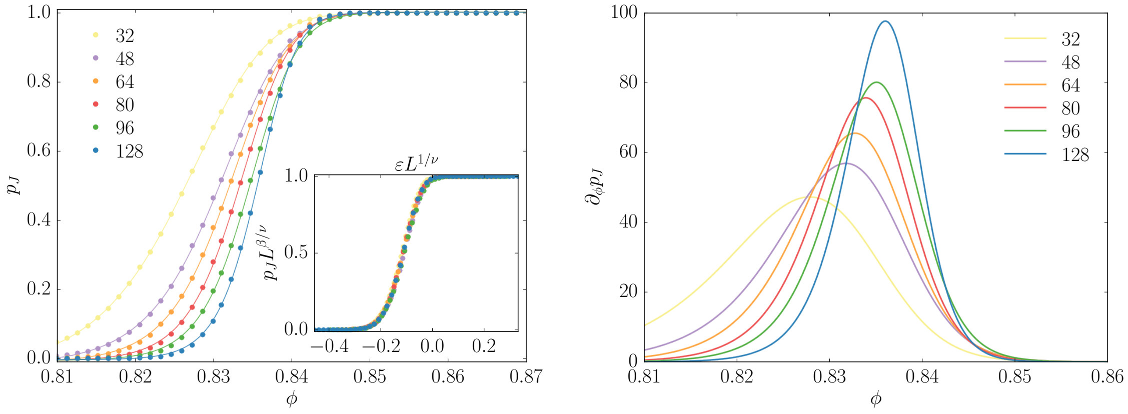

(a) (b)

Fig. 3.8 (a) Probability of obtaining a jammed packing p_J by our preparation protocol for $N = 32$ to 128 HS-WCA polydisperse disks as a function of volume fraction. Inset: Scaling collapse for $p_J L^{\beta/\nu}$ vs. $L^{1/\nu}\left(\phi/\phi^J_{N\to\infty} - 1\right)$, with $L = N^{1/d}$, yields critical exponents $\nu \approx 1$, $\beta = 0$ and critical volume fraction $\phi^{J(p_J)}_{N\to\infty} = 0.844(2)$. Circles are observed data and solid lines correspond to sigmoid fits, Eq. (E.4). (b) Derivative of the sigmoid fits for p_J for different numbers of disks.

1. A broader investigation, which goes beyond the scope of this work, will be necessary to establish a precise relationship.

Together these results lead us to conclude that the point of equiprobability $\phi^*_{N\to\infty}$ coincides with the unjamming point $\phi^J_{N\to\infty}$, to within numerical error and up to corrections to finite size scaling. Note that the precise numerical value of ν varies through the literature and has been shown to depend on the quantity being observed, and also crucially on finite size corrections to scaling [172]. In this work we have not attempted to establish ν definitely, nor elucidate its origin with respect to the diverging correlation length(s) that might be involved.

Our simulations therefore lead to the surprising conclusion that the Edwards conjecture appears to hold precisely at the (un)jamming transition.

Diverging relative pressure fluctuations

Why is χ_Λ related to the unjamming transition? As the particles interact via purely repulsive potentials, P is strictly positive, which implies that the fluctuations of P have a floor and go to zero at unjamming. The *relative* fluctuations $\chi_P \equiv N\sigma^2\left(P/\langle P\rangle_{\mathcal{B}}\right)$, can be non-zero, and a diverging χ_P would then imply a diverging χ_Λ. Because of the bounded nature of P [118, 174, 175], however, χ_P can *only* diverge at the unjamming transition where $\langle P\rangle_{\mathcal{B}} \to 0$, see

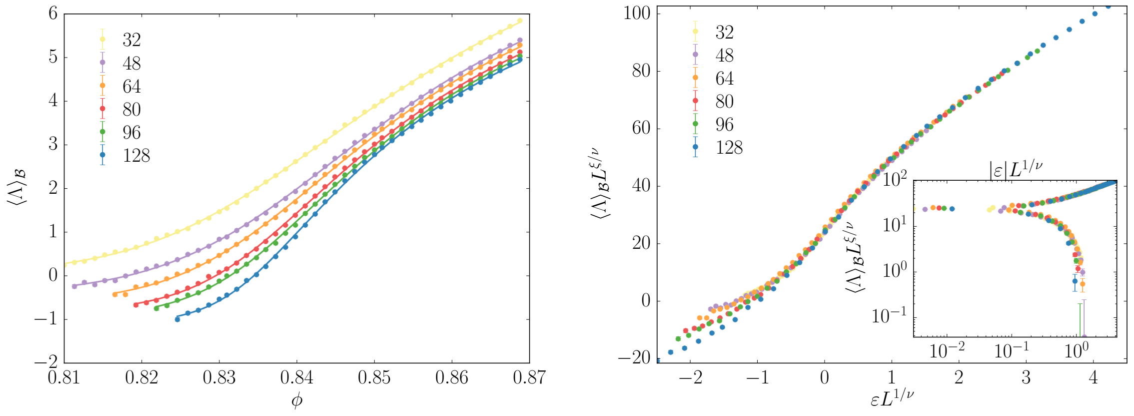

(a)

(b)

Fig. 3.9 (a) Average log-pressure $\langle\Lambda\rangle_{\mathcal{B}}$ for N HS-WCA polydisperse disks. (b) Scaling collapse for $\langle\Lambda\rangle_{\mathcal{B}}L^{\xi/\nu}$ vs. $L^{1/\nu}\left(\phi/\phi^{J}_{N\to\infty}-1\right)$, with $L=N^{1/d}$. The estimated critical exponents are $\nu=0.50(5)$ and $\xi=0.62(3)$, and the critical volume fraction $\phi^{J(\Lambda)}_{N\to\infty}=0.841(3)$. Inset: A logarithmic plot of the same data. Circles are observed data and solid lines are sigmoid fits, Eq. (E.4). Error bars, computed by BCa bootstrap [167], refer to 1σ confidence intervals.

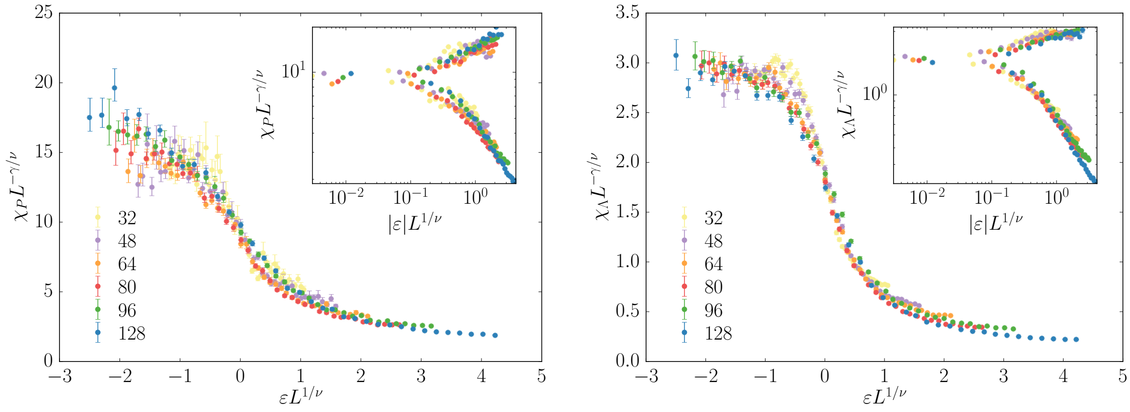

(a)

(b)

Fig. 3.10 (a) Data collapse from finite size scaling analysis of the variance of the relative pressures. The plot shows $\chi_P L^{-\gamma/\nu}$ vs. $L^{1/\nu}\left(\phi/\phi^{J}_{N\to\infty}-1\right)$, with $L=N^{1/d}$. The estimated critical exponents are $\nu=0.5(3)$ and $\gamma=0.47(5)$, and the critical volume fraction is $\phi^{*(P)}_{N\to\infty}=0.841(3)$. (b) Scaling collapse of the variance of the log-pressures. The plot shows $\chi_\Lambda L^{-\gamma/\nu}$ vs. $L^{1/\nu}\left(\phi/\phi^{*}_{N\to\infty}-1\right)$. The estimated critical exponents are $\nu=0.5(3)$ and $\gamma=0.89(5)$, and the critical volume fraction is $\phi^{*(\Lambda)}_{N\to\infty}=0.841(3)$. Error bars, computed by BCa bootstrap, refer to 1σ confidence intervals.

Appendix F for a justification. We find that χ_P does diverge (Figs. 3.5a, 3.10) and finite size scaling yields $\phi^{*(P)}_{N\to\infty} = 0.841(3)$.

3.3.7 Scaling behaviour

Scaling at $\phi \gg \phi^*$

First we show that away from a critical point, the relative pressure fluctuations scale as $1/L^2$, where $L = \sqrt{N}$ and N is the number of particles. The internal Virial is defined by $P = \sum_{i=1,N} p_i$, where p_i is the particle level "pressure" given by $p_i = \sum_j \sum_{\alpha=1,2} \boldsymbol{r}^{\alpha}_{i,j} \boldsymbol{f}^{\alpha}_{i,j}$ where $\boldsymbol{r}^{\alpha}_{i,j}$ and $\boldsymbol{f}^{\alpha}_{i,j}$ are the contact vectors and contact forces, respectively. The variance of $P/\langle P\rangle$ is

$$\sigma^2(P/\langle P\rangle) = \frac{\langle P^2\rangle - \langle P\rangle^2}{\langle P\rangle^2} = \frac{\sum_{i=1}^N \sigma^2(p_i) + \sum_{i\neq j} \mathrm{cov}(p_i, p_j)}{\left(\sum_{i=1}^N \langle p_i\rangle\right)^2}. \tag{3.5}$$

When away from a critical point we expect $\sum_{i\neq j} \mathrm{cov}(p_i, p_j)$ to scale subextensively, and the variance of relative pressure fluctuations to be

$$\sigma^2(P/\langle P\rangle) = \frac{\sum_{i=1}^N \sigma^2(p_i)}{\left(\sum_{i=1}^N \langle p_i\rangle\right)^2} \sim \frac{1}{N} \tag{3.6}$$

hence the relative pressure fluctuations away from the critical point will scale as $1/N = 1/L^2$, and

$$\sigma^2(\Lambda) \approx \sigma^2(P/\langle P\rangle) \sim 1/L^2, \tag{3.7}$$

as can be verified in Fig. 3.5.

Second, we analyse the covariance of the basin negative log-volume per particle ($F/N = -\ln(v_{\mathrm{basin}})/N$) and the relative pressure fluctuations, $\mathrm{cov}(F/N, P/\langle P\rangle)$. Similarly to the internal Virial, we define the particle level basin negative log-volume f_i, such that $F = \sum_{i=1,N} f_i$. Then we have

$$\mathrm{cov}(F/N, P/\langle P\rangle) = \frac{\langle FP\rangle - \langle F\rangle\langle P\rangle}{N\langle P\rangle} = \frac{\sum_{i=1}^N \mathrm{cov}(f_i, p_i) + \sum_{i\neq j} \mathrm{cov}(f_i, p_j)}{N\sum_{i=1}^N \langle p_i\rangle}. \tag{3.8}$$

From the power-law relation between F and Λ we know that away from the critical point $\mathrm{cov}(f_i, p_i) > 0$ and we expect $\sum_{i\neq j} \mathrm{cov}(f_i, p_j)$ to scale subextensively in this region, hence

$$\mathrm{cov}(F/N, P/\langle P\rangle) = \frac{\sum_{i=1}^N \mathrm{cov}(f_i, p_i)}{N\sum_{i=1}^N \langle p_i\rangle} \sim \frac{1}{N}, \tag{3.9}$$

therefore

$$\mathrm{cov}(f,\Lambda) \approx \mathrm{cov}(f,P/\langle P\rangle) \sim 1/L^2, \tag{3.10}$$

where $f = F/N$. We can thus conclude that the slope of the power-law relation is

$$\lambda_{\phi \gg \phi^*} = \frac{\sigma^2(f,\Lambda)}{\sigma^2(\Lambda)} \sim \mathcal{O}(1), \tag{3.11}$$

In other words, λ is independent of system size, a fact that has been verified numerically in Sec. 2.7.2, see Fig. 2.6.

Scaling as $\phi \to \phi^*$

Near the critical point, as $\phi \to \phi^*$, the variance of Λ follows the scaling form

$$\sigma^2(\Lambda) \sim L^{\gamma/\nu - 2}, \tag{3.12}$$

with $\gamma/\nu \approx 1$ as found by finite size scaling, shown in Fig. 3.10. While we do not have a finite size scaling collapse for the covariance $\sigma^2(f,\Lambda)$, due to the high computational cost of performing the basin volume calculations for multiple system sizes, we do observe that for $N = 64$ the covariance decreases with respect to the "background" $1/L^2$ fluctuations as $\phi \to \phi^*$, see Fig. 3.3e. Thus, we do not expect $L^2\sigma^2(f,\Lambda)$ to diverge but rather that

$$\sigma^2(f,\Lambda) \lesssim L^{-2}, \tag{3.13}$$

Hence in the limit $\phi \to \phi^*$ we find that the slope of the power-law relation becomes

$$\lambda_{\phi \to \phi^*} = \frac{\sigma^2(f,\Lambda)}{\sigma^2(\Lambda)} = 0. \tag{3.14}$$

Relation between scaling exponents

Starting from Eq. (3.2), we use the fact that $\sigma^2(aX \pm bY) = a^2\sigma^2(X) + b^2\sigma^2(Y) \pm 2ab\,\mathrm{cov}(X,Y)$ to compute the variance of $f = F/N$ to find

$$\sigma_f^2 = \lambda^2\sigma_\Lambda^2 = (\sigma_{f\Lambda}^2)^2/\sigma_\Lambda^2 \tag{3.15}$$

By rearranging this expressions we find that

$$(\sigma_{f\Lambda}^2)^2/\sigma_f^2 = \sigma_\Lambda^2 \sim \begin{cases} L^{-2} \text{ for } \phi \gg \phi^* \\ L^{-\zeta} \text{ for } \phi \to \phi^* \end{cases} \tag{3.16}$$

where we have defined $\zeta \equiv 2-\gamma/\nu \approx 1$ as in Eq. (3.12) and as found by finite size scaling, shown in Fig. 3.10. For $\phi \to \phi^*$, by assuming scalings $\sigma^2_{f\Lambda} \sim L^{-\eta}$ and $\sigma^2_f \sim L^{-\vartheta}$, we find the following relation between scaling exponents

$$2\eta - \vartheta = \zeta \tag{3.17}$$

3.3.8 Equiprobability in the generalized Edwards ensemble

Finally, we note that the states in the generalized Edwards ensemble [61, 65, 66, 118] characterized by ϕ and P have basin volumes that are similar, if not identical, over the full range of ϕ that we have explored (see scatter plot in Fig. 3.4b), indicating that equiprobability in the stress-volume ensemble [61, 65] is a more robust formulation of the Edwards hypothesis. This observation is consistent with recent experiments [116].

3.4 Conclusions

We have reported numerical evidence supporting the existence of a flat measure at unjamming for 2D soft repulsive sphere systems. Although, the equiprobability of jammed states at a given packing fraction was posited by Edwards for jammed packings of hard particles, our analysis shows that for soft particles, the Edwards hypothesis is valid only for the marginally jammed states at $\phi^*_{N\to\infty} = \phi^J_{N\to\infty}$, where the jamming probability vanishes, the entropy is maximized, and relative pressure fluctuations diverge. We have shown not only that there exist a practical ‘Edwardsian’ packing generation protocol, capable of sampling jammed states equiprobably, but we have uncovered an unexpected property of the energy landscape for this class of systems. At this stage we cannot establish whether the same considerations are valid in 3D, although the already proven validity of Eq. (3.2) in 3D would suggest so [35], see Sec. 2.7.2. The exact value of the entropy at unjamming, whether finite or not, also needs to be elucidated. The implications for ‘soft’ structural glasses is apparent: at ϕ^J the uniform size of the basins implies that the system, when thermalised, has the same probability of visiting all of its basins of attraction, hence there are no preferred inherent structures. This could be a signature of the hard-sphere transition occurring at the same point [39]. Our approach can therefore be extended to spin-glasses and related problems, and it would be clearly very exciting to explore the analogies and differences between ‘jamming’ in various systems for which the configuration space can break up into many distinct basins.

Chapter 4

Structural analysis of high-dimensional basins of attraction

We propose an efficient Monte Carlo method for the computation of the volumes of high-dimensional bodies with arbitrary shape. We start with a region of known volume within the interior of the manifold and then use the multi-state Bennett acceptance-ratio method to compute the dimensionless free-energy difference between a series of equilibrium simulations performed within this object. The method produces results that are in excellent agreement with thermodynamic integration, as well as a direct estimate of the associated statistical uncertainties. The histogram method also allows us to directly obtain an estimate of the interior radial probability density profile, thus yielding useful insight into the structural properties of such a high dimensional body. We illustrate the method by analysing the effect of structural disorder on the basins of attraction of mechanically stable packings of soft repulsive spheres.

— This chapter is based on Ref. [36]: Stefano Martiniani, K. Julian Schrenk, Jacob D. Stevenson, David J. Wales, and Daan Frenkel, Phys. Rev. E **94**, 031301(R) (2016)

4.1 Introduction

In science we often face, and occasionally confront, the following question: "Can we estimate the *a priori* probability of observing a system in a very unlikely state?" An example is: "How likely is a given disordered sphere packing?", not to mention questions such as "How likely is life, or the existence of a universe like ours?" within the context of dynamical systems and of the multiverse. In a number of cases, where the states correspond to extrema in a high dimensional function, this question can be narrowed down to: "How large is the ‘basin of attraction’ of a given state?”. In such cases, estimating the probability of observing a particular state is equivalent to computing the volume of the (high-dimensional) basin of attraction of this state. That simplifies the problem, but not by much [176, 177]: analytical approaches are typically limited to highly symmetric (often convex) volumes, whilst ‘brute force’ numerical techniques can deal with more complex shapes, but only in low-dimensional cases. Computing the volume of an arbitrary, high-dimensional body is extremely challenging. For instance, it can be proved that the exact computation of the volume of a convex polytope is a NP-hard problem [178–180] and, of course, the problem does not get any easier in the non-convex case.

Yet, the importance of such computations is apparent: the volume of the basin of attraction for the extrema of a generic energy landscape, be that of biological molecules [37], an artificial neural network [45, 47, 48], a dynamical system [41, 42], or even of a “string theory landscape” (where the minima corresponds to different de Sitter vacua [51, 56]), is essential for understanding the systems’ behavior.

In high dimensions, simple quadrature and brute-force sampling fail [181] and other methods are needed. In statistical mechanics, the problem is equivalent to the calculation of the partition function (or, equivalently, the free energy) of a system, and several techniques have been developed to tackle this problem (see e.g [151]). The earliest class of techniques to compute partition functions is based on thermodynamic integration (TI) [151, 182, 183], which is based on the idea that a transformation of the Hamiltonian of the system can transform an unknown partition function into one that is known analytically. More recent techniques include histogram-based methods (Wang-Landau [184], parametric and non-parametric weighted histogram analysis method (WHAM) [185]) or Nested Sampling [186, 187]. In essence, all these techniques reduce the computation of the partition function to the numerical evaluation of a one-dimensional integral.

Among the above methods Nested Sampling and Wang Landau are Monte Carlo algorithms in their own right, that produce the (binned) density of states as a by-product. On the other hand, TI can be identified as a particular Umbrella Sampling scheme [151], that outputs multiple sets of equilibrium states that can be analysed, either by numerical quadrature (e.g. see the Einstein crystal method (ECM) [146] described in Appendix B), or by WHAM and multi-state Bennet acceptance ratio method (MBAR). All the above methods can be used to compute high-dimensional volumes. However, the choice of the MBAR method [188] is an optimal one. Not only is MBAR non-parametric (no binning is required) and the lowest known variance reweighting estimator for free energy calculations, but it also eliminates the need for explicit numerical integration of the density of states, thus reducing to a minimum the number of systematic biases.

One reason why brute force methods are not suited to estimate the volumes of high-dimensional bodies, is that for such bodies the volume of the largest inscribed hypersphere, quickly becomes negligible to the volume of the smallest circumscribed hypersphere – and most of the volume of the circumscribed hypersphere is empty. Hence, using a Monte Carlo ‘rejection method’ to compute the volume of the non-convex body as the fraction of volume contained in a hypersphere [124, 189], does not yield accurate results: the largest contribution should come from points that are barely sampled, if at all.

In this chapter we show that MBAR can be used, not only to arrive at an accurate estimate of a high-dimensional, non-convex volume, but that it can also be used to probe the spatial distribution of this volume.

4.2 Computing high-himensional volumes

4.2.1 Mathematical basis

Our aim is to measure the volume of a $n-$dimensional connected compact manifold $\Gamma \subseteq \mathbb{R}^n$ with boundaries. We require this body to be “well guaranteed”, *i.e.* it has both an inscribed and a circumscribed hypersphere [177]. To explore different parts of the non-convex volume, we use a spherically symmetric bias that either favors the sampling of points towards the center, or towards the periphery. We start by performing a series of $K+1$ random walks under different applied bias potentials, similarly to the Einstein-crystal method [146], described in Appendix B. We refer to each of the walkers as a “replica” R_i. Unlike TI, where biasing is always ‘attractive’ (*i.e.* it favors larger confinement), in MBAR we are free to choose both attractive and repulsive bias potentials. Additionally MBAR uses the full posterior distribution (hence all moments) rather than just the average log-likelihood computed over the posterior, as for TI. The present method directly yields an estimate for the statistical uncertainty in the results that depends on the full distributions and is sensitive to their degree of overlap, thus making the method more robust to under-sampling. In contrast, TI would require an expensive resampling numerical procedure to achieve the same objective.

The Markov Chain Monte Carlo (MCMC) random walk of replica $i \in [0,K]$ will generate samples with unnormalised probability density $q_i(\boldsymbol{x})$, which for a standard Metropolis Monte Carlo walk is

$$q_i(\boldsymbol{x}) \equiv e^{-\beta_i U_i(\boldsymbol{x})} \tag{4.1}$$

with biasing potential $U_i(\boldsymbol{x})$ and inverse temperature β_i; from now on we assume $\beta_i = 1$ for all walkers R_i, without loss of generality. The normalised probability density is then

$$p_i(\boldsymbol{x}) = Z_i^{-1} q_i(\boldsymbol{x}) \tag{4.2}$$

with normalisation constant

$$Z_i = \int_{\mathbb{R}^n} q_i(\boldsymbol{x})\, \mathrm{d}\boldsymbol{x}. \tag{4.3}$$

We require that the bias potential $U_i(\boldsymbol{x})$ can be factorised as

$$U_i(\boldsymbol{x}) = \Theta_\Gamma(\boldsymbol{x}) u_i(\boldsymbol{x}) \tag{4.4}$$

where u_i is the reduced potential function and $\Theta_\Gamma(\boldsymbol{x})$ is the "oracle" [177], such that for all choices of $u_i(\boldsymbol{x})$,

$$U_i(\boldsymbol{x}) = \begin{cases} u_i(\boldsymbol{x}) & \text{if } \boldsymbol{x} \in \Gamma \\ \infty & \text{if } \boldsymbol{x} \notin \Gamma \end{cases} \tag{4.5}$$

We thus have that the normalisation constant in Eq. (4.3) becomes an integral over the manifold Γ

$$Z_i = \int_{\mathbb{R}^n} e^{-U_i(\boldsymbol{x})}\, \mathrm{d}\boldsymbol{x} = \int_{\Gamma} e^{-u_i(\boldsymbol{x})}\, \mathrm{d}\boldsymbol{x}. \tag{4.6}$$

If replica R_M is chosen to have bias $u_M = 0$, by definition Eq. (4.6) becomes the volume V_Γ. Hence if we can compute the partition function for the reduced potential function $u_M = 0$, we can compute the volume V_Γ.

The MBAR method [188] is a binless and statistically optimal estimator to compute the difference in dimensionless free energy for multiple sets of equilibrium states (trajectories) $\{\boldsymbol{x}\}_i$ obtained using different biasing potentials $u_i(\boldsymbol{x})$. The difference in dimensionless free energy is defined as

$$\Delta \hat{f}_{ij} \equiv \hat{f}_j - \hat{f}_i = -\ln\left(\frac{Z_j}{Z_i}\right) \tag{4.7}$$

which can be computed by solving a set of self-consistent equations as described in Ref. [188]. Note that only the differences of the dimensionless free energies are meaningful as the absolute values $\hat{f}_i$ are determined up to an additive constant and that the "hat" indicates MBAR estimates for the dimensionless free energies, to be distinguished from the exact (reference) values.

Let us define the volume $V_\gamma = \pi^{n/2} r_\gamma^n / \Gamma(n/2+1)$ of a n-ball $\gamma \subseteq \Gamma$ with radius r_γ centred on $\boldsymbol{x}_0$ and absolute dimensionless free energy $f_\gamma = -\ln V_\gamma$. For instance, when the volume of a basin of attraction in a potential energy landscape is to be measured, $\boldsymbol{x}_0$ is chosen to be the minimum energy configuration and $\gamma \subseteq \Gamma$ the largest n-ball centred at $\boldsymbol{x}_0$ that fits in Γ. We also define $\{\boldsymbol{x}\}_i$ to be the set of states sampled with biasing potential u_i and $\{\boldsymbol{x}\}_\gamma = \cup_{i=0}^{K}\{\boldsymbol{x} : |\boldsymbol{x}-\boldsymbol{x}_0| \leq r_\gamma\}_i$ to be the set of states re-sampled within γ with reduced potential

$$u_\gamma(\boldsymbol{x}) = \begin{cases} 0 & \text{if } |\boldsymbol{x}-\boldsymbol{x}_0| \leq r_\gamma \\ \infty & \text{if } |\boldsymbol{x}-\boldsymbol{x}_0| > r_\gamma \end{cases} \tag{4.8}$$

In other words we augment the set of states with the additional reduced potential u_γ. Note that MBAR can compute free energy differences and uncertainties between sets of states not sampled, *viz.* with a different reduced potential function, without any additional iterative solution of the self-consistent estimating equations, see Ref. [188] for details.

Computing the free energy difference between the sets of equilibrium states $\{\boldsymbol{x}\}_\gamma$ and $\{\boldsymbol{x}\}_M$, chosen to have reduced potentials $u_M = 0$ and u_γ, we find that the absolute free energy for the unbiased set of states $\{\boldsymbol{x}\}_M$ is

$$f_M = f_\gamma + (\hat{f}_M - \hat{f}_\gamma) \tag{4.9}$$

where the free energy difference $\hat{f}_M - \hat{f}_\gamma$ is obtained by MBAR with associated uncertainty $\delta\Delta\hat{f}_{M\gamma}$. The volume of the manifold is then just $V_\Gamma = \exp(-f_M)$ with uncertainty $\delta V_\Gamma = V_\Gamma \delta\Delta\hat{f}_{M\gamma}$. Note that the set of biasing potentials u_i must be chosen so that there is sufficient overlap between each neighbouring pair of $p_i(\boldsymbol{x})$. For instance for the harmonic bias $u_i = k_i|\boldsymbol{x}-\boldsymbol{x}_0|^2/2$ we must choose a set of coupling constants k_i so that all neighbouring replicas have a sufficient probability density overlap.

4.2.2 Computational procedure

We choose a set of harmonic bias potential functions

$$u_i = \frac{1}{2}k_i|\boldsymbol{x}-\boldsymbol{x}_0|^2 \tag{4.10}$$

with $k_{i\in[1,M]} = \{k_1,\dots,k_{M-1},0\}$ and perform 10^{10} Hamiltonian Parallel Tempering steps as described in Sec.2.4 [1]. Note that each Monte Carlo step is followed by a full energy minimisation to test whether the walker has stepped outside the basin of attraction. We choose half of the k's to be positive and the other half negative to accelerate equilibration as well as to increase the DOS resolution near the boundary of the basin. The distributions obtained from the replicas with negative coupling constants contribute to the final MBAR volume

---

[1] Note that for convenience we used the same choice of positive k's as required for thermodynamic integration as described in Sec. 2.4 . For this particular method any choice of k's is appropriate, typically a geometric distribution, denser for small k and coarser near k_1 is also suitable.

estimation, unlike for TI. We stress that the choice of biasing potential is arbitrary. Near the origin we sample the set of configurations $\{\boldsymbol{x}\}_0$ directly from a hypersphere centred at $\boldsymbol{x}_0$ with radius sampled from a Gaussian distribution with standard deviation $\sigma = \sqrt{\langle|\boldsymbol{x}-\boldsymbol{x}_0|^2\rangle_{k_1}}$, corresponding to a coupling constant $k_0 = 1/\sigma^2$. This choice of k_0 is such that there is sufficient overlap between the distributions of $\{\boldsymbol{x}\}_0$ and $\{\boldsymbol{x}\}_1$, as can be verified looking at the two leftmost curves in Fig. 4.1 [2]. The corresponding bias potential function is

$$u_0 = (n-1)\log|\boldsymbol{x}-\boldsymbol{x}_0| + \frac{1}{2}k_0|\boldsymbol{x}-\boldsymbol{x}_0|^2, \tag{4.11}$$

where the first term on the right-hand-side is the log-DOS for a n-ball, necessary to account for the greater entropy associated with the regions of space further away from the origin. For a system of N particles in d dimensions with fixed centre of mass we have $n=(N-1)d$ degrees of freedom. The overhead associated with this calculation is insignificant compared to the Hamiltonian Parallel Tempering since the samples thus drawn are completely uncorrelated.

We compute the reduced free energy differences between each of $1+31$ replicas with reduced potential functions given by Eqs. (4.10)–(4.11) using PyMBAR [188, 190]. As reference volume we choose γ to be the n-ball of radius r_γ centred on $\boldsymbol{x}_0$ with approximately $\mathcal{R}=0.9$ of its volume contained within the basin Γ. We choose $\gamma \not\subseteq \Gamma$ to allow more samples with $|\boldsymbol{x}-\boldsymbol{x}_0| \leq r_\gamma$ thus reducing the uncertainty in the MBAR estimate. For $\mathcal{R}\approx 1$ we can correct exactly for this by noting that

$$\mathcal{R} = \frac{1}{V_\gamma}\int_\gamma p_0(\boldsymbol{x})d\boldsymbol{x} \tag{4.12}$$

and $\mathcal{R}$ can be computed directly by Monte Carlo. We thus rewrite Eq. (4.9) as

$$f_M = f_\gamma + (\hat{f}_M - \hat{f}_\gamma) - \log\mathcal{R}. \tag{4.13}$$

Note that the difference in reduced free energies computed using a reference sphere of radius $r_\gamma/2$ or $2r_\gamma$ is within the statistical uncertainty, hence the method is robust with respect to the choice of reference sphere. We also note that this method ought not be limited to the n-ball as the choice of reference volume, in fact any geometrical body $\gamma \subseteq \Gamma$ of known volume and surface (thus for which a similar expression to Eq. (4.11) can be derived) is suitable, for instance a hypercube or a hyperellipsoid. If $\gamma \not\subseteq \Gamma$ then an accurate estimate of $\mathcal{R}$ must be available.

---

[2] To do so we sample a direction from the surface of the unit sphere and the length of the displacement from a Normal$(0,\sigma)$.

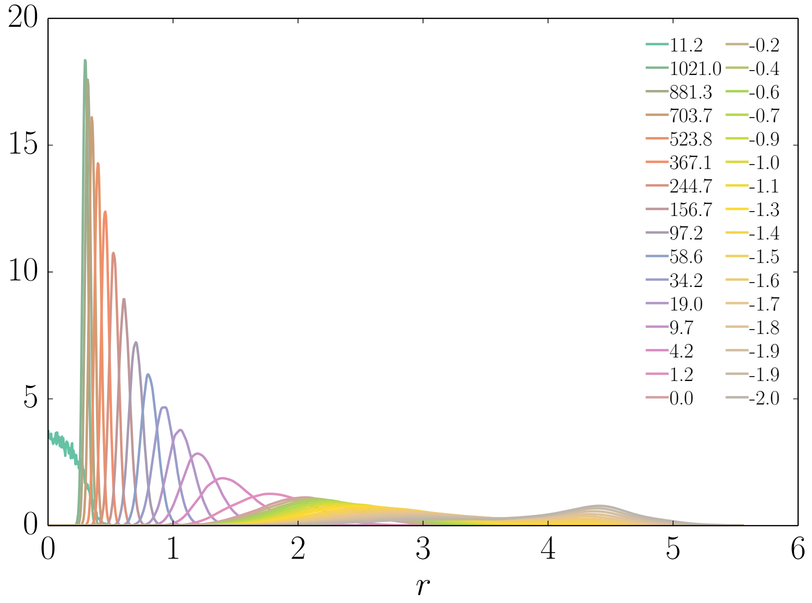

Fig. 4.1 Kernel density estimation of the distance sampled by a random walk within the basin, coupled to the minimum with decreasing harmonic coupling constant k from left to right. The left-most curve was obtained by direct sampling as described in the text. Replicas with $k < 0$ explore regions of the volume that would otherwise never be visited. This particular example is of a disordered packing with polidispersity $\eta = 0.037$.

4.2.3 Density of states

From the analysis of the posterior probability density functions, the present method may yield structural information, as an easy to compute by-product. Choosing a set of biasing potentials $u_i(r)$ that are a function of the distance from the origin $r = |\boldsymbol{x} - \boldsymbol{x}_0|$, we can compute the overall density of states (DOS) for the manifold as a function of r. From each of the $K+1$ replicas' trajectories $\{\boldsymbol{x}\}_i$ we obtain a (binless) kernel density estimation (KDE) [181] of the probability density functions $h_i(r)$, see Fig. 4.1 for an example, which must be unbiased and summed over all replicas to obtain the overall log-DOS function as

$$\log h(r) = \sum_{i=0}^{K} w_i(r) \left(\log h_i(r) + u_i(r) - \Delta \hat{f}_{0i} \right). \tag{4.14}$$

where $w_i(r) = h_i(r) / \sum_{i=0}^{K} h_i(r)$ are normalised weights and $\Delta \hat{f}_{0i}$ are the free energy differences between replicas R_i and R_0.

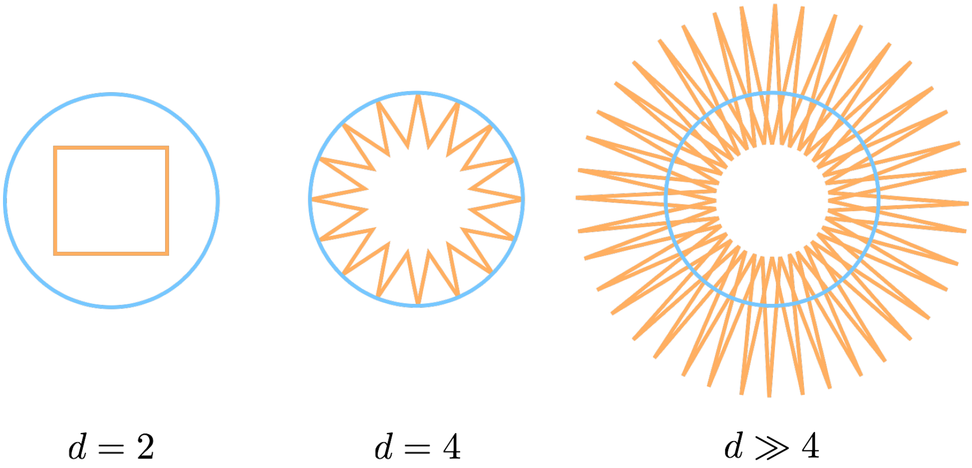

Fig. 4.2 Conceptual illustration of the relationship between the d-ball and the d-cube in 2, 4, and d-dimensions. Consider a d-cube of unit side length and a d-ball with unit radius sharing their centre. As d increases the diameter of the d-ball remains the same, while the diagonal of the unit d-cube grows as $\sqrt{d}$ and the number of corners grows as 2^d: for $d = 2$ the unit square centred at the origin lies completely inside the unit-radius circle. At $d = 4$ the half-diagonal of the 4-cube has unit-length and thus the vertices lie on the surface of the 4-ball. For $d \gg 4$ the vertices of the cube lie far outside the unit ball. On the other hand, each face of the unit d-cube is only distance $1/2$ from the origin and therefore inside the d-ball. In high dimensions all of the volume of the cube will be concentrated in the corners outside the unit ball. Also note that while the volume of the d-cube is 1 for all d, the volume of the unit d-ball shrinks to zero as $d \to \infty$ (curiously going through a maximum in 5 dimensions).

4.3 Basins of attraction in high dimensions

A basin of attraction is defined as the set of all points that lead to a particular minimum energy configuration by a path of steepest descent on a potential energy surface (PES), see Appendix A. Exploring a basin of attraction is computationally expensive because each call to the oracle function $\Theta_\Gamma(\boldsymbol{x})$ requires a full energy minimisation and equilibrating a MCMC on a high dimensional support is difficult [32, 34, 35, 169]. For this reason little is known about the geometry of these bodies [35, 85, 169, 191].

On the basis of ‘brute-force’ calculations on low-dimensional systems, Ashwin et al. [124] suggested that the basins of attraction of energy minima tend to be “branched and threadlike”, quite unlike the hyper-ellipsoidal shape that naively one might expect on the basis of our experience with two or three-dimensional energy landscapes. However, the approach of Ref. [124] breaks down for higher dimensional systems for which most of the volume of the basin is concentrated at distances from the minimum where the overwhelming majority of points do not belong to the basin. The method that we present here allows us to explore precisely those very rarified regions where most of the 'mass' of a basin is concentrated.

In general the representation of *all* high dimensional *convex* bodies should have a hyperbolic form such as the one proposed in the illustration by Ashwin et al. due to the exponential decay in volume of parallel hypersections (slices) away from the median (or equator) [192]. This holds true even for the simplest convex bodies, such as the hypercube, and the underlying geometry need not be "complicated", let alone dendritic, as one would guess at first from the two-dimensional representation, see Fig. 4.2 for an illustration. For the simplest cases of the unit d-sphere and the unit d-cube it can be shown that most of the volume is contained within $\mathcal{O}(1/d)$ of the boundary and that at the same time the volume is contained in a slab $\mathcal{O}(1/\sqrt{d})$ and $\mathcal{O}(1)$ from the equator, irrespective of the choice of north pole, respectively [176, 193]. Hence, there is virtually no interior volume. Such phenomena of concentration of measure are ubiquitous in high dimensional geometry and are closely related to the law of large numbers [193].

As we will show, the results presented by Ashwin et al. are, within the resolution available to their method, qualitatively consistent with those for a simple (unit) hypercube.

4.4 Packing preparation protocol

We draw $N = 32$ particle radii $\{r_{\mathrm{HS}}\}_N$ from a Gaussian distribution $\mathrm{Normal}(1, \eta) > 0$, truncated at $r_{\mathrm{HS}} = 0$, set the box size to meet the target packing fraction of the hard sphere fluid ϕ_{HS} and arrange the particles either in a fcc or a disordered configuration, as described below. Given these hard sphere configurations, we switch on a soft repulsive interaction to generate over-compressed jammed packings, as described in Sec. 2.3.2.

We systematically introduce structural disorder by preparing packings with (geometrically) increasing particle size polydispersity η. For each η we prepare $\sim$10 packings at a soft packing fraction $\phi_{\mathrm{SS}} = 0.74148$ with a soft to hard-sphere radius ratio of $r_{\mathrm{SS}}/r_{\mathrm{HS}} = 1.12$. The particles are placed initially in a fcc arrangement $\boldsymbol{x}_{\mathrm{fcc}}$ and then relaxed via an energy minimisation to a mechanically stable state $\boldsymbol{x}_0$. Energy minimisations are performed with the CG_DESCENT algorithm [141–143]. Thus, for the lowest polydispersities the packings remain in a perfect fcc structure and with increasing η they progressively move away into a disordered glassy state. For the largest polydispersity, for which hard-core overlaps do not allow an initial fcc arrangement, we sample a series of completely random initial states followed by an energy minimisation. Note that even for $\eta \approx 0$, due to the high packing fraction, starting from a completely random set of coordinates, an energy minimisation does not lead to the fcc crystal but rather to the closest glassy jammed state (inherent structure). We are interested in the effect of structural disorder on the shape of the basin of attraction for the soft sphere packings.

4.5 Results: Effect of structural disorder on the basins of attraction of jammed sphere packings

We determine the amount of structural disorder in the packing by computing the Q_6 bond orientational order parameter [171] and the average number of contacts per particle z, shown in Fig. 4.3. As the polydispersity of the system is increased, the coordination number z decays monotonically from the close-packed value of 12 to a value $z_{\mathrm{fcc}} > z > z_{\mathrm{iso}}$, where $z_{\mathrm{iso}} = 6 - 6/32 \approx 5.81$ is the average contact number at iso-staticity for a three-dimensional packing of frictionless spheres [164]. The Q_6 order parameter, computed using a solid-angle based nearest-neighbor definition [194], decays from its fcc value well after the contact number has dropped below the close-packed value of 12.

We start characterising the shape of the high dimensional basins of attraction associated with these packings by performing an unconstrained random walk within the basin and performing principal component analysis (PCA) on the trajectory thus obtained [181]. PCA yields a set of eigenvectors that span the d-dimensional configurational space with associated eigenvalues $\lambda_1, \ldots, \lambda_d$. If the basin possess d-dimensional spherical symmetry then all the eigenvalues are expected to be equal. A measure of the shape of a random walk is then the asphericity factor [195]

$$A_d = \frac{\sum_{i>j} (\lambda_i - \lambda_j)^2}{(d-1)\left(\sum_{i=1}^{d} \lambda_i\right)^2}, \tag{4.15}$$

that has a value of 0 for a spherically symmetric random walk and of 1 for a walk that extends only in one dimension. Note that for an unrestricted random walk one finds $A_d = 2(d+2)/(5d+4)$ for linear chains [195] and therefore, contrary to intuition, the trails of unrestricted random walks are elongated rather than spherical. However, in this work, we consider restricted random walks designed to sample uniformly, hence in a spherical volume we verify that $A_d \approx 0$. Furthermore, we compute the distance of the centre of mass (CM) position from the minimum energy configuration for the random walk, $|\langle \boldsymbol{x} \rangle - \boldsymbol{x}_0|$. This quantity reveals whether the basin is isotropic around the minimum or not. Both quantities, averaged over all packings, are plotted as a function of polydispersity in Fig. 4.3 along with the structural order parameters. Interestingly, we observe that for low η the basins are, on average, spherically symmetric and isotropic around the minimum. With the onset of

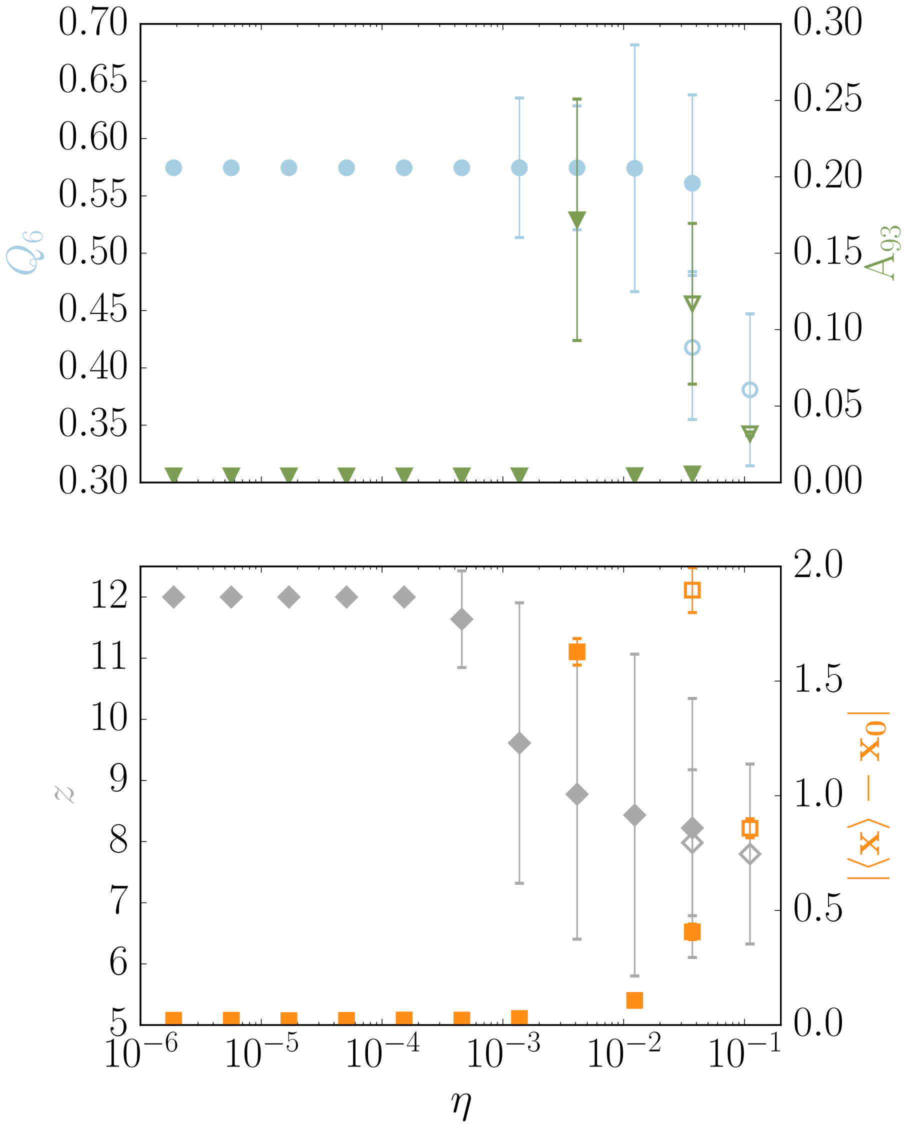

Fig. 4.3 Structural disorder as a function of polydispersity η is quantified by the average coordination number z (grey diamonds) and the Q_6 bond orientational order parameter (blue circles); error bars correspond to one standard deviation of the distribution of values per particle. Basin shape is characterized by the asphericity factor A_d (green triangles) and the mean distance of the centre of mass from the minmum (orange squares); error bars correspond to the standard error. Filled and empty markers correspond to packings obtained starting from an fcc and a disordered arragement, respectively.

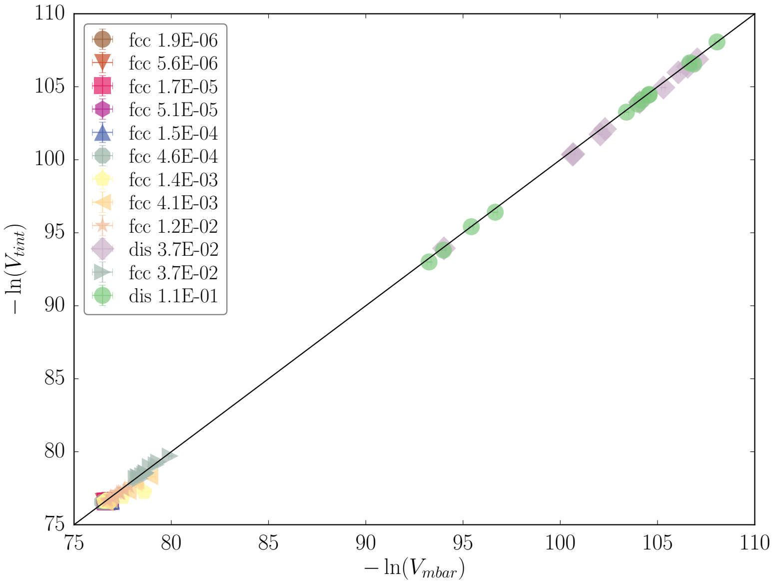

Fig. 4.4 Comparison of the volumes computed by thermodynamic integration, using only the replicas with positive coupling constant, and by MBAR following the protocol described in this work.

structural disorder we observe a marginal increase in asphericity and in the *CM* distance from the minimum. In order to observe a significant change however, we need to go to the fully disordered packings at higher polydispersity. With increasing polydispersity, we observe significant changes in the structural order parameters and in the asphericity factor A_d and *CM* distance from the minimum.

Using the procedure described in Sec 4.2.2 to compute the volume of the basins of attraction, we find excellent agreement with thermodynamic integration, see Fig. 4.4. We find that structural disorder has a dramatic effect on the volume of basins of attraction: from Fig. 4.4 we see that monodispere and polydisperse fcc packings differ in size by a factor of 10 to 100, consistent with the reduced stability of the fcc structure when polidispersity is increased. For polydisperse packings, on the other hand, ordered and disordered packings differ in volume by 10 to 15 orders of magnitude, see for instance $\eta = 0.037$. Such a dramatic difference highlights the role of the protocol: starting from a random quench we obtain jammed packings with basins that are much smaller than for fcc, but orders of magnitude more numerous.

As a natural by-product of the computation we are able to compute the radial probability density function (DOS), shown in Fig. 4.5 together with the logarithm of the ratio between the measured DOS, and that of a d-hypersphere. The log-ratio curves clearly show that all basins have a well-defined hyperspherical core region, where the curves are flat around 0, followed by a series of exponential decays at larger distances from the minimum. For $\eta < 10^{-4}$ the curves are mostly indistinguishable from one another with most of the probability mass concentrated between $1 < r < 3$, as it can be seen from the inset showing the corresponding cumulative distribution function (CDF). For higher polydispersity, the DOS curves have ever longer tails, as it is also shown by the systematic shift in the CDF.

Importantly, the curves show that a 'rejection' method to measure the basin volume will fail. In this method, the volume of the basin is determined by integrating the fraction of points on a hyper-shell with radius r that fall inside the basin. That fraction is the function shown in the bottom panel of Fig. 4.5. The most important contribution to the integral would come from the range of r values where $h(r)$ (top panel of Fig. 4.5) has a significant value. As can be seen from the figure, for disordered systems this happens for values of r where the fraction of hyper-sphere points within the basin is extremely small, in the example shown $\mathcal{O}(10^{-30})$. Hence, the dominant part of the integral would come from parts that are never sampled.

To interpret our results for the DOS curves, it is useful to compare with the corresponding result for a unit hypercube (see Fig. 4.5). In one instance we do so by placing the 'origin' of the hypercube at its *CM*, and in another by placing the origin on one of the 2^d corners of the hypercube, to generate a DOS of a system with a very anisometric density distribution. An illustration of the d-cube geometry is given in Fig. 4.2. When the 'origin' of the hypercube is at its *CM* ('iso-cube' in Fig. 4.5), we observe a larger hyperspherical core region followed by a rapid single-rate decay in $h(r)$, consistently with the numerous number of corners (2^d) of the d-cube. The observed $h(r)$ for the 'iso-cube' is therefore qualitatively similar to that obtained for ordered fcc packings with small η, in that they are both simply concave down, although when η becomes large a point of inflection followed by a longer tail appears. When the 'origin' is placed on one of the corners of the hypercube ('hcube' in Fig. 4.5), we observe a smaller hyperspherical core region followed by a rapid decay with different rates over different distances: the function is first concave down and then around $r \approx 2$ there is a first point of inflection. Not surprisingly, moving the origin of the system from the center to the corner of a hypercube has a dramatic effect on the shape of the DOS, which is now much more similar to the curves for large η, with similar characteristic changes of slope observed for the basins. Again, this agrees with the observation that the *CM* distance increases with increasing structural disorder. The effect of the basin asphericity, as measured by the asphericity factor A_d is difficult to infer from the DOS alone.

We thus measure and observe that the structural isotropy and high degree of rotational symmetry in the crystal, as indicated by the Q_6 parameter, is reflected in the isotropy and

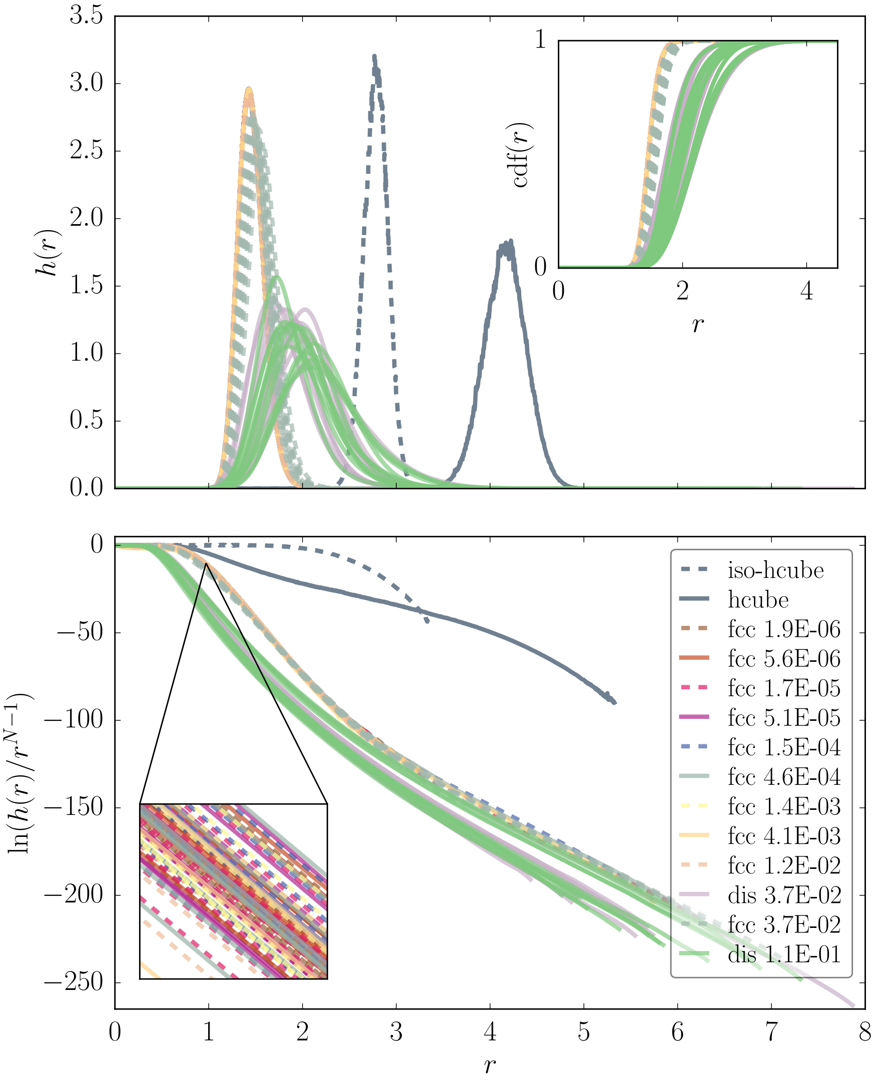

Fig. 4.5 Top plot shows the measured basin radial probability density function $h(r)$ (DOS) for packings at different polydispersities. The solid and dashed blue curves correspond to the DOS of a 93D hypercube, measured from the centre of mass ('iso-cube') and from a point in one of the corners. The top inset shows the cumulative distribution function for $h(r)$. The bottom panel shows the logarithm of the ratio of the DOS of the basin and of a 93D hyperball. The bottom inset shows the set of barely distinguishable overlapping curves measured for low polydispersities. Top and bottom plots share the x-axis.

spherical symmetry of the basin around the minimum, even for relatively large polydispersities when the average contact number has already dropped considerably from the close-packed value. Similarly, the structural disorder at larger η is reflected in the anisotropy and asphericity of the basin. Hence, changes in the basin structure, as indicated by the asphericity factor, the *CM* and the density profile, occur before any observable changes occur in Q_6 and after the average contact number ($z \lesssim 9$) has fallen well below the close-packed value of 12.

4.6 Conclusions

An efficient method for the computation and characterisation of high-dimensional volumes based on the multi-state Bennet acceptance-ratio method has been presented. The technique is simpler and more versatile than the existing, and state-of-the-art, Einstein crystal method [146] discussed in Appendix B, as well as free of any additional systematic biases, introduced for instance by the numerical integration step in ECM. Numerical results for the MBAR-based method are found to be in excellent agreements with ECM.

As well as being binless and statistically optimal, the method yields a direct estimate of the statistical errors and, as natural by-product, the histogram method allows us to obtain an estimate of the radial probability density profile interior to the basin. Numerical results for jammed packings of three-dimensional soft spheres show that brute-force ’rejection’ methods, such as the one proposed in Ref. [124], are unsuited to compute the volume of basins of attraction in high dimensions. Our analysis suggests that the basin of attraction of disordered polydisperse soft sphere packings have an extremely small spherical core region, are overall oblate, as shown by PCA, have numerous corners, as shown by comparison with a hypercube, and their centre of mass is shifted with respect to the minimum energy configuration. The basin of attraction of order soft sphere packings with low polydispersity, on the other hand, are isotropic around the centre of mass, that also coincides with the minimum energy configuration. At the density we study, we also show that order packings have larger basin volumes.

Finally, despite not having explored this direction, the method can be easily generalised to the computation of the free energy of solids, analogously to the Einstein-crystal method, see Appendix B.

Chapter 5

Density propagation method for surveying the energy landscape geometry

The enumeration of the minima in an arbitrary potential energy landscape can be accomplished by measuring the volumes of ‘basins of attraction’ associated with a subset of those minima, in what is known as the mean basin volume method. Key applications of this method include the direct computation of the entropy of complex physical systems, or the a priori assessment of the performance quality of complex objective functions used e.g. in the context of machine learning. Here a novel technique for calculating basin volumes is presented, addressing several shortcomings of the established approach. We develop a practical implementation of this technique and validate it through application to systems with known volumes. The new method is found to be scalable, with simulations revealing a linear relationship between system dimensionality and the computational cost of measuring the basin volume. In a proof-of-principle demonstration, the technique is used to measure the volumes of all three basins of attraction of the one-dimensional XY model with eight spins. The basin of the global energy minimum is found to occupy $(79.31 \pm 0.17)\%$ of the total system volume, with the remaining two minima accounting for $(10.35 \pm 0.08)\%$ each. Finally, we show how this method is able to assist in the visualisation of complex, high-dimensional basin structures.

— This chapter is based on Ref. [196]: Shang-Wei Ye, Stefano Martiniani, K. Julian Schrenk, Jacob D. Stevenson, Daan Frenkel, and Eric Vanden-Eijnden, *submitted*

5.1 Introduction

The emergent behaviour of complex systems can often be better understood in light of their entropy, which is determined by the number of accessible microstates [151, 197]. For all but the simplest systems, the number of these states is so large that its calculation poses a formidable challenge even for the most sophisticated analytical or numerical approaches presently available. As such, the development of efficient and robust methods for enumerating the microstates of a given system and the analysis of their properties is of great general interest. The development of this class of methods is crucial for understanding the dynamical and thermodynamical properties of numerous systems in physics, chemistry, or biology, whose evolution can be modeled as a navigation over a high-dimensional energy landscape with an exponential number of stationary points [125]. In this context, key questions include determining the number and level of stationary points, the volume of the basins of attraction associated with energy minima, and the height of the energy barriers that need to be overcome to escape these basins [25, 28, 32, 34–36]. Similar questions have also emerged in computer science and machine learning, in particular in the context of the training of deep neural networks [43, 45, 47]. This problem involves the optimization of a complex objective function whose geometric properties ultimately determine the feasibility of the learning algorithm and the performances of the network it leads to.

A promising method for calculating the number of stable points in an energy landscape has been developed within the context of granular packings, where the enumeration of the possible microstates allows for a direct computation of the configurational (granular) entropy. The method in question is the so called ‘mean basin volume’ (MBV) method [32, 34, 35], outlined in Sec. 2.2. The basis of this method is the computation of the volumes of the ‘basins of attraction’ [198] of the mechanically stable packings. Conventionally, this is achieved by thermodynamic integration from a harmonic reference state [33, 151], see Sec. 2.4, or from a region of known volume [36], see Sec. 4.2. This is not without limitations. These methods rely on a Markov Chain Monte Carlo that at each step generates a full energy minimisation path to check whether the step falls within the basin; all minimisation paths are then discarded. Given that generating paths is the most time-consuming part of the method, it would be advantageous if more useful data could be extracted from them. Here we design and evaluate a new approach to the calculation of basin volumes, termed the ‘density propagation method’, which makes use of novel mathematical results and provides quantitative insights into the geometry of basins of attraction.

5.2 Density propagation method

5.2.1 Mathematical basis

Consider a D-dimensional system with its potential energy at a configurational coordinate $\boldsymbol{x}$ given by $U(\boldsymbol{x})$. A basin of attraction can be associated with a local minimum of $U(\boldsymbol{x})$ at $\boldsymbol{x}_i$. This is defined as the set Γ of all points $\boldsymbol{x}$ which belong to the steepest-descent trajectories reaching $\boldsymbol{x}_i$. The volume of this basin is V_Γ. A particular trajectory can be characterized by the vector field $\boldsymbol{X}(t,\boldsymbol{x})$, which is parametrized by a 'time' t such that

$$\frac{\mathrm{d}}{\mathrm{d}t}\boldsymbol{X}(t,\boldsymbol{x}) = -\boldsymbol{\nabla} U[\boldsymbol{X}(t,\boldsymbol{x})], \quad \boldsymbol{X}(0,\boldsymbol{x}) = \boldsymbol{x}. \tag{5.1}$$

Note that $\boldsymbol{X}(t,\boldsymbol{x}) \to \boldsymbol{x}_i$ as $t \to \infty$. Furthermore, following a trajectory backwards in time gives steepest-*ascent*, so that $\boldsymbol{X}(t,\boldsymbol{x})$ approaches the basin boundary as $t \to -\infty$. The uniqueness theorem guarantees that trajectories do not intersect each other at finite t.

We now introduce a reference region $\gamma \subset \Gamma$ of volume V_γ, that contains the minimum $\boldsymbol{x}_i$. Any trajectory starting inside the basin but outside the reference, *i.e.* at $\boldsymbol{x} \in \Gamma \setminus \gamma$ (where $\setminus$ denotes the set-theoretic difference), will hit the surface $\partial\gamma$ of the reference region at some finite, positive $t = \tau_+(\boldsymbol{x})$, at a coordinate $\boldsymbol{X}(\tau_+(\boldsymbol{x}),\boldsymbol{x}) \in \partial\gamma$.

Suppose there is some material filling $\Gamma \setminus \gamma$ with uniform density at $t = 0$, which flows according to $\boldsymbol{X}(t,\boldsymbol{x})$. Since the total amount of material in Γ is conserved, its density $\rho(\boldsymbol{x},t)$ must satisfy the continuity equation

$$\frac{\partial \rho(\boldsymbol{x},t)}{\partial t} = \boldsymbol{\nabla} \cdot [\rho(\boldsymbol{x},t)\boldsymbol{\nabla} U(\boldsymbol{x})], \tag{5.2}$$

subject to the initial condition

$$\rho(\boldsymbol{x},0) = \begin{cases} 1/V_{\Gamma\setminus\gamma} & \boldsymbol{x} \in \Gamma \setminus \gamma \\ 0 & \boldsymbol{x} \notin \Gamma \setminus \gamma \end{cases}, \tag{5.3}$$

where $V_{\Gamma\setminus\gamma} \equiv V_\Gamma - V_\gamma$ is the volume of $\Gamma \setminus \gamma$. This describes how the material flows through $\partial\gamma$ and enters the reference region γ to accumulate at $\boldsymbol{x}_i$ as $t \to \infty$. Solving Eq. (5.2) allows us to calculate the fraction $\nu_{\partial\gamma}(\boldsymbol{x})\mathrm{d}\sigma(\boldsymbol{x})$ of material that entered the surface through a given surface element $\mathrm{d}\boldsymbol{\sigma}(\boldsymbol{x}) \equiv \hat{\boldsymbol{n}}(\boldsymbol{x})\mathrm{d}\sigma(\boldsymbol{x})$ at $\boldsymbol{x} \in \partial\gamma$. We find

$$\nu_{\partial\gamma}(\boldsymbol{x}) = \frac{1}{V_{\Gamma\setminus\gamma}} |\hat{\boldsymbol{n}}(\boldsymbol{x}) \cdot \boldsymbol{\nabla} U(\boldsymbol{x})| \int_0^\infty \det[\mathrm{J}(\boldsymbol{x},t)]\mathrm{d}t, \tag{5.4}$$

where $\hat{\boldsymbol{n}}(\boldsymbol{x})$ is the unit normal to $\partial\gamma$ at $\boldsymbol{x} \in \partial\gamma$, and $\mathrm{J}(\boldsymbol{x},t)$ is the Jacobian matrix of a steepest-ascent transformation:

$$\mathrm{J}(\boldsymbol{x},t) \equiv \frac{\partial \boldsymbol{X}(-t,\boldsymbol{x})}{\partial \boldsymbol{x}}. \tag{5.5}$$

A proof of Eq. (5.4) can be found in Appendix G. Combining Eqs. (5.1) and (5.5) gives

$$\frac{\mathrm{d}}{\mathrm{d}t}\mathrm{J}(\boldsymbol{x},t) = \frac{\partial \nabla U[\boldsymbol{X}(-t,\boldsymbol{x})]}{\partial \boldsymbol{x}}. \tag{5.6}$$

Using this in Jacobi's formula [199] gives us an equation for $\det[\mathrm{J}(\boldsymbol{x},t)]$:

$$\begin{aligned} \frac{\mathrm{d}}{\mathrm{d}t}\det[\mathrm{J}(\boldsymbol{x},t)] &= \det[\mathrm{J}(\boldsymbol{x},t)]\mathrm{Tr}\left\{\mathrm{J}^{-1}(\boldsymbol{x},t)\frac{\mathrm{d}}{\mathrm{d}t}\mathrm{J}(\boldsymbol{x},t)\right\} \\ &= \det[\mathrm{J}(\boldsymbol{x},t)]\mathrm{Tr}\left\{\frac{\partial \nabla U[\boldsymbol{X}(-t,\boldsymbol{x})]}{\partial \boldsymbol{X}(-t,\boldsymbol{x})}\right\} \\ &\equiv \det[\mathrm{J}(\boldsymbol{x},t)]\mathrm{Tr}\{\mathrm{H}[\boldsymbol{X}(-t,\boldsymbol{x})]\}, \end{aligned} \tag{5.7}$$

where $\mathrm{H}[\boldsymbol{X}(-t,\boldsymbol{x})]$ is the Hessian matrix of the potential energy U at position $\boldsymbol{X}(-t,\boldsymbol{x})$. This is just a high-dimensional version of the Euler expansion formula from fluid mechanics [200, 201], telling us how the volume of a small parcel of material changes as it travels along a steepest-ascent trajectory.

Returning to Eq. (5.4), we note that $\nu_{\partial\gamma}$ can also be interpreted as the uniform density in $\Gamma\setminus\gamma$ mapped on to $\partial\gamma$ by steepest-descent. In other words, it satisfies

$$\int_{\partial\gamma} f(\boldsymbol{x})\nu_{\partial\gamma}(\boldsymbol{x})\mathrm{d}\sigma(\boldsymbol{x}) = \frac{1}{V_{\Gamma\setminus\gamma}}\int_{\Gamma\setminus\gamma} f[\boldsymbol{X}(\tau_+(\boldsymbol{x}),\boldsymbol{x})]\mathrm{d}\boldsymbol{x}, \tag{5.8}$$

i.e. the expectation of some arbitrary function $f(\boldsymbol{x})$, with $\boldsymbol{x} \in \partial\gamma$ drawn from $\nu_{\partial\gamma}(\boldsymbol{x})$, must equal the expectation of $f[\boldsymbol{X}(\tau_+(\boldsymbol{x}),\boldsymbol{x})]$, with $\boldsymbol{x}$ sampled from a uniform distribution in $\Gamma\setminus\gamma$.

We now have all the equations necessary for deriving the key result. The surface area S_γ of the reference region is

$$S_\gamma = \int_{\partial\gamma}\mathrm{d}\sigma(\boldsymbol{x}) = \int_{\partial\gamma}\frac{\nu_{\partial\gamma}(\boldsymbol{x})}{\nu_{\partial\gamma}(\boldsymbol{x})}\mathrm{d}\sigma(\boldsymbol{x}). \tag{5.9}$$

Using the result of Eq. (5.8) with $f(\boldsymbol{x}) = 1/\nu_{\partial\gamma}(\boldsymbol{x})$, Eq. (5.9) can be rewritten as

$$S_\gamma = \frac{1}{V_{\Gamma\setminus\gamma}}\int_{\Gamma\setminus\gamma}\frac{\mathrm{d}\boldsymbol{x}}{\nu_{\partial\gamma}[\boldsymbol{X}(\tau_+(\boldsymbol{x}),\boldsymbol{x})]}. \tag{5.10}$$

Recognizing $1/V_{\Gamma\setminus\gamma}$ as the uniform density function in $\Gamma\setminus\gamma$, and substituting from Eq. (5.4), we find

$$\begin{aligned} S_\gamma &= \langle \nu_{\partial\gamma}^{-1}[\boldsymbol{X}(\tau_+(\boldsymbol{x}),\boldsymbol{x})]\rangle_{\Gamma\setminus\gamma} \\ &\equiv V_{\Gamma\setminus\gamma}\langle\rho_{\partial\gamma}^{-1}[\boldsymbol{X}(\tau_+(\boldsymbol{x}),\boldsymbol{x}]\rangle_{\Gamma\setminus\gamma}. \end{aligned} \tag{5.11}$$

where $\langle\cdots\rangle_{\Gamma\setminus\gamma}$ denotes the expectation with respect to a uniformly distributed $\boldsymbol{x}\in\Gamma\setminus\gamma$, and

$$\rho_{\partial\gamma}(\boldsymbol{x}_{\partial\gamma}) \equiv |\hat{\boldsymbol{n}}(\boldsymbol{x}_{\partial\gamma})\cdot\boldsymbol{\nabla}U(\boldsymbol{x}_{\partial\gamma})|\int_0^\infty \det[\mathrm{J}(\boldsymbol{x}_{\partial\gamma},t)]\mathrm{d}t, \tag{5.12}$$

with $\boldsymbol{x}_{\partial\gamma}\equiv\boldsymbol{X}(\tau_+(\boldsymbol{x}),\boldsymbol{x})$. Recalling that $V_{\Gamma\setminus\gamma}=V_\Gamma-V_\gamma$, Eq. (5.11) gives the final result:

$$V_\Gamma = V_\gamma + \frac{S_\gamma}{\langle\rho_{\partial\gamma}^{-1}(\boldsymbol{x}_{\partial\gamma})\rangle_{\Gamma\setminus\gamma}}. \tag{5.13}$$

There is a clear physical interpretation of this result for the system of flowing material we have been considering; $\rho_{\partial\gamma}(\boldsymbol{x}_{\partial\gamma})$ can be seen as the time-integrated volumetric flux through a given point on the reference surface. Taking an average of this quantity, weighted appropriately for the material's initial distribution, and multiplying by the surface area S_γ of the reference region should naturally return the initial volume $V_{\Gamma\setminus\gamma}$ of the material. By adding the volume of the reference region to this, we get the volume V_Γ of the entire basin.

5.2.2 Computational procedure

With the derivation of Eq. (5.13), the theoretical elements necessary for understanding the density propagation method have been laid out. Practical questions regarding its implementation are now addressed.

Firstly, we must define a suitable reference region γ. For simplicity, a hypersphere centered on $\boldsymbol{x}_i$ is chosen. Since γ must be enclosed completely by the basin Γ, it is important to choose the radius R_γ of this sphere to be sufficiently small. The most reliable way of ensuring this is to randomly generate many positions uniformly on $\partial\gamma$ and perform steepest-descent minimisation from each one, checking that they all map to $\boldsymbol{x}_i$. However, this is computationally very expensive. Instead, we use a weaker, but also substantially cheaper, test. Note that for a correctly specified γ, $\boldsymbol{\nabla}U(\boldsymbol{x})$ for all $\boldsymbol{x}\in\partial\gamma$ points outwards from $\partial\gamma$. Thus, so long as the proposed reference sphere is not so large as to contain multiple minima, it is sufficient to verify $\boldsymbol{\nabla}U(\boldsymbol{x})\cdot(\boldsymbol{x}-\boldsymbol{x}_i)>0$ for many trial positions $\boldsymbol{x}$. If a negative result is recorded, R_γ is reduced and the test repeated. It is not appropriate to just choose some arbitrary, extremely small R_γ, since this reduces the proportion of V_Γ known analytically, thus increasing the contribution of numerical errors to the final volume estimate.

The Metropolis algorithm is used to sample points from a uniform distribution inside the basin. In this MCMC walk, starting at the minimum $\boldsymbol{x}_i$, the energy E_i of a configuration is given by:

$$E_i(\boldsymbol{x}) = \begin{cases} 0 & \boldsymbol{x} \in \Gamma \\ \infty & \boldsymbol{x} \notin \Gamma \end{cases}, \tag{5.14}$$

i.e, all steps taking the MCMC walk outside the basin are rejected. Two checks are in place to determine whether point $\boldsymbol{x}$ is in Γ:

1. Any $\boldsymbol{x}$ for which $|\boldsymbol{x} - \boldsymbol{x}_i| \leq R_\gamma$ must be in $\gamma \subset \Gamma$, so can be accepted.
2. If $|\boldsymbol{x} - \boldsymbol{x}_i| > R_\gamma$, steepest-descent is performed, *i.e.* we generate $\boldsymbol{X}(t, \boldsymbol{x})$ for $t \geq 0$. Demonstrating the existence of some finite $t = \tau_+(\boldsymbol{x})$ for which $|\boldsymbol{X}(\tau_+(\boldsymbol{x}), \boldsymbol{x}) - \boldsymbol{x}_i| \leq R_\gamma$ is sufficient for concluding $\boldsymbol{x} \in \Gamma \setminus \gamma$. In this case, $\boldsymbol{x}$ is accepted and the coordinate $\boldsymbol{x}_{\partial\gamma} \equiv \boldsymbol{X}(\tau_+(\boldsymbol{x}), \boldsymbol{x})$ is recorded.

From every valid position $\boldsymbol{x}$ of the random walk, a steepest-ascent path is also followed towards the edge of the basin. Combining the ascent and descent paths gives a complete trajectory, connecting the point $\boldsymbol{x}_{\partial\gamma}$ on the reference sphere to the point $\boldsymbol{X}(-\infty, \boldsymbol{x}_{\partial\gamma})$ on the basin boundary, via $\boldsymbol{x}$.

The most important computation in the density propagation method is the characterization of the trajectory passing through an arbitrary $\boldsymbol{x}$. This is done by updating $\boldsymbol{X}(t, \boldsymbol{x})$ according to Eq. (5.1) by Euler integration, as outlined in Algorithm 1. In practice three termination conditions are used in Algorithm 1; satisfying any one of them ends the algorithm:

- **Condition 1**: $|\boldsymbol{X}_n - \boldsymbol{x}_i| < R_\gamma$, indicating entry into the reference sphere.
- **Condition 2**: $|\nabla U(\boldsymbol{X}_n)|$ is below some minimum threshold, suggesting that the path has reached the vicinity of some stationary point other than $\boldsymbol{x}_i$. If this happens during steepest-descent, we conclude that $\boldsymbol{x} \notin \Gamma$; otherwise it means the ascending end of the trajectory has reached a maximum on the basin boundary.
- **Condition 3**: Pertains only to the steepest-ascent stage and triggers if

  $$\nabla U(\boldsymbol{X}_n) \cdot \nabla U(\boldsymbol{X}_{n-1}) < 0, \tag{5.15}$$

  indicating that the basin edge has been overstepped. In this event, $\boldsymbol{X}_n$ is discarded so that the end position of the trajectory is inside the basin at $\boldsymbol{X}_{n-1}$. This is taken as our estimate for $\boldsymbol{X}(-\infty, \boldsymbol{x}_{\partial\gamma})$.

Algorithm 1 Trajectory and propagation of dilation

```
$\boldsymbol{X}_0 \leftarrow \boldsymbol{x}$; $n \leftarrow 0$; $\mathrm{Tr}(\mathrm{H}_0) \leftarrow \mathrm{Tr}[\mathrm{H}(\boldsymbol{X}_0)]$

while termination condition is not satisfied do
    //steepest-descent
    choose integration step $\Delta t_n$;
    $\boldsymbol{X}_{n-1} \leftarrow \boldsymbol{X}_n - \Delta t_n \boldsymbol{\nabla} U(\boldsymbol{X}_n)$;
    $\mathrm{Tr}(\mathrm{H}_{n-1}) \leftarrow \mathrm{Tr}[\mathrm{H}(\boldsymbol{X}_{n-1})]$;
    $n \leftarrow n-1$;
end while

if we can conclude that $\boldsymbol{x} \in \Gamma$ then
    $\boldsymbol{x}_{\partial\gamma} \leftarrow \boldsymbol{X}_n$
    $n \leftarrow 0$
    while termination condition is not satisfied do
        //steepest-ascent
        choose integration step $\Delta t_n$;
        $\boldsymbol{X}_{n+1} \leftarrow \boldsymbol{X}_n + \Delta t_n \boldsymbol{\nabla} U(\boldsymbol{X}_n)$;
        $\mathrm{Tr}(\mathrm{H}_{n+1}) \leftarrow \mathrm{Tr}[\mathrm{H}(\boldsymbol{X}_{n+1})]$;
        $n \leftarrow n+1$;
    end while
end if
```

After steepest-ascent has terminated, we are left with a complete series of positions $\{\boldsymbol{X}_n\}$ giving a discretized approximation to the trajectory. We can now compute $\rho_{\partial\gamma}(\boldsymbol{x}_{\partial\gamma})$ using Eq. (5.12).

Although simple Euler integration could be used to solve Eq. (5.7) for $\det[\mathrm{J}(\boldsymbol{x},t)]$, a more accurate result is obtained if we first consider the analytical solution:

$$\ln\{\det[\mathrm{J}(\boldsymbol{x}_{\partial\gamma},t)]\} = \int_0^t \mathrm{Tr}\{\mathrm{H}[\boldsymbol{X}(-t',\boldsymbol{x}_{\partial\gamma})]\}\mathrm{d}t', \tag{5.16}$$

where we have used the initial condition $\det[\mathrm{J}(\boldsymbol{x}_{\partial\gamma},0)] = 1$, which follows from the definition of $\mathrm{J}(\boldsymbol{x},t)$ in Eq. (5.5). Approximating the r.h.s. of Eq. (5.16) with a Riemann sum, we can use an iterative scheme to estimate $\{\det(\mathrm{J}_n)\}$ corresponding to $\{\boldsymbol{X}_n\}$:

$$\ln[\det(\mathrm{J}_{n+1})] = \ln[\det(\mathrm{J}_n)] + \mathrm{Tr}(\mathrm{H}_n)\Delta t_n. \tag{5.17}$$

Finally, we take

$$\int_0^\infty \det[\mathrm{J}(\boldsymbol{x}_{\partial\gamma},t)]\mathrm{d}t \approx \sum_n \det(\mathrm{J}_n)\Delta t_n, \tag{5.18}$$

and $\rho_{\partial\gamma}(\boldsymbol{x}_{\partial\gamma})$ follows from Eq. (5.12).

The choice for the integration steps $\{\Delta t_n\}$ is a very important practical consideration. Using smaller steps reduces numerical errors, at the expense of computation time. A robust method should set step sizes according to local information on the PEL, such that steps are small in regions of rapid Jacobian evolution (high degree of dilation) and large when little is changing (low degree of dilation). From Eq. (5.17), it is clear that the quantity $\mathrm{Tr}(\mathrm{H}_n)\Delta t_n$ should be small for accurate estimation of $\det[\mathrm{J}(\boldsymbol{x},t)]$. Thus, a good choice for Δt_n is usually:

$$\Delta t_n = \frac{\Theta}{|\mathrm{Tr}(\mathrm{H}_n)|}, \tag{5.19}$$

where Θ is some suitably small constant. This expression for Δt_n should not be used blindly, however. For instance, a step should not be taken if it could lead to the trajectory overstepping the reference sphere entirely. A safeguard against this is to have a maximum step proposal, $\Delta t_n^{\max} = R_\gamma / |\boldsymbol{\nabla} U(\boldsymbol{X}_n)|$, so that two successive trajectory points are never separated by more than the reference sphere radius. This is another reason against choosing an extremely small R_γ. A minimum step proposal $\Delta t_n^{\min}$ is also required to prevent arithmetic underflow in the integration of Eq. (5.1).

We must also be wary of large steps at the ends of the trajectory. If the step transporting the trajectory through the reference sphere is large, we will get a poor estimate of $\boldsymbol{x}_{\partial\gamma}$, and by extension, the quantity $|\hat{\boldsymbol{n}}(\boldsymbol{x}_{\partial\gamma}) \cdot \boldsymbol{\nabla} U(\boldsymbol{x}_{\partial\gamma})|$. At the other end of the trajectory, the decision to invalidate the last step if it satisfies Eq. (5.15) means the trajectory is always terminated inside the basin, at some point at most a distance $\Delta t_n |\boldsymbol{\nabla} U(\boldsymbol{X}_n)|$ from the basin boundary. Since no information is gathered beyond this point, it is problematic if $\Delta t_n |\boldsymbol{\nabla} U(\boldsymbol{X}_n)|$ is large, especially in high-dimensional systems where most of the total basin volume is concentrated very close to the boundary [202]. To minimise these end-effects, a backtracking routine is implemented, allowing the trajectory to terminate closer to the basin boundary, see Algorithm 2. On the other hand, if Δt_n leads to the crossing of the reference sphere surface, we solve for Δt_n in $|\boldsymbol{X}_{n-1} - \boldsymbol{x}_i| = |\boldsymbol{X}_n - \Delta t_n \boldsymbol{\nabla} U(\boldsymbol{X}_n) - \boldsymbol{x}_i| = R_\gamma$.

Algorithm 2 Backtracking

```
$c \leftarrow$ user-defined constant

if $\Delta t_n$ leads to the crossing of the basin edge then
    revert trajectory to state immediately before crossing;
    continue updating position using $\Delta t_n / c$ instead of $\Delta t_n$;
    use the same termination logic as before;
end if
```

Having computed $\rho_{\partial\gamma}(\boldsymbol{x}_{\partial\gamma})$ for every $\boldsymbol{x}$ in the walk, we obtain $\langle\rho_{\partial\gamma}^{-1}(\boldsymbol{x}_{\partial\gamma})\rangle_{\Gamma\setminus\gamma}$ by taking an average of the reciprocals correctly weighted to guarantee detailed balance *i.e.* whenever a move is rejected the contribution from the last position $\boldsymbol{x}$ is double counted. Since V_γ and S_γ are known, we can apply Eq. (5.13) to evaluate V_Γ. Uncertainty in the volume can be estimated using the bootstrap method [166].

5.3 Numerical results

The density propagation method was tested in two phases. In a first phase we used a simple hyperspherical basin to gain insight into the major sources of error in the estimation of volumes. The second phase consisted of applying the technique to more complex test systems, offering some indication of how well the method should be expected to perform in the context of, for instance, jammed packings. In what follows, all systems are scaled so that $R_\gamma = 1$ gives a suitable reference sphere inside each basin.

5.3.1 Sources of error in the volume estimation

There are two main sources of error in the estimation of the volume V_Γ by the density propagation method. One is the sampling error associated with drawing $\boldsymbol{x}$ from $\Gamma \setminus \gamma$, which can be reduced by performing a longer MCMC random walk (assuming that the walk is well equilibrated) and thus spawning more trajectories. The other is the numerical error in computing $\rho_{\partial\gamma}(\boldsymbol{x}_{\partial\gamma})$ for a given trajectory, which depends on the size of the integration steps Δt_n.

As discussed before, Δt_n can be chosen such that its product with $\mathrm{Tr}(\mathrm{H}_n)$ equals some constant Θ, see Eq. (5.19). To study how the choice of Θ affects the numerical error, we considered a spherically-symmetric Gaussian potential centered on the origin, enclosed by a hard hyperspherical boundary sharing the same centre. The spherical symmetry of this basin means that, in the exact limit, all $\boldsymbol{x} \in \Gamma \setminus \gamma$ should have the same $\rho_{\partial\gamma}(\boldsymbol{x}_{\partial\gamma})$. This makes the basin ideal for investigating numerical errors in isolation from sampling error. A graphical representation of the density propagation method in the two-dimensional case is shown in Fig. 5.1a.

Fig. 5.1b shows the dimensional dependence of $\eta \equiv |\hat{V}_\Gamma - V_\Gamma|/V_\Gamma$, the relative error in basin volume estimates, for several different values of Θ. In each case, η is seen to stabilise around some fixed value when the number of dimensions D is large. From these results, it can be deduced that in the absence of sampling error, η becomes proportional to Θ. The constant of proportionality is expected to be basin-dependent; here we find $\eta \approx 1.1\Theta$ for

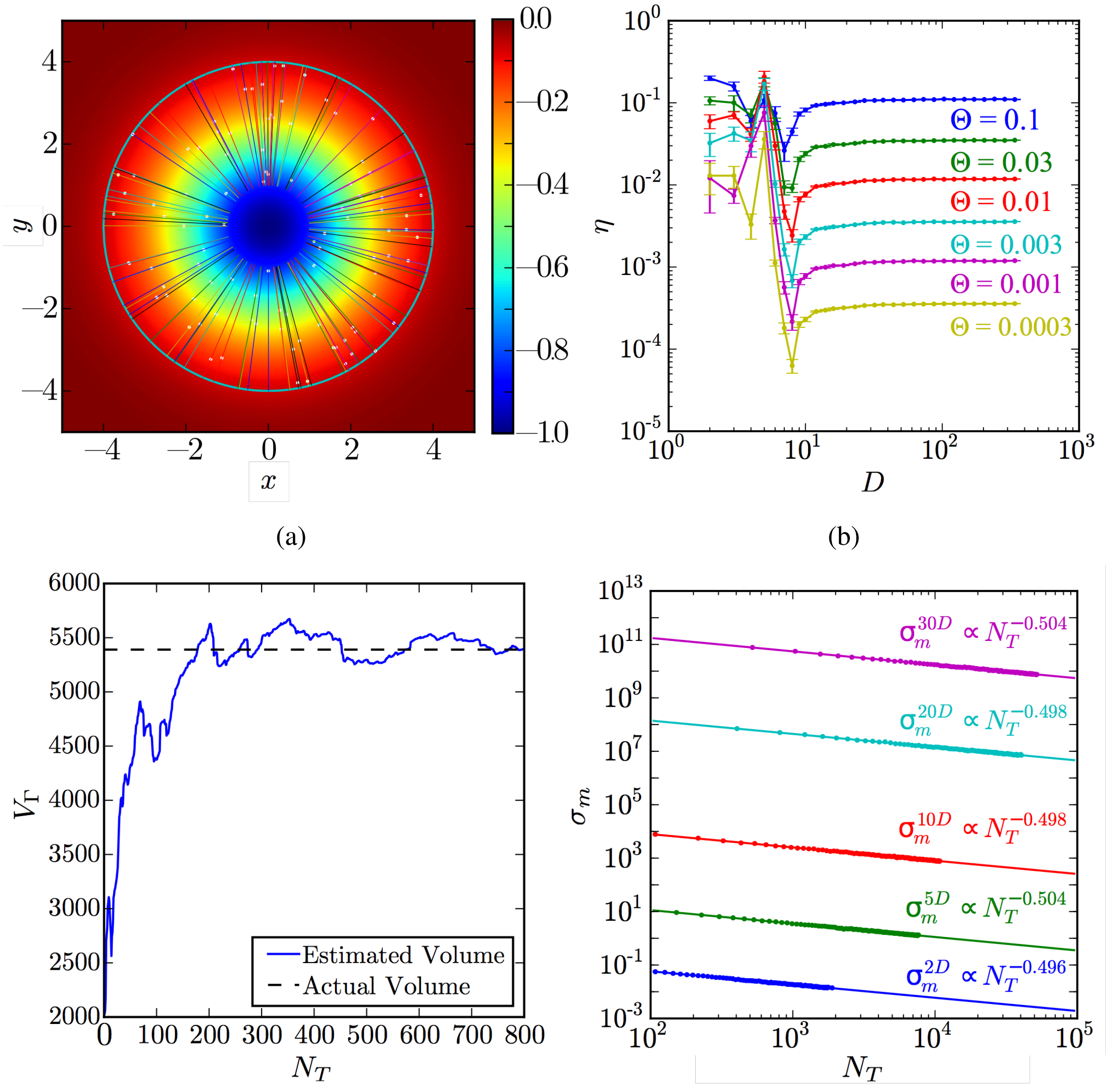

(a) (b)

(c) (d)

Fig. 5.1 (a) Trajectories for a Gaussian potential centered inside a circular box. Positions visited by the MCMC walk are indicated by white dots. (b) Relative error $\eta \equiv |\hat{V}_\Gamma - V_\Gamma|/V_\Gamma$ in the estimated volume of a hyperspherical basin, for $2 \leq D \leq 340$ and several different Θ values, using 10 trajectories per estimate. The error bars refer to the standard errors computed from 10 repeat test runs. (c) Volume estimates as a function of the number of trajectories N_T for a five-dimensional (anisotropic) hyperspherical basin on Gaussian potential offset from the origin. (d) Dependence of sampling error on the number of trajectories N_T, for several numbers of dimensions.

$D > 20$. This simple relationship does not hold for smaller D. A possible explanation for this is that trajectories are more coarsely discretized in low dimensions; since $\mathrm{Tr}(\mathrm{H}_n)$ is typically smaller, larger integration steps are selected via Eq. (5.19), leading to greater numerical errors. This issue is compounded by the fact that in low D, a higher proportion of the basin volume lies near the basin centre than in high D, so poor trajectory characterization near the basin centre adds an additional layer of error. As a result, there is a lack of an obvious relationship between η and D when D is small.

Having established how the selection of Θ affects the numerical error, we then look at how the sampling error in a volume estimate depends on the number of trajectories spawned, N_T. For this we considered an asymmetrical version of the previous basin, with an identical hyperspherical boundary but with the underlying Gaussian potential offset by a unit distance from the origin. Choosing $\Theta = 10^{-3}$ for negligible integration errors, an MCMC walk is performed inside the basin, with the volume estimate revised after the generation of each new trajectory. The walk continues until estimates have stabilized around the true value. Fig. 5.1c shows a time series for these estimates in the five-dimensional case. From the resultant collection of trajectories, the sampling error as a function of N_T can be quantified by bootstrap. This involves drawing many subsamples of size N_T from the original collection of $N'_T \geq N_T$ trajectories. The standard deviation σ_m of subsampled volume estimates is taken to be the sampling error associated with N_T. The above process was repeated for a range of N_T values, in different dimensions, to give the results shown in Fig. 5.1d. The sampling error in the density propagation method appears to decrease as $N_T^{-1/2}$, which is consistent with the use of a Monte Carlo process to generate the distribution of points $\boldsymbol{x}_{\partial\gamma}$.

5.3.2 Application to a mixture of Gaussians

To evaluate the effectiveness of the density propagation method in the context of the mean basin volume approach described in Sec. 2.2, we looked at a mixture of Gaussians potential constructed from the sum of several Gaussian potentials. As before, a hyperspherical boundary was added so that results could be compared against a known system volume V_{system}. The centres of the individual Gaussians were chosen randomly inside the system boundary, subject to a minimum separation constraint between them. Once a 'mixture of Gaussians' potential has been initialized, its minima can be found by local optimisation, using the centres of its constituent Gaussians as starting points. The density propagation method can then be used to estimate the volume $V_\Gamma^{(i)}$ of each basin, and $\sum_i V_\Gamma^{(i)}$ can be compared to the exact system volume V_{system}. The outcome of this process for a two-dimensional trial system constructed by summing 10 Gaussians is illustrated in Fig. 5.2a. With $\Theta = 0.05$ and

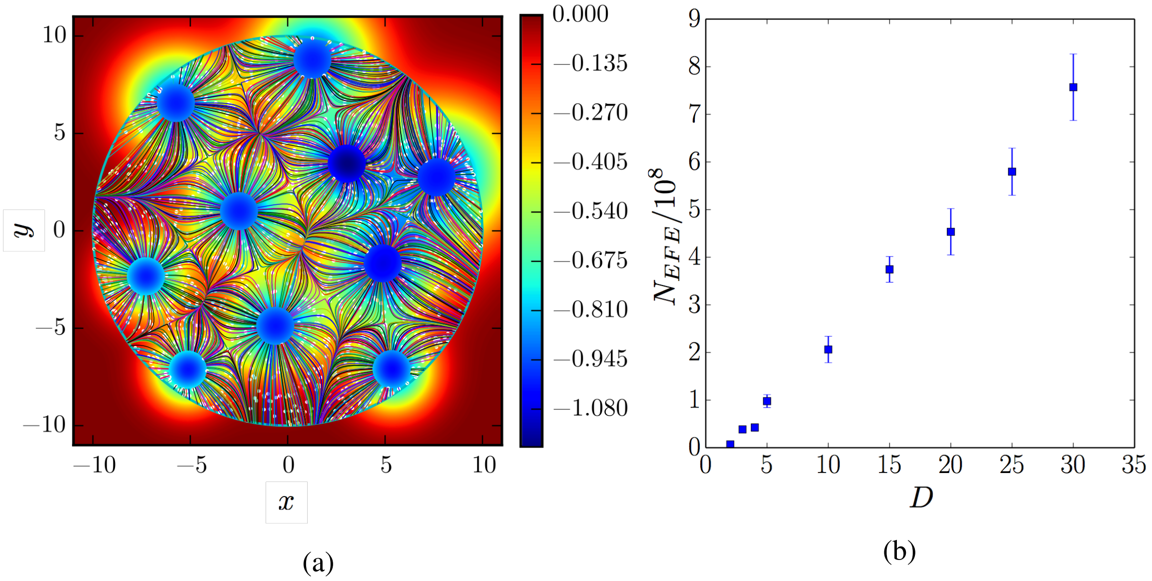

Fig. 5.2 (a) Application of the density propagation method to a two-dimensional potential constructed by summing 10 Gaussians. The spherical boundary (outer circle) defines the system's volume that when estimated with 200 trajectories per basin agrees with the true value to within 0.2%. (b) Number of energy function evaluations N_{EFE} required to achieve a converged estimate of V_{test} for increasing dimensionality. The error bars are computed from 20 samples (basins) for each number of dimensions D.

$N_T = 200$ per basin, the estimated total volume of this particular system was within 0.2% of the true value.

After validating the density propagation method on the two-dimensional trial system, we sought to assess the scalability of the technique to higher-dimensional PELs. In simulations, the costliest function calls are generally those involving $U(\boldsymbol{x})$; in our case, $\nabla U(\boldsymbol{x})$ and $\mathrm{H}(\boldsymbol{x})$, which we re-evaluate after every integration step, see Algorithm 1. Hence, our next test benchmarks how the number of energy function evaluations N_{EFE} needed for a converged volume estimation depends on dimensionality. In this test, we look at mixture of Gaussian potentials consisting of five basins each. We select one basin by minimising from a point sampled uniformly at random in the hyperspherical boundary and compute its volume V_{test} using 10^5 MCMC steps. Convergence is defined to be the largest number of MCMC steps such that the volume estimate deviates more than 1% from the final value. The number of MCMC steps needed until convergence translates to a number of function calls N_{EFE}, see Fig. 5.2b. The evidence from this test indicates that N_{EFE} scales linearly with system dimensionality D.

5.3.3 Application to the XY model

In our final test we consider the well-known XY lattice spin model. In this model, the potential energy of a lattice of N spins oriented at $\theta_1, \cdots, \theta_N$ is given by

$$U_{XY}(\boldsymbol{\theta}) = -\sum_{i \in N} \sum_{j \in n(i)} \cos(\theta_i - \theta_j), \tag{5.20}$$

where $\boldsymbol{\theta} \equiv (\theta_1, \cdots, \theta_N)$ and $n(i)$ is defined to return the nearest-neighbors of the i^{th} spin. In past studies, the stationary points of $U_{XY}(\boldsymbol{\theta})$ have been directly enumerated for two-dimensional lattices of up to $N = 100$ spins [203, 204]. Therefore, this system is a good benchmark for testing the density propagation method and the mean basin volume approach.

As a proof of concept, we considered a one-dimensional chain of $N = 8$ spins, with periodic boundary conditions. As others had done previously [203, 204], we fixed θ_1 at zero to avoid numerical difficulties associated with the global $\mathrm{O}(2)$ symmetry of this system. Since the seven unfixed spins can each have any orientation in $(-\pi, \pi]$, the volume of configuration space for this system is $V_{\text{system}} = (2\pi)^7 \approx 386\,598$. The system has three minima (verified by basin-hopping [205]): a global minimum with all spins aligned, and two local minima with each spin offset by $\pi/4$ from its neighbors. The corresponding configurations are shown in Fig. 5.3a.

The volumes V_Γ^{global} and V_Γ^{local} of the basins corresponding to the global minimum and one of the local minima were computed using an incremental trajectory spawning procedure analogous to that outlined in Sec. 5.3.2. The results are summarized in Table 5.1. Due to the symmetry of the system, both local minima have the same volume, hence $V_{\text{system}} = V_\Gamma^{\text{global}} + 2V_\Gamma^{\text{local}}$. Using the values from Table 5.1, the estimated system volume is $388\,700 \pm 800$. The uncertainty was computed by bootstrap and thus reflects the sampling error, which in this case amounts to 0.2%. The estimated volume in fact differs from the exact value by 0.5%, indicating additional sources of error. These are numerical in origin and could be reduced by using smaller integration steps. From the results, the proportion of phase space occupied by each basin can be deduced. The basin of the global minimum

Minimum	N_{conv}	N_{EFE}	V_Γ
Global	34 800	1.846×10^8	$308\,300 \pm 800$
Local	20 900	1.123×10^8	$40\,220 \pm 70$

Table 5.1 Estimation of V_Γ^{global} and V_Γ^{local}, with $\Theta = 0.001$. The number of trajectories required for convergence is denoted N_{conv}, and the associated number of function evaluations N_{EFE}. The uncertainties in V_Γ correspond to standard errors estimated using 1000 bootstrap samples.

is found to occupy $(79.31 \pm 0.17)\%$ of the total system volume, with each local minimum occupying $(10.35 \pm 0.08)\%$[1].

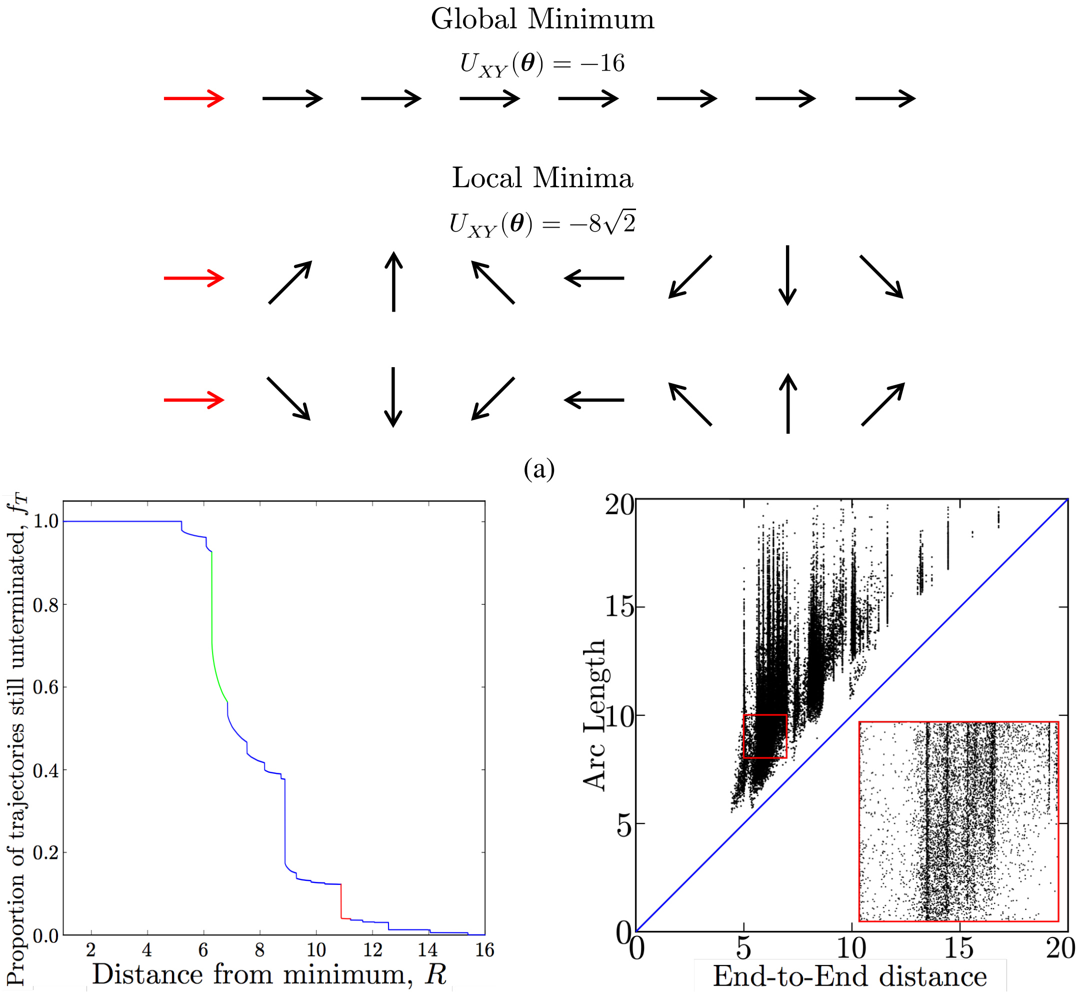

(a)

(b)

(c)

Fig. 5.3 (a) Minimum energy configurations in the $N = 8$ one-dimensional XY model. The fixed spin is highlighted in red. (b) Plot of the proportion of trajectories still unterminated at distance R from the minimum, $f_T(R)$. The characteristic profile of a maximum at the end of a long dendrite is highlighted in red, while a maximum lying away from the extremities of the basin boundary has a typical profile highlighted in green. (c) Scatterplot showing the arc length of each trajectory against its end-to-end distance. The bottom-right image is a zoomed-in version of the highlighted region.

---

[1] These uncertainties have been calculated with the simplifying assumption of a 0.5% numerical error contribution to both V_Γ^{global} and V_Γ^{local} in addition to the bootstrapped standard errors shown in Table 5.1.

5.3.4 Visualizing basins with trajectories

Thus far, the density propagation method has been used solely for calculating basin volumes. In what follows, we demonstrate how the collection of trajectories generated for a given basin in fact reveals information about the basin's geometry. The basin associated with the global minimum in the $N = 8$ one-dimensional XY model (Fig. 5.3a) will be used as an example.

First, by considering the furthest radial distance from the minimum reached by each trajectory, we can calculate the proportion f_T of trajectories with segments lying outside a sphere of radius R centered on the minimum. Fig. 5.3b shows how f_T evolves with increasing R. The value of R for which f_T reaches zero gives the largest length scale of the basin. Moreover, energy maxima can be identified from vertical drops in f_T. A vertical drop followed by an interval of constant f_T suggests a maximum positioned at the end of a long dendrite; all trajectories ending on the maximum are at their greatest distance from the minimum there. A smooth tailing-off in f_T after a vertical drop signifies the opposite; trajectories ending at these maxima may possess segments lying radially further out from the minimum. The total decrease in f_T associated with a particular maximum indicates the height of that maximum. In Fig. 5.3b, the drops in f_T occurring furthest from the minimum are all step-like in profile, implying a dendritic basin structure.

It is also instructive to compare the arc length of each trajectory to its end-to-end distance, as is done in Fig. 5.3c. Points near the blue line correspond to relatively straight trajectories, whilst those at large vertical distances from it represent trajectories taking highly nonlinear routes through space. A series of vertical structures can be identified in the plot, indicating groups of trajectories with different arc lengths but almost the same end-to-end distance. Trajectories belonging to such a group connect a highly localized region of the reference sphere surface to the same maximum, via very different paths. These paths enclose a volume of configuration space which is mapped to essentially a single point on the reference sphere by steepest-descent.

Finally, looking at how the probability density of trajectory arc lengths changes with R (Fig. 5.4a), can alert us to the radial distances at which there are topological features of interest inside the basin. For R just greater than 1, very few trajectories have arc lengths much longer than $R-1$, the shortest distance to $\partial\gamma$. As such, the distribution exhibits high positive skewness, since the mean arc length is effectively equal to $R-1$, as well as low variance. The variance increases from less than 0.1 up to a maximum of 3.8 for $R \in [3.0, 6.3]$. This suggests that the PEL becomes highly anisotropic in this interval, such that the shapes of trajectories traversing different regions of the basin begin to differ greatly. The arc length distributions are bimodal over this range of R (Fig. 5.4b), with the left peak in each instance reflecting those trajectories which have yet to deviate from a linear path. Towards higher R,

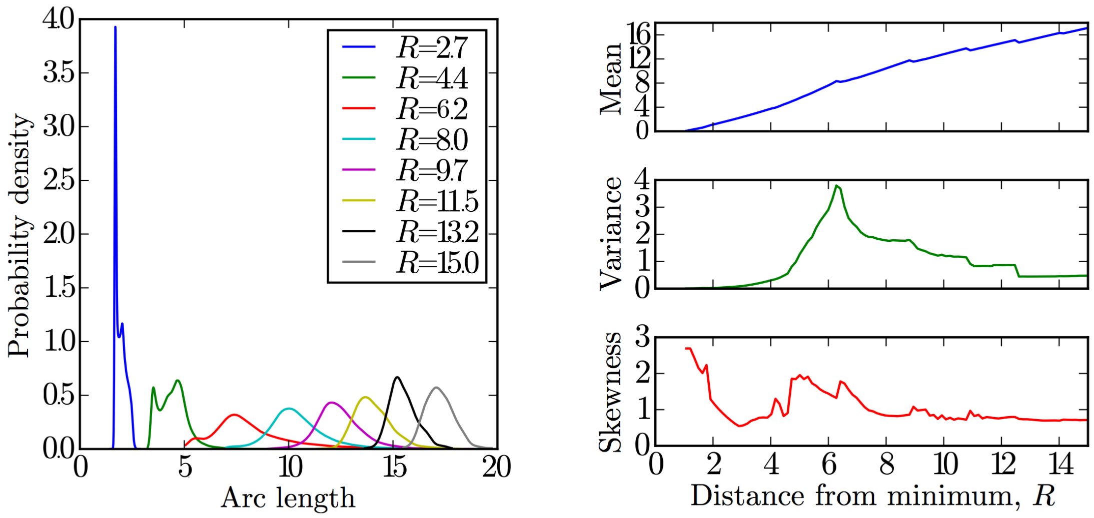

(a) (b)

Fig. 5.4 (a) Trajectory arc length densities for increasing R. Densities were obtained via Gaussian kernel density estimation, using Silverman's rule for bandwidth selection [206]. Note that since $R_\gamma = 1$, the minimum arc length possible at a given R is $R-1$. (b) Evolution of the mean, variance and skewness of the trajectory arc length distribution with increasing R. These quantities were calculated from the kernel density estimates at 100 equidistant intervals between $R = 1$ and $R = 15$.

the trajectory population decreases, leaving only groups of similar trajectories behind. This explains the variance fall-off for $R \gtrsim 6.3$.

5.4 Conclusions

We have developed the density propagation method for surveying energy landscapes and measuring volumes of basins of attraction. This implementation has been applied with success to the basins of several test systems in various dimensions, demonstrating, in principle at least, its compatibility with the MBV method for the calculation of the number of minima in an energy landscape. The new technique has proven to be capable of producing accurate basin volume estimates not only for various toy potentials based on Gaussians in spherical boxes, but also for a simple physical system: the $N = 8$ one-dimensional XY model. In the latter case, we have provided testable predictions for the basin volumes associated with the global and local minima. Furthermore, preliminary simulations involving the method have suggested a linear relationship between computational workload and problem dimensionality.

The density propagation method has been shown to hold several advantages over existing approaches of energy landscape exploration. Notably, in coming to a volume estimate, it makes use of data accumulated during energy minimisation, the most computationally taxing part of most related computational techniques. Moreover, the method deals directly with steepest-descent basins of attraction, which are guaranteed to be compact (note that this requirement can be relaxed the methods discussed in Chapt. 2, 4). Finally, insight into basin geometries can be obtained as a by-product of the density propagation method, making it a valuable tool for visualizing the complex, high-dimensional landscapes being studied.

In its current implementation, the density propagation method has produced encouraging results. However, further development and testing is necessary to establish the practical viability of this method, e.g., when combined with dynamics different from steepest descent. In particular it would be interesting to find dynamics which accelerate convergence while preserving a basin shape true to steepest descent. One possibility in this direction would be to combine the density propagation method with the string method [207, 208], which would permit to calculate the new descent trajectory fast given the old one.

Chapter 6

Monte Carlo sampling for stochastic weight functions

Conventional Monte Carlo simulations are stochastic in the sense that the acceptance of a trial move is decided by comparing a computed acceptance probability with a random number, uniformly distributed between 0 and 1. Here we consider the case that the weight determining the acceptance probability itself is fluctuating. This situation is common in many numerical studies. We show that it is possible to construct a rigorous Monte Carlo algorithm that visits points in state space with a probability proportional to their average weight. The same approach has the potential to transform the methodology of a certain class of high-throughput experiments or the analysis of noisy datasets.

— This chapter is based on Ref. [209]: Daan Frenkel, K. Julian Schrenk, Stefano Martiniani, preprint arXiv:1612.06131

6.1 Introduction

Dynamic Monte Carlo simulations aim to sample the states of the system under study such that the frequency with which a given state is visited is proportional to the weight (often ‘Boltzmann’ weight) of that state. The equilibrium distribution of a system, *i.e.* the distribution for which every state occurs with a probability proportional to its (Boltzmann) weight, is invariant under application of a single Monte Carlo step. Algorithms that satisfy this criterion are said to satisfy ‘balance’ [210]. Usually, we impose a stronger condition: ‘detailed balance’, which implies that the average rate at which the system makes a transition from an arbitrary ‘old’ state (o) to a ‘new’ state (n) is exactly balanced by the average rate for the reverse rate. The detailed balance condition is a very useful tool to construct valid Markov

Chain Monte Carlo (MCMC) algorithms. We can write the detailed balance condition as follows;

$$P(\boldsymbol{x}_o)P_{\text{gen}}(o \to n)P_{\text{acc}}(o \to n) = P(\boldsymbol{x}_n)P_{\text{gen}}(n \to o)P_{\text{acc}}(n \to o) \tag{6.1}$$

where $P(\boldsymbol{x}_i)$ denotes the equilibrium probability that the system is in state i (in this case, i can stand for o or n) characterised by a (usually high-dimensional) coordinate $\boldsymbol{x}_i$). $P_{\text{gen}}(i \to j)$ denotes the probability to generate a trial move from state i to state j. In the simplest case, this may be the probability to generate a random displacement that will move the system from $\boldsymbol{x}_i$ to $\boldsymbol{x}_j$, but in general the probability to generate a trial move may be much more complex (see e.g. Ref. [151]). Finally $P_{\text{acc}}(i \to j)$ denotes the probability that a trial move from state i to state j will be accepted.

Many simple MC algorithms satisfy in addition microscopic reversibility, which means that $P_{\text{gen}}(i \to j) = P_{\text{gen}}(j \to i)$. In that case, detailed balance implies that

$$\frac{P_{\text{acc}}(o \to n)}{P_{\text{acc}}(n \to o)} = \frac{P(\boldsymbol{x}_n)}{P(\boldsymbol{x}_o)} \tag{6.2}$$

There are many acceptance rules that satisfy this criterion. The most familiar one is the so-called Metropolis rule [211]:

$$P_{\text{acc}}(o \to n) = \text{Min}\left\{1, \frac{P(\boldsymbol{x}_n)}{P(\boldsymbol{x}_o)}\right\} \tag{6.3}$$

The acceptance for the reverse move follows by permuting o and n. In the specific case of Boltzmann sampling of configuration space, where the equilibrium distribution is proportional to the Boltzmann factor $P(\boldsymbol{x}_i) \sim \exp(-U_i/k_{\text{B}}T)$, where U_i is the potential energy of the system in the state characterised by the coordinate $\boldsymbol{x}_i$, T is the absolute temperature and k_{B} is the Boltzmann constant. In that case, we obtain the familiar result

$$P_{\text{acc}}(o \to n) = \text{Min}\{1, \exp[-(U_n - U_o)/k_{\text{B}}T]\} \tag{6.4}$$

6.2 Monte Carlo simulations with ‘noisy’ acceptance rules.

There are many situations where conventional MCMC cannot be used because the quantity that determines the weight of a state i is, itself, the average of a fluctuating quantity. Specifically, we consider the case of weight functions fluctuating according to a Bernoulli process, *i.e.* in an intermittent manner, although our approach is not limited to Bernoulli processes. Examples that we consider are ‘committor’ functions, or the outcome of a stochastic minimisation procedure.

Equally interesting are examples where a MCMC algorithm would be employed to steer a (high throughput) experiment where we aim to optimise an output (e.g. crystal nucleation) that is only determined in a probabilistic sense by the initial conditions (typically specified by a large number of parameters). Yet another example would be an experiment that aims to find optimal solutions based on stochastic outcomes (e.g. finding the biologically most functional and/or least harmful composition of a multi-drug cocktail). Problems of this nature – and there are many of them – are, at present not tackled using MCMC sampling. Yet, there is no doubt MCMC sampling is the method of choice to explore high-dimensional parameter space.

Note that the problem that we are discussing here is different from the case considered by Ceperley and Dewing (CD) [212]. CD analysed the problem of performing MCMC sampling of Boltzmann weights in cases where the energy function is noisy. We come back to this point later: suffice it to say that in the case studied in Ref. [212], the crucial point is that the Boltzmann weight is a nonlinear function of the energy and that therefore the Boltzmann factor corresponding to the average energy is not the same as the average of the Boltzmann factor obtained by sampling over energy fluctuations. Ref. [212] showed how to construct an approximate algorithm for such cases, which becomes exact if the fluctuations are normally distributed. Here we consider the case where the probability to sample a point is given rigorously by the average of the stochastic estimator of the weight function.

To give a specific example, we consider the problem of computing the volume of the basin of attraction of a particular energy minimum i in a high-dimensional energy landscape [32, 34–36]. The algorithms discussed in Chapt. 2, 4, 5 rely on the fact that, for every point $\boldsymbol{x}$ in configuration space, we can determine unambiguously whether or not it belongs to the basin of attraction of minimum i: if a (steepest-descent or similar) trajectory that starts at point $\boldsymbol{x}$ ends in minimum i, the ‘oracle function’ $\mathcal{O}_i(\boldsymbol{x}) = 1$, and otherwise it is zero.

However, many minimizers are not deterministic – and hence the oracle function is probabilistic. (In fact, historical evidence suggests that ancient oracles were probabilistic at best). In that case, if we start a number of minimisations at point $\boldsymbol{x}$, some will have $\mathcal{O}_i(\boldsymbol{x}) = 1$ and others have $\mathcal{O}_i(\boldsymbol{x}) = 0$. We denote with $P_{\mathcal{O}}^{(i)}(\boldsymbol{x})$ the average value of the Bernoulli process defined by the oracle function $\mathcal{O}_i(\boldsymbol{x})$. In words: $P_{\mathcal{O}}^{(i)}(\boldsymbol{x})$ is the probability that the oracle function associated with point $\boldsymbol{x}$ has a value of one.

We now redefine the basin volume (probability mass) of minimum i as

$$v_i \equiv \int d\boldsymbol{x}\, P_{\mathcal{O}}^{(i)}(\boldsymbol{x}) \tag{6.5}$$

where $\boldsymbol{x}$ denotes the coordinate in d-dimensional space. Clearly,

$$\sum_{i=1}^{\Omega} v_i = V_{total} \tag{6.6}$$

where Ω is the number of distinct minima. This equation expresses the fact that every trajectory must end up somewhere. Hence, we now have an algorithm that allows us to define basin 'clouds' rather than basin volumes, but for the rest the language stays the same.

6.2.1 Naive MC algorithm

If we consider a large number of trial moves form point $\boldsymbol{x}$ to point $\boldsymbol{x}'$, the average acceptance probability is $P_{\mathcal{O}}(\boldsymbol{x}')$. If we consider a large number of trial moves in the reverse direction, the acceptance probability is $P_{\mathcal{O}}(\boldsymbol{x})$. In steady state, the populations should be such that detailed balance holds. If we denote the 'density' of sampled points by $\rho(\boldsymbol{x})$, then

$$\rho(\boldsymbol{x})P_{\mathrm{acc}}(\boldsymbol{x} \to \boldsymbol{x}') = \rho(\boldsymbol{x}')P_{\mathrm{acc}}(\boldsymbol{x}' \to \boldsymbol{x}) \tag{6.7}$$

Hence if we choose the acceptance probability to be equal to the (instantaneous) value of the oracle function in the trial state, then

$$\rho(\boldsymbol{x})P_{\mathcal{O}}(\boldsymbol{x}') = \rho(\boldsymbol{x}')P_{\mathcal{O}}(\boldsymbol{x}) \tag{6.8}$$

or

$$\frac{\rho(\boldsymbol{x})}{\rho(\boldsymbol{x}')} = \frac{P_{\mathcal{O}}(\boldsymbol{x})}{P_{\mathcal{O}}(\boldsymbol{x}')} \tag{6.9}$$

In words: points are sampled with a probability proportional to the value of the oracle function. Note that in this naive version of the algorithm, the acceptance rule is *not* the Metropolis rule that considers the ratio of two weights. Here it is the probability itself. Hence, whenever the probability becomes very low, the acceptance of moves decreases proportionally.

There is another class of problems that can be sampled with this algorithm: those that are deterministic but for which the domain where the oracle function is one is highly non-compact. In this case, the key requirement is that the sampling algorithm is ergodic: it should avoid getting stuck in small islands where the oracle function is one. If that can be achieved, then we can use exactly the same approach as before, be it that now the oracle function behaves like a more or less random telegraph function in space. Still, we can define $v_i \equiv \int d\boldsymbol{x}\, P_{\mathcal{O}}(\boldsymbol{x})$ as before.

6.2.2 Configurational bias approach

In the way it has been formulated above, there is a problem with this approach: as the system moves into a region where $P_{\mathcal{O}}(\boldsymbol{x})$ is very low, the acceptance of moves becomes very small and hence the 'diffusion coefficient' that determines the rate at which configuration space is sampled, would become small. As a consequence, sampling of the wings of the distribution may not converge.

One way to mitigate the sampling problem is to use an approach that resembles configurational bias MC (CBMC) [213], but is different in some respects. The key point to note is that, if we know all random numbers that determine the value of the oracle function – including the random numbers that control the behaviour of the stochastic minimiser – then in the extended space of coordinates and random numbers, the value of the oracle function is always the same for a given point.

One way to exploit this would be to generate a random walk between points that are surrounded by a 'cloud' of k points where we compute the oracle function (k is arbitrary, but as we shall see later, it may pay to make it large). We denote the central point (*i.e.* the one to which or from which moves are attempted) by $\boldsymbol{x}_{\mathrm{B}}$, where 'B' stands for 'backbone'. The reason for calling this point a 'backbone' point is that we will be sampling the k points connected to it, but we will not compute the oracle function at this very point. Hence, $\boldsymbol{x}_{\mathrm{B}}$ may even be located in a region where the oracle function is strictly zero. The coordinates of the k cloud points around $\boldsymbol{x}_{\mathrm{B}}$ are given by:

$$\boldsymbol{x}_{\mathrm{B},i} = \boldsymbol{x}_{\mathrm{B}} + \Delta_i \tag{6.10}$$

with $i = \{1, 2, \cdots, k\}$. The vectors Δ are generated by some stochastic protocol: e.g. the vectors may be uniformly distributed in a hypersphere with radius R_h. The precise choice of the protocol does not matter, as long as the rules are not changed during the simulation. For a fixed protocol, the set $\boldsymbol{x}_{\mathrm{B},i}$ is uniquely determined by a set of random numbers $\mathcal{R}_{\mathrm{B}}$. It is convenient (but not essential) to choose the protocol such that any acceptable trial direction about a backbone point is equally likely to be generated. Finally, we note that the value of the oracle function $\mathcal{O}_i$ for a given point $\boldsymbol{x}_{\mathrm{B},i}$ is uniquely determined by another set of random numbers $\mathcal{R}_{\mathcal{O}}$.

We now define an extended state space

$$\tilde{\boldsymbol{x}}_{\mathrm{B}} \equiv \{\boldsymbol{x}_{\mathrm{B}}, \mathcal{R}_{\mathrm{B}}, \mathcal{R}_{\mathcal{O}}\} . \tag{6.11}$$

In this space, the oracle functions are no longer fluctuating quantities.

We can now construct a MCMC to visit (but not sample) backbone points. To this end, we compute the 'Rosenbluth weight' of point $\tilde{\boldsymbol{x}}_{\mathrm{B}}$ as

$$W(\tilde{\boldsymbol{x}}_{\mathrm{B}}) = \sum_{i=1}^{k} \mathcal{O}_i \omega_i, \tag{6.12}$$

where $\mathcal{O}_i \equiv \mathcal{O}(\tilde{\boldsymbol{x}}_{\mathrm{B},i})$ and $\omega_i \equiv \omega(\tilde{\boldsymbol{x}}_{\mathrm{B},i})$ is some arbitrary (Boltzmann) bias.

We can then construct a MCMC algorithm where the acceptance of a trial move from the 'old' $\tilde{\boldsymbol{x}}_{\mathrm{B}}^{(o)}$ to the 'new' $\tilde{\boldsymbol{x}}_{\mathrm{B}}^{(n)}$ is given by

$$P_{\mathrm{acc}}(o \to n) = \mathrm{Min}\left\{1, \frac{W(\tilde{\boldsymbol{x}}_{\mathrm{B}}^{(n)})}{W(\tilde{\boldsymbol{x}}_{\mathrm{B}}^{(o)})}\right\} \tag{6.13}$$

As the probabilities to generate the trial directions for forward and backward moves, and the generation of random numbers that determine the value of the oracle function are also uniform, the resulting MC algorithm satisfies super-detailed balance and a given backbone point $\tilde{\boldsymbol{x}}_{\mathrm{B}}$ will be visited with a probability proportional to $W(\tilde{\boldsymbol{x}}_{\mathrm{B}})$.

Note that during a trial move, the state of the old point is not changed, hence it retains the same trial directions and the same set $\{\mathcal{R}_{\mathcal{O}}\}$. If the trial move is rejected, it is this 'extended point' that is sampled again.

6.2.3 Sampling

To discuss sampling, it is best to first discuss a 'thought-algorithm' *i.e.* a valid algorithm that we can construct, but that we would never use in practice. In our thought algorithm, we consider the transition between one particular point, say i_o in the cloud around the old backbone position and another point i_n in the cloud around the new backbone position. Note that the statistical weight of these points depends on $\tilde{\boldsymbol{x}}_{\mathrm{B}}^{(o)}$ and $\tilde{\boldsymbol{x}}_{\mathrm{B}}^{(n)}$, respectively. We denote these statistical weights by $P(\tilde{\boldsymbol{x}}_{\mathrm{B}}^{(o)})$ and $P(\tilde{\boldsymbol{x}}_{\mathrm{B}}^{(n)})$. We can now write down the detailed balance condition:

$$P(\tilde{\boldsymbol{x}}_{\mathrm{B}}^{(o)}) P_{\mathrm{gen}}(\tilde{\boldsymbol{x}}_{\mathrm{B}}^{(n)}) P_{\mathrm{sel}}(i_n) P_{\mathrm{acc}}(o \to n) = P(\tilde{\boldsymbol{x}}_{\mathrm{B}}^{(n)}) P_{\mathrm{gen}}(\tilde{\boldsymbol{x}}_{\mathrm{B}}^{(o)}) P_{\mathrm{sel}}(i_o) P_{\mathrm{acc}}(n \to o), \tag{6.14}$$

where $P_{\mathrm{sel}}(i_n)$ denotes the probability to select point i_n from among the cloud of points around $\boldsymbol{x}_{\mathrm{B}}^{(n)}$ (and similarly, for $P_{\mathrm{sel}}(i_o)$). We now make the following choice for P_{sel}:

$$P_{\mathrm{sel}}(i_n) = \frac{\mathcal{O}(i_n)\omega(i_n)}{\sum_{i'=1}^{k} \mathcal{O}(i'_n)\omega(i'_n)} = \frac{\mathcal{O}(i_n)\omega(i_n)}{W(\tilde{\boldsymbol{x}}_{\mathrm{B}}^{(n)})}, \tag{6.15}$$

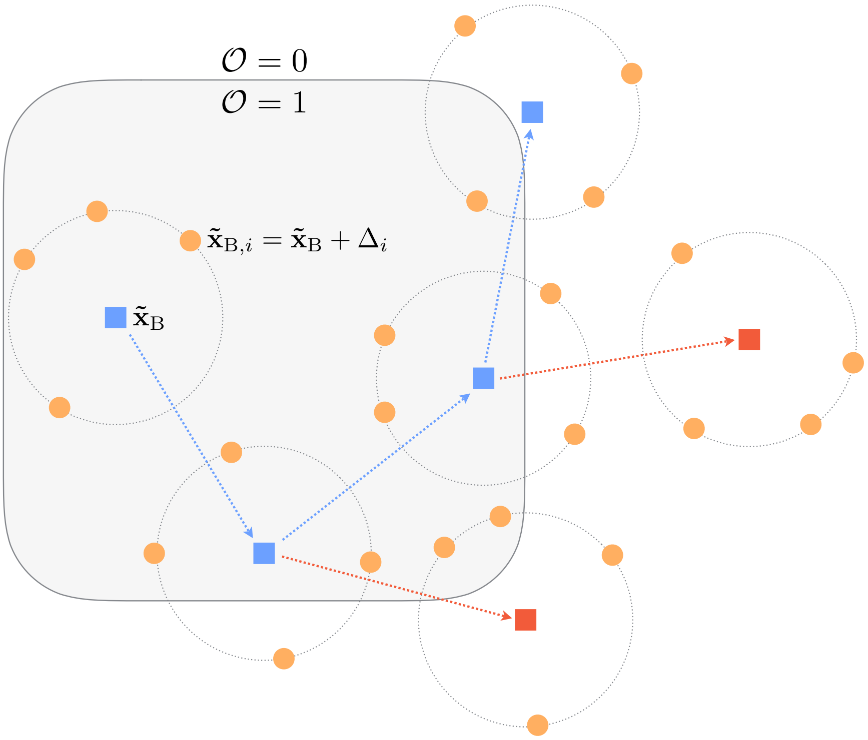

Fig. 6.1 ‘Cloud’ sampling: illustration of the configurational bias approach for a simple oracle defined by the gray shaded region, such that $\mathcal{O} = 1$ inside the gray boundary and $\mathcal{O} = 0$ outside. Blue and red squares are the accepted and rejected backbone points $\tilde{\mathbf{x}}_{\mathrm{B}}$, respectively. The ‘cloud’ points $\tilde{\mathbf{x}}_{\mathrm{B},i} = \tilde{\mathbf{x}}_{\mathrm{B}} + \Delta_i$ are represented by orange circles. In this example we randomly sample $k = 4$ ‘cloud’ points from a circle of fixed radius centred on the backbone point (dotted circles). Each ‘cloud’ is sampled with probability proportional to the Rosenbluth weight defined in Eq. (6.12). Note that valid backbone points are not required to fall in the region where $\mathcal{O} = 1$ since the Rosenbluth weight does not depend on the value of the oracle at the backbone point.

With this definition of the selection probability, we can write:

$$\frac{P(\tilde{\mathbf{x}}_{\mathrm{B}}^{(o)})}{P(\tilde{\mathbf{x}}_{\mathrm{B}}^{(n)})} = \frac{\mathcal{O}(i_o)\omega(i_o)}{\mathcal{O}(i_n)\omega(i_n)} \tag{6.16}$$

where we have used the fact that the generation probabilities for forward and backward moves are equal and we have inserted Eq. (6.13) for the ratio of the acceptance probabilities. Eq. (6.16) implies that in equilibrium, the probability to occupy state i_o is proportional to $\mathcal{O}(i_o)\omega(i_o)$, where it should be stressed that the value of the oracle function depends on both the spatial coordinates of point i_o and on the set of random numbers $\{\mathcal{R}_{\mathcal{O}}\}$ that, together, determine the value of $\mathcal{O}(i_o)$. If we were to average over all possible values of the random numbers $\{\mathcal{R}_{\mathcal{O}}\}$ then it is clear that the probability to sample a state with the spatial coordinates of the point i_o is proportional to $\langle \mathcal{O}(i_o) \rangle\, \omega(i_o)$. In other words, the algorithm described above samples all points in configuration space with a probability proportional to the local average of the oracle function and to the (usually Boltzmann) bias evaluated at that point.

Whilst the above description of the sampling strategy allows us to establish that all points in space are sampled with the correct frequency, it is not an efficient algorithm. The reason is obvious: in order to compute the weights W, the oracle function must be computed for k points, and yet in the naive version of the algorithm, only one point is sampled. In practice, we take steps between backbone points sampled according to Eq. (6.13) and keep all k cloud points for all the accepted backbone points, as described below. An illustration of the method is given in Fig. 6.1. Efficiency can be further improved using the approach underlying 'waste-recycling' Monte Carlo [214], we can in fact include all points in the sampling, even if the actual trial backbone move is rejected.

For every backbone point $\tilde{\mathbf{x}}_{\mathrm{B}}$ visited, we can compute the observable (say A) of the set of k cloud points as follows:

$$A_{\text{sampled}} = \frac{\sum_{i=1}^{k} \mathcal{O}_i \omega_i A_i}{\sum_{i=1}^{k} \mathcal{O}_i \omega_i} \tag{6.17}$$

The average of A during a MCMC simulation of L steps is:

$$\langle A \rangle = \frac{1}{L} \sum_{j=1}^{L} \left(\frac{\sum_{i=1}^{k} \mathcal{O}_i \omega_i A_i}{\sum_{i=1}^{k} \mathcal{O}_i \omega_i} \right)_j \tag{6.18}$$

where the index j labels the different backbone states visited.

6.2.4 Parallel Tempering

Parallel Tempering (PT) [148, 149] is a Monte Carlo scheme that targets the slow equilibration of systems characterised by large free energy barriers that prevent the efficient equilibration of a MCMC random walk. In PT, m replicas of the system are simulated simultaneously at different temperatures, different chemical potentials [215] or different Hamiltonians [216, 217]. Configurations are then swapped among replicas, thus making 'high temperature' regions available to 'low temperature' ones and *vice versa*. In the basin volume calculations of Refs. [34–36, 155] and discussed in Chapt. 2, 3, 4, Hamiltonian PT is essential to achieving fast equilibration of the replicas' MCMC random walks performed inside the body of the basin with different applied biases.

The configurational bias approach to 'cloud' sampling embodied by Eq. (6.13) can be easily generalised to PT to find an acceptance rule for the swap of configurations between replicas i and j

$$P_{\text{acc}}(i \to j) = \text{Min}\left\{1, \frac{W(\tilde{\boldsymbol{x}}_{\text{B}}^{(i)}, \omega^{(j)})W(\tilde{\boldsymbol{x}}_{\text{B}}^{(j)}, \omega^{(i)})}{W(\tilde{\boldsymbol{x}}_{\text{B}}^{(i)}, \omega^{(i)})W(\tilde{\boldsymbol{x}}_{\text{B}}^{(j)}, \omega^{(j)})}\right\} \tag{6.19}$$

where we defined the Rosenbluth weight $W(\tilde{\boldsymbol{x}}_{\text{B}}^{(i)}, \omega^{(j)}) = \sum_{l=1}^{k} \mathcal{O}(\tilde{\boldsymbol{x}}_{\text{B},l}^{(i)})\omega^{(j)}(\tilde{\boldsymbol{x}}_{\text{B},l}^{(i)})$. It is important to note that PT is truly an equilibrium Monte Carlo method: the microscopic equilibrium of each ensemble is not disturbed by the swaps.

6.2.5 Combine with 'Waste-recycling' MC

Using a CBMC-style approach would increase the speed with which the relevant configuration space is explored. However, it has the drawback that it may be wasteful: generating a trial move involves computing k oracle functions and, in normal CBMC the points this generated would not be sampled at all if the trial move is rejected.

However, we can do better by using 'waste-recycling' MC [214]. In that case we can combine the information of the accepted and the rejected states in our sampling. Specifically, we denote the probability to accept a move from an old state o to a new state n by $P_{\text{acc}}(o \to n)$, then, normally we would sample $A_{\text{sampled}}(n)$ if the move is accepted and $A_{\text{sampled}}(o)$ otherwise. However, we can do better by combining the information and sample

$$A_{\text{wr}} = P'_{\text{acc}}(o \to n)A_{\text{sampled}}(n) + [1 - P'_{\text{acc}}(o \to n)]A_{\text{sampled}}(o) \tag{6.20}$$

where P'_{acc} denotes the acceptance probability for *any* valid MCMC algorithm (not just Metropolis). In fact, it is convenient to use the symmetric Barker rule [218] to compute P'_{acc}. In that case, we would sample

$$A_{wr} = \frac{\left(\sum_{i=1}^{k} \mathcal{O}_i \omega_i A_i\right)_{old} + \left(\sum_{i=1}^{k} \mathcal{O}_i \omega_i A_i\right)_{new}}{\left(\sum_{i=1}^{k} \mathcal{O}_i \omega_i\right)_{old} + \left(\sum_{i=1}^{k} \mathcal{O}_i \omega_i\right)_{new}} \tag{6.21}$$

Hence, all $2k$ points that have been considered are included in the sampling.

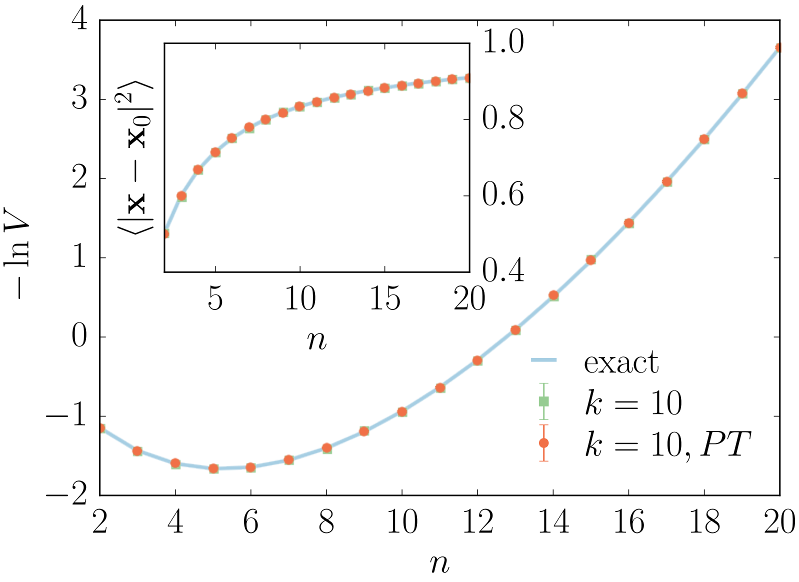

Fig. 6.2 Deterministic oracle: Volume calculation for an n-ball with radius $R = 0.5$ and $n \in [2,20]$. Numerical results (symbols) were obtained by the configurational bias approach of Eq. (6.13) and Eq. (6.19) (PT), with k 'cloud' points, and MBAR. Inset: mean square displacement computed by Eq. (6.18). Solid blue lines are analytical results and error bars refer to twice the standard error (as estimated by MBAR for the volume).

6.3 Numerical Results

6.3.1 Basin volume calculations

We test the proposed configurational bias approach by numerically computing the basin volume (probability mass) for a stochastic oracle function as defined in Eq. (6.5). We choose a few simple oracle functions, for which the integral in Eq. (6.5) can be solved analytically.

The volume calculations are performed using the multistate-Bennett acceptance ratio method (MBAR) [188] as described in Chapt. 4. In essence, we compute the dimensionless free energy difference between a region of known volume $\widehat{f}_{\text{ref}} = -\ln V_{\text{ref}} + c$ and the equilibrium distribution of points sampled uniformly within the basin $\widehat{f}_{\text{tot}} = -\ln V_{\text{tot}} + c$, estimated by MBAR up to an additive constant c. Since $f_{\text{ref}} = -\ln V_{\text{ref}}$ is known, we obtain the basin volume as $f_{\text{tot}} = f_{\text{ref}} + (\widehat{f}_{\text{tot}} - \widehat{f}_{\text{ref}})$. We use 15 replicas with positive coupling constants for all examples discussed herein.

First, we test the method for a deterministic oracle, namely a simple n-ball of known volume $V_{n\text{-ball}} = \pi^{n/2} R^n / \Gamma(n/2+1)$ with radius $R = 0.5$ and $n \in [2,20]$. As shown in Fig. 6.2 we correctly recover the volume and the mean square displacement using the acceptance rule

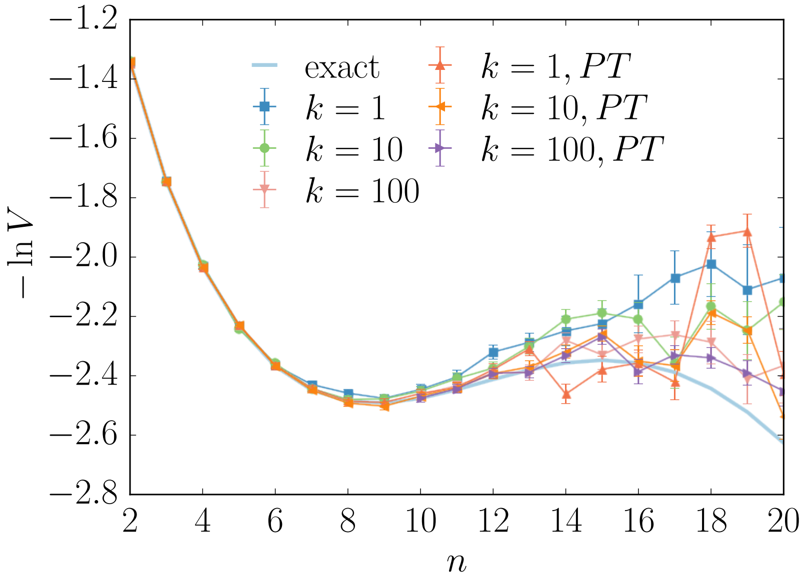

Fig. 6.3 Stochastic oracle: Volume calculation for the oracle defined in Eq. (6.22) with radius $R = 0.5$, $\lambda = 0.1$ and dimensions $n \in [2,20]$. Symbols (lines are guide to the eye) are numerical results obtained by the configurational bias approach of Eq. (6.13) and Eq. (6.19) (PT), with k 'cloud' points, and MBAR. Solid blue line is the analytical result and error bars refer to twice the standard error as estimated by MBAR. At large n accuracy increases by increasing k as the random walker diffuses more efficiently through regions of space where $\langle \mathcal{O} \rangle \ll 1$. Implementing PT also improves equlibration for small k by allowing the walker to escape low density regions when stuck.

defined in Eq. (6.13) for $k = 10$ 'cloud' points, with and without parallel tempering swap moves, with acceptance rule defined in Eq. (6.19). Hence, the algorithm is clearly sampling the correct equilibrium distributions.

We test the method for a stochastic oracle function defined as

$$\mathcal{O}(\boldsymbol{x}) = \begin{cases} 1 & \text{if } |\boldsymbol{x}| < R \\ \text{Uniform}[0,1] < \exp[-(|\boldsymbol{x}| - R)/\lambda] & \text{if } |\boldsymbol{x}| \geq R \end{cases} \tag{6.22}$$

with volume

$$V = 2(R^n/n + \lambda^n \exp(R/\lambda)\Gamma(n, R/\lambda))\pi^{n/2}R^n/\Gamma(n/2),$$

where $\Gamma(a,x)$ is the incomplete gamma function. Results for dimensions $n \in [2,20]$, $R = 0.5$ and $\lambda = 0.1$ are shown in Fig. 6.3. Note that, despite the volume being finite, the basin is unbounded in the sense that the average value of the oracle only tends to zero as as $|\boldsymbol{x}| \to \infty$. As the dimensionality of the basin increases, all of the volume will concentrate

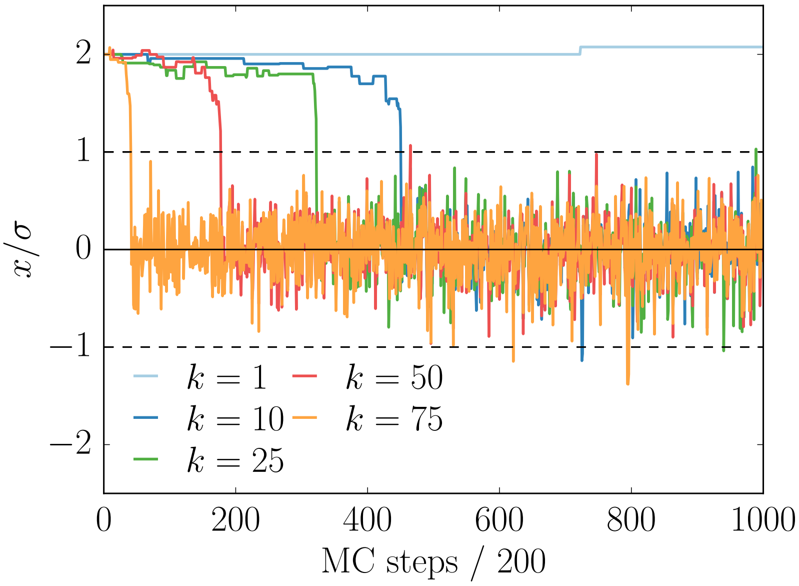

Fig. 6.4 Transition state finding: we consider the one-dimensional problem of identifying a transition state x_{tr}, corresponding to the location of a Gaussian energy barrier separating a reactant and a product with the same energy. The oracle, defined (symmetrically) by the stochastic oracle in Eq. (6.23), corresponds to the outcome of a 'reaction experiment', *i.e.* $\mathcal{O}(x) = 1$ if from position x the reaction is successful, and $\mathcal{O}(x) = 0$ otherwise. We find the transition state by allowing a random walker to diffuse to $x_{\mathrm{tr}} = 0$, the position along the reaction coordinate where the probability of crossing is highest. A series of random walks are performed according to Eq. (6.13) for different numbers of 'cloud' points k. The walkers are constrained to reject moves for which the energy is below that of the initial position, thus excluding reactants and products from the sampling. The figure shows the position of the walker backbone along the reaction coordinate as a function of the number of MCMC steps. For increasing k the random walkers diffuse more efficiently and therefore converge faster to the transition state $x_{\mathrm{tr}} = 0$. Traditional single-point sampling does not move at all from the initial condition.

away from the centre of mass in regions of space where the oracle has a high probability of returning 0. Hence, it becomes more difficult for a random walker to diffuse efficiently as the dimensionality of space increases. We can verify this in Fig. 6.3: for $n < 6$ results seem to be independent of the number of 'cloud' points and of whether PT swaps are implemented. However, growing deviations are observed for increasing n and accuracy increases significantly for growing number of 'cloud' points k and with the use of PT, whose non-local moves allow the walker to escape regions of low density (for which $\langle\mathcal{O}\rangle \ll 1$) when stuck.

6.3.2 Transition state finding

In this example we show that our approach can be used to efficiently identify the transition state along a known reaction coordinate. As an illustration, we consider the (trivial) one-dimensional problem of identifying the transition state x_{tr}, corresponding to the location of a Gaussian energy barrier separating a reactant and a product with the same energy. The oracle, in this case, corresponds to the outcome of a 'reaction experiment', *i.e.* $\mathcal{O}(x) = 1$ if from position x the reaction is successful, and $\mathcal{O}(x) = 0$ otherwise. We find the transition state by allowing a random walker to diffuse to x_{tr}, the position along the reaction coordinate where the probability of crossing is highest. We do so for varying numbers of cloud points k and show that our method outperforms traditional 'single-point' sampling.

Note that points in the transition-state ensemble (in the one-dimensional case: just one point) are characterised by the property that the committor has an average value of 0.5. However, any individual trajectory will either be crossing ("1") or non-crossing ("0"). Hence, the 'signal' is stochastic. As anticipated, we consider the one-dimensional case of a particle with kinetic energy K sampled according to the 1-dimensional Maxwell Boltzmann distribution, crossing a Gaussian barrier with height $U_{\mathrm{tr}} = 30kT$ and variance $\sigma^2 = 1$ [1]. We define the oracle symmetrically such as

$$\mathcal{O}(x) = \begin{cases} 1 & \text{if } K > U_{\mathrm{tr}} - U(x) \\ 0 & \text{if } K \leq U_{\mathrm{tr}} - U(x) \end{cases} \tag{6.23}$$

and constrain the walk to reject moves for which the energy is below that of the initial position, such that $\mathcal{O} = 0$ if $U(x) < U(x_0)$; we choose $x_0 = 2\sigma$. By thus constraining the sampling, we are excluding the 'reactant' and 'product' states from our sampling. In Fig. 6.4 we show results for backbone step-size 0.25σ, 'cloud' radius 0.25σ and varying number of 'cloud' points k. One can clearly see that, as the number of 'cloud' points increases, the system diffuses faster towards the transitions state, whilst for the traditional single-point sampling, the walker does not move at all from the initial position.

6.4 Relation to earlier work

In their 1999 paper, Ceperley and Dewing [212] consider a different situation where normal 'Metropolis' sampling fails, namely the case where the calculation of the energy function is subject to statistical errors (with zero mean). In that case, we cannot use the conventional Metropolis rule $P_{\mathrm{acc}} = \mathrm{Min}\{1, \exp(-\beta\Delta u)\}$, where u is the instantaneous value of the en-

---

[1] We choose as our unit of length σ, hence in our reduced units $kT = \sigma^2$

ergy difference, because what is needed to compute the correct acceptance probability is $\exp(-\beta\langle\Delta u\rangle)$, but what is sampled is $\langle\exp(-\beta\Delta u)\rangle \neq \exp(-\beta\langle\Delta u\rangle)$. Ceperley and Dewing showed that if the fluctuations in the energy of the individual states, and therefore the fluctuations in Δu are normally distributed, and if the variance in energy is the same for all states, then we can still get an algorithm that samples the correct Boltzmann distribution, if we use as acceptance rule

$$P_{\text{acc}} = \text{Min}\{1, \exp[-\beta\Delta u - (\beta\sigma)^2/2]\} \tag{6.24}$$

where $\sigma^2 = 2\sigma_s^2$, with σ_s denoting the variance in the energy of the individual states. Note that the situation considered in Ref. [212] is very different from the case that we consider here, as we focus on the situations where the average of the (fluctuating) oracle functions is precisely the weight function that we wish to sample. However, the current approach allows us to rederive the CD result. We note that, as before, we can consider extended states characterised by the spatial coordinates of the system and by the random variables that characterise the noise in the energy function. First, we note the average Boltzmann factor of extended state i is

$$\langle P_i\rangle = \exp[-\beta\langle u\rangle_i]\exp[+(\beta\sigma_s)^2/2] \tag{6.25}$$

and therefore

$$\frac{\langle P_n\rangle}{\langle P_o\rangle} = \exp[-\beta\langle\Delta u\rangle] \tag{6.26}$$

Hence, the average Boltzmann factor of any state i is still proportional to the correct Boltzmann weight. However, an MCMC algorithm using the instantaneous Boltzmann weights would not lead to correct sampling as super-detailed balance yields

$$\frac{P_n(\boldsymbol{x}_n)}{P_o(\boldsymbol{x}_o)} = \exp[-\beta\Delta u] \tag{6.27}$$

and hence

$$\left\langle\frac{P_n}{P_o}\right\rangle = \exp[-\beta\langle\Delta u\rangle + (\beta\sigma)^2/2] \tag{6.28}$$

which is not equal to

$$\frac{\langle P_n\rangle}{\langle P_o\rangle} = \exp[-\beta\langle\Delta u\rangle] \tag{6.29}$$

If, however we would use the CD acceptance rule, we would get

$$\begin{aligned}\left\langle\frac{P_n}{P_o}\right\rangle &= \exp[-\beta\langle\Delta u\rangle + (\beta\sigma)^2/2] \times \exp[-(\beta\sigma)^2/2] \\ &= \exp[-\beta\langle\Delta u\rangle] = \frac{\langle P_n\rangle}{\langle P_o\rangle}\end{aligned} \tag{6.30}$$

Hence, with this rule the states would (on average) be visited with the correct probability. Note that, as the noise enters non-linearly in the acceptance rule, the CD algorithm is very different from the one that we derived above. Note also that the present derivation makes it clear that the CD algorithm can be easily generalised to cases where the noise in the energy is not normally distributed, as long as the distribution of the noise is state-independent.

6.5 Conclusions

Thus far the algorithm described above was presented as a method to perform Monte Carlo sampling in cases where the weight function itself is fluctuating. However, the method might also be used to control certain experiments that study stochastic events (e.g. crystal nucleation, cell death or even the effect of advertising). Often, the occurrence of the desired event depends on a large number of variables (temperature, pressure, pH, concentration of various components) and we would like to select the optimal combination. However, as the desired event itself is stochastic, individual measurements provide little guidance. One might aim to optimise the conditions by accumulating sufficient statistics for individual state points. However, such an approach is expensive. The procedure described in the preceding sections suggests that it may be better to perform experiments in a ‘cloud’ of state points around a backbone point. We could then accept or reject the trial move to a new backbone state using the same rule as in Eq. (6.13).

Chapter 7

Conclusions and outlook

In this thesis a robust numerical protocol for the characterization of the complexity of energy landscapes has been established. The capabilities of the approach have been demonstrated within the context of the computation of the configurational entropy of two and three-dimensional jammed packings. By means of numerical simulation we have demonstrated the extensivity of the granular entropy as proposed by Edwards for three-dimensional jammed soft-sphere packings and produced a direct test of the Edwards conjecture for the equivalent two dimensional systems. We find that Edwards' hypothesis of equiprobability of all jammed states holds *only* at the (un)jamming density, that is precisely the point of practical significance for many granular systems.

Numerous questions on the the generality and possible implications of our findings remain to be explored. It needs to be established whether our results on the equiprobability of jammed packings are valid in three dimensions, and a full finite-size scaling analysis of our entropy calculations over multiple densities is still lacking. It remains to be clarified to what extent our conclusions are protocol dependent, specifically what is the dependence on the initial state of the system and on the jamming protocol. Furthermore it needs to be elucidated whether there is a distinction between 'direct' and 'tapping' protocols, and what is the effect of shear on the system.

It would be hard to imagine that equiprobability of states and jamming criticality (whose super-universal character seems to be independent of the protocol used to generate the jammed configurations [219]) occur at the same density by pure coincidence. Our analysis points in the direction of a fundamental connection between the two, but this notion needs to be clarified further. It would be interesting to probe whether the emergence of equiprobability at a characteristic (critical) point can be observed in other out-of-equilibrium problems, such as the random organization process [220] and other absorbing state models [221]. Since both jammed packings and absorbing state models have been found to exhibit hyperuniformity at the critical point [222, 223], it would then be natural to ask whether any connection can be established.

In this thesis two new recipes for the computation of high-dimensional volumes have been presented, that improve on the established approach by either providing more statistically robust estimates of the volume or by exploiting the trajectories of the paths of steepest descent. Both methods also produced as a natural by-product unprecedented details on the structures of high-dimensional basins of attraction. It would be interesting to explore whether the density propagation method could be extended to other forms of dynamics and to probe whether information on the dilation of space gathered during the density propagation steps could be used to bias the sampling, in order to guarantee a faster convergence.

It would clearly be very exciting to use our protocol to study different phenomena. Studies of the shear yielding of jammed packings are already underway, but the emergence of the correct phenomenology only for large system sizes poses a challenge. The application of the method to spin and structural (thermal) glasses that are not amenable to analytical treatment would also be very interesting.

Finally, we have presented a novel Monte Carlo algorithm to tackle problems with fluctuating weight functions. This is a common situation, for instance, in machine learning when the “training” is performed by stochastic optimisation. The method has been shown to improve accuracy in the computation of the ‘volume’ of high dimensional ‘fluctuating’ basins of attraction and to be able to identify transition states along known reaction coordinates. We argue that the approach can be extended to the optimization of the experimental conditions for observing certain phenomena, for which individual measurements are stochastic and provide little guidance.

I could have listed more possible applications of the techniques developed in this thesis, but my aim is not to provide an exhaustive list, simply because more applications are likely to emerge with time. These conclusions mainly express my own excitement that a class of problems that had been intractable in the past can now be addressed numerically.

References

[1] S. Lloyd. “Computational capacity of the universe”. In: *Physical Review Letters* 88.23 (2002), p. 237901 (cited on page 1).

[2] M. Kac. “On the average number of real roots of a random algebraic equation (II)”. In: *Proceedings of the London Mathematical Society* 2.1 (1948), pp. 390–408 (cited on page 2).

[3] K. Farahmand. “On the average number of real roots of a random algebraic equation”. In: *The Annals of Probability* (1986), pp. 702–709 (cited on page 2).

[4] E. Bogomolny, O. Bohigas, and P. Leboeuf. “Distribution of roots of random polynomials”. In: *Physical Review Letters* 68.18 (1992), p. 2726 (cited on page 2).

[5] A. Edelman and E. Kostlan. “How many zeros of a random polynomial are real?” In: *Bulletin of the American Mathematical Society* 32.1 (1995), pp. 1–37 (cited on page 2).

[6] J. M. Rojas. “On the average number of real roots of certain random sparse polynomial systems”. In: *Lectures in Applied Mathematics-American Mathematical Society* 32 (1996), pp. 689–700 (cited on page 2).

[7] E. Kostlan. “On the expected number of real roots of a system of random polynomial equations”. In: *Foundations of Computational Mathematics* (2000), pp. 149–188 (cited on page 2).

[8] G. Malajovich and J. M. Rojas. “High probability analysis of the condition number of sparse polynomial systems”. In: *Theoretical Computer Science* 315.2 (2004), pp. 525–555 (cited on page 2).

[9] J.-M. Azaïs and M. Wschebor. “On the roots of a random system of equations. The theorem of Shub and Smale and some extensions”. In: *Foundations of Computational Mathematics* 5.2 (2005), pp. 125–144 (cited on page 2).

[10] D. Armentano and M. Wschebor. “Random systems of polynomial equations. The expected number of roots under smooth analysis”. In: *Bernoulli* 15.1 (2009), pp. 249–266 (cited on page 2).

[11] Y. V. Fyodorov, G. A. Hiary, and J. P. Keating. “Freezing transition, characteristic polynomials of random matrices, and the riemann zeta function”. In: *Physical Review Letters* 108.17 (2012), p. 170601 (cited on page 2).

[12] L. I. Nicolaescu. “Complexity of random smooth functions on compact manifolds. II”. In: *arXiv:1209.0639* (2012) (cited on page 2).

[13] Y. V. Fyodorov. “High-dimensional random fields and random matrix theory”. In: *arXiv:1307.2379* (2013) (cited on page 2).

[14] D. Cheng and A. Schwartzman. “On the Explicit Height Distribution and Expected Number of Local Maxima of Isotropic Gaussian Random Fields”. In: *arXiv:1503.01328* (2015) (cited on page 2).

[15] Y. V. Fyodorov, A. Lerario, and E. Lundberg. “On the number of connected components of random algebraic hypersurfaces”. In: *Journal of Geometry and Physics* 95 (2015), pp. 1–20 (cited on page 2).

[16] Y. V. Fyodorov. “Complexity of random energy landscapes, glass transition, and absolute value of the spectral determinant of random matrices”. In: *Physical Review Letters* 92.24 (2004), p. 240601 (cited on pages 2, 16).

[17] A. J. Bray and D. S. Dean. “Statistics of critical points of Gaussian fields on large-dimensional spaces”. In: *Physical Review Letters* 98.15 (2007), p. 150201 (cited on pages 2, 16).

[18] Y. V. Fyodorov and C. Nadal. “Critical behavior of the number of minima of a random landscape at the glass transition point and the Tracy-Widom distribution”. In: *Physical Review Letters* 109.16 (2012), p. 167203 (cited on pages 2, 16).

[19] A. Auffinger, G. Ben Arous, and J. Čern̆y. “Random matrices and complexity of spin glasses”. In: *Communications on Pure and Applied Mathematics* 66.2 (2013), pp. 165–201 (cited on pages 2, 16).

[20] Y. V. Fyodorov and P. Le Doussal. “Topology trivialization and large deviations for the minimum in the simplest random optimization”. In: *Journal of Statistical Physics* 154.1-2 (2014), pp. 466–490 (cited on pages 2, 16).

[21] C. Hughes, D. Mehta, and D. J. Wales. “An inversion-relaxation approach for sampling stationary points of spin model Hamiltonians”. In: *The Journal of Chemical Physics* 140.19 (2014), p. 194104 (cited on pages 2, 16).

[22] D. Mehta, T. Chen, J. D. Hauenstein, and D. J. Wales. “Communication: Newton homotopies for sampling stationary points of potential energy landscapes”. In: *The Journal of Chemical Physics* 141.12 (2014), p. 121104 (cited on pages 2, 16).

[23] J. Cleveland et al. “Certified counting of roots of random univariate polynomials”. In: *arXiv:1412.1717* (2014) (cited on pages 2, 16).

[24] D. Mehta, M. Niemerg, and C. Sun. “Statistics of stationary points of random finite polynomial potentials”. In: *Journal of Statistical Mechanics: Theory and Experiment* 2015.9 (2015), P09012 (cited on pages 2, 16).

[25] L. F. Cugliandolo and J. Kurchan. “Analytical solution of the off-equilibrium dynamics of a long-range spin-glass model”. In: *Physical Review Letters* 71.1 (1993), p. 173 (cited on pages 2, 16, 72).

[26] J. Kurchan, G. Parisi, and M. A. Virasoro. “Barriers and metastable states as saddle points in the replica approach”. In: *Journal de Physique I* 3.8 (1993), pp. 1819–1838 (cited on pages 2, 16).

[27] D. Mehta, D. A. Stariolo, and M. Kastner. “Energy Landscape of the Finite-Size Mean-field 3-Spin Spherical Model”. In: *Physical Review E* 87.arXiv: 1303.1520 (2013), p. 052143 (cited on pages 2, 16).

[28] A. Auffinger and G. Ben Arous. “Complexity of random smooth functions on the high-dimensional sphere”. In: *The Annals of Probability* 41.6 (2013), pp. 4214–4247 (cited on pages 2, 16, 72).

[29] E. Subag. “The complexity of spherical p-spin models-a second moment approach”. In: *arXiv preprint arXiv:1504.02251* (2015) (cited on pages 2, 16).

[30] S. Sastry. “The relationship between fragility, configurational entropy and the potential energy landscape of glass-forming liquids”. In: *Nature* 409.6817 (2001), pp. 164–167 (cited on pages 2, 16).

[31] A. Banerjee, S. Sengupta, S. Sastry, and S. M. Bhattacharyya. “Role of Structure and Entropy in Determining Differences in Dynamics for Glass Formers with Different Interaction Potentials”. In: *Physical Review Letters* 113.22 (2014), p. 225701 (cited on pages 2, 16).

[32] N. Xu, D. Frenkel, and A. J. Liu. “Direct determination of the size of basins of attraction of jammed solids”. In: *Physical Review Letters* 106.24 (2011), p. 245502 (cited on pages 2, 8, 9, 13, 14, 16, 18, 20, 21, 25, 40, 62, 72, 91, 139).

[33] D. Frenkel, D. Asenjo, and F. Paillusson. “The other entropy”. In: *Molecular Physics* 111 (2013), p. 3641 (cited on pages 2, 16, 20, 25, 72).

[34] D. Asenjo, F. Paillusson, and D. Frenkel. “Numerical Calculation of Granular Entropy”. In: *Physical Review Letters* 112.9 (2014), p. 098002 (cited on pages 2, 8, 9, 13, 14, 16, 18–20, 23–28, 35, 40, 45, 62, 72, 91, 96, 139).

[35] S. Martiniani, K. J. Schrenk, J. D. Stevenson, D. J. Wales, and D. Frenkel. “Turning intractable counting into sampling: Computing the configurational entropy of three-dimensional jammed packings”. In: *Phys. Rev. E* 93 (1 2016), p. 012906 (cited on pages 2, 11, 40, 44, 46, 54, 62, 72, 91, 96).

[36] S. Martiniani, K. J. Schrenk, J. D. Stevenson, D. J. Wales, and D. Frenkel. “Structural analysis of high-dimensional basins of attraction”. In: *Physical Review E* 94.3 (2016), p. 031301 (cited on pages 2, 40, 55, 72, 91, 96).

[37] M. A. Miller and D. J. Wales. “Energy landscape of a model protein”. In: *Journal of Chemical Physics* 111.14 (1999), pp. 6610–6616 (cited on pages 2, 56).

[38] J. N. Onuchic, Z. Luthey-Schulten, and P. G. Wolynes. “Theory of protein folding: the energy landscape perspective”. In: *Annual review of physical chemistry* 48.1 (1997), pp. 545–600 (cited on page 2).

[39] P. Charbonneau, J. Kurchan, G. Parisi, P. Urbani, and F. Zamponi. “Glass and Jamming Transitions: From Exact Results to Finite-Dimensional Descriptions”. In: *arXiv preprint arXiv:1605.03008* (2016) (cited on pages 2, 54).

[40] G. Biroli and P. Urbani. “Breakdown of Elasticity in Amorphous Solids”. In: *arXiv preprint arXiv:1601.06724* (2016) (cited on page 2).

[41] D. A. Wiley, S. H. Strogatz, and M. Girvan. “The size of the sync basin”. In: *Chaos: An Interdisciplinary Journal of Nonlinear Science* 16.1 (2006), p. 015103 (cited on pages 2, 9, 56).

[42] P. J. Menck, J Heitzig, N Marwan, and J Kurths. “How basin stability complements the linear-stability paradigm”. In: *Nature Physics* 9.2 (2013), pp. 89–92 (cited on pages 2, 56).

[43] G. Wainrib and J. Touboul. “Topological and dynamical complexity of random neural networks”. In: *Physical Review Letters* 110.11 (2013), p. 118101 (cited on pages 2, 16, 72).

[44] A. Choromanska, M. Henaff, M. Mathieu, G. Ben Arous, and Y. LeCun. “The loss surface of multilayer networks”. In: *arXiv:1412.0233* (2014) (cited on pages 2, 16).

[45] L. Sagun, V. U. Guney, and Y. LeCun. “Explorations on high dimensional landscapes”. In: *arXiv:1412.6615* (2014) (cited on pages 2, 16, 56, 72).

[46] P. Chaudhari and S. Soatto. “Trivializing The Energy Landscape Of Deep Networks”. In: *arXiv:1511.06485* (2015) (cited on pages 2, 16).

[47] A. J. Ballard, J. D. Stevenson, R. Das, and D. J. Wales. “Energy landscapes for a machine learning application to series data”. In: *The Journal of chemical physics* 144.12 (2016), p. 124119 (cited on pages 2, 56, 72).

[48] A. Ballard, J. D. Stevenson, and D. J. Wales. “Energy Landscapes of Machine Learning”. In: *in submission* (2016) (cited on pages 2, 56).

[49] A. Aazami and R. Easther. “Cosmology from random multifield potentials”. In: *Journal of Cosmology and Astroparticle Physics* 2006.03 (2006), p. 013 (cited on pages 2, 16).

[50] S.-H. H. Tye, J. Xu, and Y. Zhang. “Multi-field inflation with a random potential”. In: *Journal of Cosmology and Astroparticle Physics* 2009.04 (2009), p. 018 (cited on pages 2, 16).

[51] J. Frazer and A. R. Liddle. “Exploring a string-like landscape”. In: *Journal of Cosmology and Astroparticle Physics* 2011.02 (2011), p. 026 (cited on pages 2, 16, 56).

[52] J. Frazer and A. R. Liddle. “Multi-field inflation with random potentials: field dimension, feature scale and non-Gaussianity”. In: *Journal of Cosmology and Astroparticle Physics* 2012.02 (2012), p. 039 (cited on pages 2, 16).

[53] D. Battefeld, T. Battefeld, and S. Schulz. “On the unlikeliness of multi-field inflation: bounded random potentials and our vacuum”. In: *Journal of Cosmology and Astroparticle Physics* 2012.06 (2012), p. 034 (cited on pages 2, 16).

[54] J. Distler and U. Varadarajan. “Random polynomials and the friendly landscape”. In: *arXiv preprint hep-th/0507090* (2005) (cited on pages 2, 16).

[55] M. R. Douglas and S. Kachru. “Flux compactification”. In: *Reviews of Modern Physics* 79 (2007), pp. 733–796 (cited on pages 2, 16).

[56] B. Greene, D. Kagan, A. Masoumi, D. Mehta, E. J. Weinberg, and X. Xiao. “Tumbling through a landscape: Evidence of instabilities in high-dimensional moduli spaces”. In: *Physical Review D* 88.2 (2013), p. 026005 (cited on pages 2, 56).

[57] S. F. Edwards and R. B. S. Oakeshott. “Theory of powders”. In: *Physica A* 157 (1989), p. 1080 (cited on pages 2, 12, 16, 23, 24, 37, 38).

[58] S. Edwards. “The role of entropy in the specification of a powder”. In: *Granular Matter*. Springer, 1994, pp. 121–140 (cited on page 2).

[59] S. Edwards. “New kinds of entropy”. In: *Journal of statistical physics* 116.1-4 (2004), pp. 29–42 (cited on pages 3, 5, 6).

[60] S. Edwards. “The rheology of powders”. In: *Rheologica Acta* 29.6 (1990), pp. 493–499 (cited on pages 3, 6).

[61] D. Bi, S. Henkes, K. E. Daniels, and B. Chakraborty. “The Statistical Physics of Athermal Materials”. In: *Annual Review of Condensed Matter Physics* 6.1 (2015), p. 63 (cited on pages 3, 7, 13, 27, 38, 54).

[62] E. Nowak, J. Knight, M. Povinelli, H. Jaeger, and S. Nagel. “Reversibility and irreversibility in the packing of vibrated granular material”. In: *Powder technology* 94.1 (1997), pp. 79–83 (cited on pages 4, 7).

[63] S. Edwards and D. Grinev. “Granular materials: towards the statistical mechanics of jammed configurations”. In: *Advances in Physics* 51.8 (2002), pp. 1669–1684 (cited on pages 4, 38).

[64] S. Edwards. “The full canonical ensemble of a granular system”. In: *Physica A: Statistical Mechanics and its Applications* 353 (2005), pp. 114–118 (cited on page 5).

[65] R. Blumenfeld and S. F. Edwards. “On granular stress statistics: Compactivity, angoricity, and some open issues”. In: *The Journal of Physical Chemistry B* 113.12 (2009), p. 3981 (cited on pages 5, 6, 13, 54).

[66] S. Henkes, C. S. O’Hern, and B. Chakraborty. “Entropy and temperature of a static granular assembly: an ab initio approach”. In: *Physical Review Letters* 99.3 (2007), p. 038002 (cited on pages 5, 13, 27, 36, 54).

[67] R. Blumenfeld, J. F. Jordan, and S. F. Edwards. “Interdependence of the volume and stress ensembles and equipartition in statistical mechanics of granular systems”. In: *Physical Review Letters* 109.23 (2012), p. 238001 (cited on pages 6, 13).

[68] C. Monthus and J.-P. Bouchaud. “Models of traps and glass phenomenology”. In: *Journal of Physics A: Mathematical and General* 29.14 (1996), p. 3847 (cited on page 7).

[69] P. Sollich. “Rheological constitutive equation for a model of soft glassy materials”. In: *Physical Review E* 58.1 (1998), p. 738 (cited on page 7).

[70] J. Langer. “Shear-transformation-zone theory of plastic deformation near the glass transition”. In: *Physical Review E* 77.2 (2008), p. 021502 (cited on page 7).

[71] R. P. Behringer, D. Bi, B. Chakraborty, S. Henkes, and R. R. Hartley. “Why do granular materials stiffen with shear rate? Test of novel stress-based statistics”. In: *Physical review letters* 101.26 (2008), p. 268301 (cited on page 7).

[72] D. Bi and B. Chakraborty. “Rheology of granular materials: dynamics in a stress landscape”. In: *Philosophical Transactions of the Royal Society of London A: Mathematical, Physical and Engineering Sciences* 367.1909 (2009), pp. 5073–5090 (cited on page 7).

[73] J. Brujić, P. Wang, C. Song, D. L. Johnson, O. Sindt, and H. A. Makse. “Granular dynamics in compaction and stress relaxation”. In: *Physical review letters* 95.12 (2005), p. 128001 (cited on page 7).

[74] A. Chakravarty, S. F. Edwards, D. V. Grinev, M. Mann, T. E. Phillipson, and A. J. Walton. “Statistical mechanics and reversible states in quasi-static powders”. In: *Proceedings of the Workshop on the Quasi-static Deformations of Particulate Materials*. 2003 (cited on page 7).

[75] P. Philippe and D. Bideau. “Compaction dynamics of a granular medium under vertical tapping”. In: *EPL (Europhysics Letters)* 60.5 (2002), p. 677 (cited on page 7).

[76] E. Caglioti, V. Loreto, H. J. Herrmann, and M. Nicodemi. “A “tetris-like” model for the compaction of dry granular media”. In: *Physical Review Letters* 79.8 (1997), p. 1575 (cited on page 7).

[77] M. Nicodemi, A. Coniglio, and H. J. Herrmann. “Frustration and slow dynamics of granular packings”. In: *Physical Review E* 55.4 (1997), p. 3962 (cited on page 7).

[78] M. Nicodemi, A. Coniglio, and H. J. Herrmann. “Compaction and force propagation in granular packings”. In: *Physica A: Statistical Mechanics and its Applications* 240.3-4 (1997), pp. 405–418 (cited on page 7).

[79] M. Nicodemi. “Dynamical response functions in models of vibrated granular media”. In: *Physical review letters* 82.19 (1999), p. 3734 (cited on page 7).

[80] M. Nicodemi, A. Coniglio, and H. J. Herrmann. “Density fluctuations in a model for vibrated granular media”. In: *Physical Review E* 59.6 (1999), p. 6830 (cited on page 7).

[81] A. Prados, J. J. Brey, and B. Sánchez-Rey. “Hysteresis in vibrated granular media”. In: *Physica A: Statistical Mechanics and its Applications* 284.1 (2000), pp. 277–298 (cited on page 7).

[82] J. Berg, S. Franz, and M. Sellitto. “Testing the Edwards hypothesis in spin systems under tapping dynamics”. In: *The European Physical Journal B-Condensed Matter and Complex Systems* 26.3 (2002), pp. 349–356 (cited on page 7).

[83] G. Gradenigo, E. E. Ferrero, E. Bertin, and J.-L. Barrat. “Edwards thermodynamics for a driven athermal system with dry friction”. In: *Physical review letters* 115.14 (2015), p. 140601 (cited on page 7).

[84] K. Wang, C. Song, P. Wang, and H. A. Makse. “Angoricity and compactivity describe the jamming transition in soft particulate matter”. In: *EPL (Europhysics Letters)* 91.6 (2010), p. 68001 (cited on pages 7, 13).

[85] K. Wang, C. Song, P. Wang, and H. A. Makse. “Edwards thermodynamics of the jamming transition for frictionless packings: Ergodicity test and role of angoricity and compactivity”. In: *Physical Review E* 86 (1 2012), p. 011305 (cited on pages 7, 13, 62).

[86] S. McNamara, P. Richard, S. K. De Richter, G. Le Caër, and R. Delannay. “Measurement of granular entropy”. In: *Physical Review E* 80.3 (2009), p. 031301 (cited on pages 7, 13).

[87] S. McNamara, P. Richard, S. K. de Richter, G. Le Caër, R. Delannay, M. Nakagawa, and S. Luding. “Overlapping histogram method for testing edward’s statistical mechanics of powders”. In: *AIP Conference Proceedings*. Vol. 1145. 1. AIP. 2009, pp. 465–468 (cited on page 7).

[88] F. Paillusson and D. Frenkel. “Probing ergodicity in granular matter”. In: *Physical review letters* 109.20 (2012), p. 208001 (cited on page 7).

[89] F. Paillusson. “Devising a protocol-related statistical mechanics framework for granular materials”. In: *Physical Review E* 91.1 (2015), p. 012204 (cited on pages 7, 13, 14, 25).

[90] P. A. Gago, D. Maza, and L. A. Pugnaloni. “Ergodic-nonergodic transition in tapped granular systems: The role of persistent contacts”. In: *Papers in physics* 8.1 (2016), pp. 0–0 (cited on page 7).

[91] G. J. Willard. "Elementary Principles in Statistical Mechanics". In: *The Rational Foundation of Thermodynamics, New York, Charles Scribner's sons and London, Edward Arnold* (1902) (cited on pages 7, 38).

[92] G.-J. Gao, J. Bławzdziewicz, and C. S. O'Hern. "Frequency distribution of mechanically stable disk packings". In: *Physical Review E* 74 (2006), p. 061304 (cited on pages 7, 12, 14).

[93] G.-J. Gao, J. Blawzdziewicz, C. S. O'Hern, and M. Shattuck. "Experimental demonstration of nonuniform frequency distributions of granular packings". In: *Physical Review E* 80.6 (2009), p. 061304 (cited on pages 7, 12).

[94] R. K. Bowles and S. Ashwin. "Edwards entropy and compactivity in a model of granular matter". In: *Physical Review E* 83.3 (2011), p. 031302 (cited on page 8).

[95] R. H. Swendsen. "Statistical mechanics of colloids and Boltzmann's definition of the entropy". In: *American journal of physics* 74.3 (2006), pp. 187–190 (cited on page 8).

[96] D. Frenkel. "Why colloidal systems can be described by statistical mechanics: some not very original comments on the Gibbs paradox". In: *Molecular Physics* 112.17 (2014), pp. 2325–2329 (cited on page 8).

[97] M. E. Cates and V. N. Manoharan. "Celebrating Soft Matter's 10th anniversary: Testing the foundations of classical entropy: colloid experiments". In: *Soft Matter* 11 (33 2015), pp. 6538–6546 (cited on page 8).

[98] J. D. Chodera, W. C. Swope, J. W. Pitera, C. Seok, and K. A. Dill. "Use of the weighted histogram analysis method for the analysis of simulated and parallel tempering simulations". In: *Journal of Chemical Theory and Computation* 3.1 (2007), p. 26 (cited on page 9).

[99] J. F. Kok, E. J. R. Parteli, T. I. Michaels, and D. B. Karam. "The physics of windblown sand and dust". In: *Reports on Progress in Physics* 75 (2012), p. 106901 (cited on page 12).

[100] M. Van Hecke. "Jamming of soft particles: geometry, mechanics, scaling and isostaticity". In: *Journal of Physics: Condensed Matter* 22.3 (2010), p. 033101 (cited on page 12).

[101] A. J. Liu and S. R. Nagel. "Nonlinear dynamics: Jamming is not just cool any more". In: *Nature* 396.6706 (1998), p. 21 (cited on page 12).

[102] H. A. Makse and J. Kurchan. "Testing the thermodynamic approach to granular matter with a numerical model of a decisive experiment". In: *Nature* 415.6872 (2002), p. 614 (cited on page 12).

[103] C. Song, P. Wang, and H. A. Makse. "Experimental measurement of an effective temperature for jammed granular materials". In: *Proceedings of the National Academy of Sciences of the United States of America* 102.7 (2005), p. 2299 (cited on page 12).

[104] A. Barrat, J. Kurchan, V. Loreto, and M. Sellitto. "Edwards' measures: a thermodynamic construction for dense granular media and glasses". In: *Physical Review E* 63.5 (2001), p. 051301 (cited on page 12).

[105] F. Lechenault, F. da Cruz, O. Dauchot, and E. Bertin. “Free volume distributions and compactivity measurement in a bidimensional granular packing”. In: *Journal of Statistical Mechanics: Theory and Experiment* 2006.07 (2006), P07009 (cited on page 12).

[106] K. E. Daniels and N. W. Hayman. “Force chains in seismogenic faults visualized with photoelastic granular shear experiments”. In: *Journal of Geophysical Research: Solid Earth (1978–2012)* 113 (2008), B11411 (cited on page 12).

[107] J. Brujić, C. Song, P. Wang, C. Briscoe, G. Marty, and H. A. Makse. “Measuring the coordination number and entropy of a 3d jammed emulsion packing by confocal microscopy”. In: *Physical Review Letters* 98.24 (2007), p. 248001 (cited on page 13).

[108] V. Baranau, D. Hlushkou, S. Khirevich, and U. Tallarek. “Pore-size entropy of random hard-sphere packings”. In: *Soft Matter* 9.12 (2013), p. 3361 (cited on page 13).

[109] E. R. Nowak, J. B. Knight, E. Ben-Naim, H. M. Jaeger, and S. R. Nagel. “Density fluctuations in vibrated granular materials”. In: *Physical Review E* 57.2 (1998), p. 1971 (cited on page 13).

[110] M. Schröter, D. I. Goldman, and H. L. Swinney. “Stationary state volume fluctuations in a granular medium”. In: *Physical Review E* 71.3 (2005), p. 030301 (cited on page 13).

[111] D. S. Dean and A. Lefevre. “Possible test of the thermodynamic approach to granular media”. In: *Physical Review Letters* 90.19 (2003), p. 198301 (cited on page 13).

[112] S.-C. Zhao, S. Sidle, H. L. Swinney, and M. Schröter. “Correlation between Voronoi volumes in disc packings”. In: *EPL (Europhysics Letters)* 97.3 (2012), p. 34004 (cited on page 13).

[113] T. Aste and T. Di Matteo. “Emergence of Gamma distributions in granular materials and packing models”. In: *Physical Review E* 77.2 (2008), p. 021309 (cited on page 13).

[114] R. Blumenfeld and S. F. Edwards. “Granular entropy: Explicit calculations for planar assemblies”. In: *Physical Review Letters* 90.11 (2003), p. 114303 (cited on page 13).

[115] S.-C. Zhao and M. Schröter. “Measuring the configurational temperature of a binary disc packing”. In: *Soft Matter* 10.23 (2014), p. 4208 (cited on page 13).

[116] J. G. Puckett and K. E. Daniels. “Equilibrating temperaturelike variables in jammed granular subsystems”. In: *Physical Review Letters* 110.5 (2013), p. 058001 (cited on pages 13, 54).

[117] C. Briscoe, C. Song, P. Wang, and H. A. Makse. “Entropy of Jammed Matter”. In: *Physical Review Letters* 101 (18 2008), p. 188001 (cited on page 13).

[118] S. Henkes and B. Chakraborty. “Statistical mechanics framework for static granular matter”. In: *Physical Review E* 79 (6 2009), p. 061301 (cited on pages 13, 27, 28, 36, 50, 54, 144).

[119] J. H. Snoeijer, T. J. H. Vlugt, M. van Hecke, and W. van Saarloos. “Force network ensemble: a new approach to static granular matter”. In: *Physical Review Letters* 92.5 (2004), p. 054302 (cited on page 13).

[120] A. R. T. Van Eerd, B. P. Tighe, and T. J. H. Vlugt. “Numerical study of the force network ensemble”. In: *Molecular Simulation* 35.14 (2009), p. 1168 (cited on pages 13, 36).

[121] B. P. Tighe, J. H. Snoeijer, T. J. H. Vlugt, and M. van Hecke. “The force network ensemble for granular packings”. In: *Soft Matter* 6.13 (2010), p. 2908 (cited on pages 13, 36).

[122] B. P. Tighe and T. J. H. Vlugt. “Stress fluctuations in granular force networks”. In: *Journal of Statistical Mechanics: Theory and Experiment* 2011.04 (2011), P04002 (cited on pages 13, 36).

[123] C. S. O’Hern, L. E. Silbert, A. J. Liu, and S. R. Nagel. “Jamming at zero temperature and zero applied stress: The epitome of disorder”. In: *Physical Review E* 68 (2003), p. 011306 (cited on pages 14, 16, 18, 48, 49).

[124] S. S. Ashwin, J. Blawzdziewicz, C. S. O’Hern, and M. D. Shattuck. “Calculations of the structure of basin volumes for mechanically stable packings”. In: *Physical Review E* 85 (2012), p. 061307 (cited on pages 14, 57, 62, 69).

[125] D. Wales. *Energy landscapes: Applications to clusters, biomolecules and glasses*. Cambridge University Press, 2003 (cited on pages 14, 20, 72, 125).

[126] A. J. Ballard, S. Martiniani, J. D. Stevenson, S. Somani, and D. J. Wales. “Exploiting the potential energy landscape to sample free energy”. In: *Wiley Interdisciplinary Reviews: Computational Molecular Science* 5.3 (2015), p. 273 (cited on page 14).

[127] R. J. Speedy. “Constrained simulations to count the glasses that a fluid samples”. In: *Journal of Molecular Structure* 485-486 (1999), p. 537 (cited on pages 16, 17).

[128] D. J. Wales. “Surveying a complex potential energy landscape: Overcoming broken ergodicity using basin-sampling”. In: *Chemical Physics Letters* 584 (2013), p. 1 (cited on page 16).

[129] A. Donev, S. Torquato, F. H. Stillinger, and R. Connelly. “Comment on “Jamming at zero temperature and zero applied stress: The epitome of disorder””. In: *Physical Review E* 70.4 (2004), p. 043301 (cited on page 16).

[130] C. S. O’Hern, L. E. Silbert, A. J. Liu, and S. R. Nagel. “Reply to “Comment on ‘Jamming at zero temperature and zero applied stress: The epitome of disorder’””. In: *Physical Review E* 70.4 (2004), p. 043302 (cited on page 16).

[131] F. H. Stillinger and T. A. Weber. “Packing Structures and Transitions in Liquids and Solids”. In: *Science* 225.4666 (1984), p. 983 (cited on pages 17, 18).

[132] F. H. Stillinger and T. A. Weber. “Inherent structure theory of liquids in the hard-sphere limit”. In: *Journal of Chemical Physics* 83.9 (1985), p. 4767 (cited on page 17).

[133] F. H. Stillinger. “A topographic view of supercooled liquids and glass formation”. In: *Science* 267.5206 (1995), p. 1935 (cited on page 17).

[134] B. D. Lubachevsky, F. H. Stillinger, and E. N. Pinson. “Disks vs. spheres: Contrasting properties of random packings”. In: *Journal of Statistical Physics* 64 (1991), p. 501 (cited on page 18).

[135] S. Torquato, T. M. Truskett, and P. G. Debenedetti. “Is Random Close Packing of Spheres Well Defined?” In: *Physical Review Letters* 84 (10 2000), p. 2064 (cited on page 18).

[136] F. H. Stillinger and T. A. Weber. “Hidden structure in liquids”. In: *Physical Review A* 25 (2 1982), p. 978 (cited on page 18).

[137] S. Martiniani, J. D. Stevenson, and K. J. Schrenk. *Monte Carlo Python Energy Landscape Explorer*. https://github.com/pele-python/mcpele. 2014 (cited on pages 18, 20, 23, 40).

[138] J. D. Weeks, D. Chandler, and H. C. Andersen. “Role of Repulsive Forces in Determining the Equilibrium Structure of Simple Liquids”. In: *Journal of Chemical Physics* 54.12 (1971), p. 5237 (cited on page 18).

[139] M. P. Allen and D. J. Tildesley. *Computer simulation of liquids*. Oxford university press, 1989 (cited on page 20).

[140] J. D. Stevenson, V. Rühle, S. Martiniani, and K. J. Schrenk. *Python Energy Landscape Explorer*. https://github.com/pele-python/pele. 2012 (cited on pages 20, 23, 40).

[141] W. W. Hager and H. Zhang. “A new conjugate gradient method with guaranteed descent and an efficient line search”. In: *SIAM Journal on Optimization* 16.1 (2005), p. 170 (cited on pages 20, 63).

[142] W. W. Hager and H. Zhang. “Algorithm 851: CG_DESCENT, a conjugate gradient method with guaranteed descent”. In: *ACM Transactions on Mathematical Software* 32.1 (2006), p. 113 (cited on pages 20, 63).

[143] S. Martiniani. *PyCG_DESCENT*. https://github.com/smcantab/PyCG_DESCENT. 2015 (cited on pages 20, 23, 63).

[144] E. Bitzek, P. Koskinen, F. Gähler, M. Moseler, and P. Gumbsch. “Structural relaxation made simple”. In: *Physical Review Letters* 97.17 (2006), p. 170201 (cited on pages 20, 39).

[145] P. G. Mezey. “Topology of energy hypersurfaces”. In: *Theoretica chimica acta* 62.2 (1982), p. 133 (cited on page 20).

[146] D. Frenkel and A. J. C. Ladd. “New Monte Carlo method to compute the free energy of arbitrary solids. Application to the fcc and hcp phases of hard spheres”. In: *Journal of Chemical Physics* 81.7 (1984), p. 3188 (cited on pages 20, 21, 56, 57, 69, 129).

[147] J. M. Polson, E Trizac, S Pronk, and D Frenkel. “Finite-size corrections to the free energies of crystalline solids”. In: *Journal of Chemical Physics* 112.12 (2000), p. 5339 (cited on pages 20, 21, 128).

[148] A. P. Lyubartsev, A. A. Martsinovski, S. V. Shevkunov, and P. N. Vorontsov-Velyaminov. “New approach to Monte Carlo calculation of the free energy: Method of expanded ensembles”. In: *Journal of Chemical Physics* 96.3 (1992), p. 1776 (cited on pages 20, 96).

[149] E. Marinari and G. Parisi. “Simulated tempering: a new Monte Carlo scheme”. In: *Europhysics Letters* 19.6 (1992), p. 451 (cited on pages 20, 96).

[150] C. J. Geyer and E. A. Thompson. “Annealing Markov chain Monte Carlo with applications to ancestral inference”. In: *Journal of the American Statistical Association* 90.431 (1995), p. 909 (cited on page 20).

[151] D. Frenkel and B. Smit. *Understanding molecular simulation*. San Diego: Academic Press, 2002 (cited on pages 20, 21, 56, 72, 90, 128, 129, 135).

[152] E. M. Knorr and R. T. Ng. “Algorithms for Mining Distance-Based Outliers in Large Datasets”. In: *Proceedings of the 24rd International Conference on Very Large Data Bases*. Morgan Kaufmann Publishers Inc. 1998, p. 392 (cited on pages 25, 41, 140).

[153] M. K. Varanasi and B. Aazhang. “Parametric generalized Gaussian density estimation”. In: *The Journal of the Acoustical Society of America* 86.4 (1989), pp. 1404–1415 (cited on pages 34, 139).

[154] S. Nadarajah. “A generalized normal distribution”. In: *Journal of Applied Statistics* 32.7 (2005), pp. 685–694 (cited on pages 34, 43, 139).

[155] S. Martiniani, K. J. Schrenk, K. Ramola, B. Chakraborty, and D. Frenkel. “Are some packings more equal than others? A direct test of the Edwards conjecture”. In: *arXiv preprint arXiv:1610.06328* (2016) (cited on pages 37, 96).

[156] R. B. Laughlin. *A different universe: Reinventing physics from the bottom down*. Basic Books, 2006 (cited on page 37).

[157] A. Baule, F. Morone, C. S. O’Hern, and H. A. Makse. “Edwards Statistical Mechanics for Jammed Granular Matter”. In: *arXiv preprint arXiv:1602.04369* (2016) (cited on page 38).

[158] P. Olsson and S. Teitel. “Critical scaling of shear viscosity at the jamming transition”. In: *Physical review letters* 99.17 (2007), p. 178001 (cited on page 38).

[159] M. Wyart, S. R. Nagel, and T. Witten. “Geometric origin of excess low-frequency vibrational modes in weakly connected amorphous solids”. In: *EPL (Europhysics Letters)* 72.3 (2005), p. 486 (cited on page 38).

[160] L. E. Silbert, A. J. Liu, and S. R. Nagel. “Structural signatures of the unjamming transition at zero temperature”. In: *Physical Review E* 73.4 (2006), p. 041304 (cited on page 38).

[161] C. P. Goodrich, A. J. Liu, and J. P. Sethna. “Scaling ansatz for the jamming transition”. In: *Proceedings of the National Academy of Sciences* 113.35 (2016), pp. 9745–9750 (cited on pages 38, 47).

[162] K. Ramola and B. Chakraborty. “Disordered Contact Networks in Jammed Packings of Frictionless Disks”. In: *arXiv preprint arXiv:1604.06148* (2016) (cited on page 38).

[163] K. Ramola and B. Chakraborty. “Scaling Theory for the Frictionless Unjamming Transition”. In: *arXiv preprint arXiv:1609.07054* (2016) (cited on page 38).

[164] C. P. Goodrich, A. J. Liu, and S. R. Nagel. “Finite-size scaling at the jamming transition”. In: *Physical review letters* 109.9 (2012), p. 095704 (cited on pages 39, 64).

[165] E. Lebigot. “Uncertainties: a Python package for calculations with uncertainties”. In: *URL http://pythonhosted. org/uncertainties* (2013) (cited on page 40).

[166] B. Efron. “Bootstrap methods: another look at the jackknife”. In: *The Annals of Statistics* 7.1 (1979), pp. 1–26 (cited on pages 40, 43, 79).

[167] B. Efron. “Better bootstrap confidence intervals”. In: *Journal of the American statistical Association* 82.397 (1987), pp. 171–185 (cited on pages 40, 46, 51).

[168] C. Evans. *SciKits-bootstrap*. 2014 (cited on page 40).

[169] D. Asenjo, J. D. Stevenson, D. J. Wales, and D. Frenkel. “Visualizing Basins of Attraction for Different Minimization Algorithms”. In: *Journal of Physical Chemistry B* 117.42 (2013), p. 12717 (cited on pages 43, 62).

[170] D. P. Bertsekas and J. N. Tsitsiklis. *Introduction to probability*. Vol. 1. Athena Scientific Belmont, MA, 2002 (cited on pages 43, 137).

[171] P. J. Steinhardt, D. R. Nelson, and M. Ronchetti. “Bond-orientational order in liquids and glasses”. In: *Physical Review B* 28.2 (1983), p. 784 (cited on pages 47, 64).

[172] D. Vågberg, D. Valdez-Balderas, M. Moore, P. Olsson, and S. Teitel. “Finite-size scaling at the jamming transition: Corrections to scaling and the correlation-length critical exponent”. In: *Physical Review E* 83.3 (2011), p. 030303 (cited on pages 48–50).

[173] C. S. O’Hern, S. A. Langer, A. J. Liu, and S. R. Nagel. “Random packings of frictionless particles”. In: *Physical Review Letters* 88.7 (2002), p. 075507 (cited on page 48).

[174] G. Lois, J Zhang, T. Majmudar, S Henkes, B Chakraborty, C. O’Hern, and R. Behringer. “Stress correlations in granular materials: An entropic formulation”. In: *Physical Review E* 80.6 (2009), p. 060303 (cited on pages 50, 144).

[175] B. P. Tighe. *Force distributions and stress response in granular materials*. 2006 (cited on pages 50, 144).

[176] K. Ball. “An elementary introduction to modern convex geometry”. In: *Flavors of geometry* 31 (1997), pp. 1–58 (cited on pages 56, 63).

[177] M. Simonovits. “How to compute the volume in high dimension?” In: *Mathematical programming* 97.1-2 (2003), pp. 337–374 (cited on pages 56–58).

[178] M. E. Dyer and A. M. Frieze. “On the complexity of computing the volume of a polyhedron”. In: *SIAM Journal on Computing* 17.5 (1988), pp. 967–974 (cited on page 56).

[179] L. G. Khachiyan. “The problem of computing the volume of polytopes is NP-hard”. In: *Uspekhi Mat. Nauk* 44.3 (1989), pp. 199–200 (cited on page 56).

[180] L. G. Khachiyan. “On the complexity of computing the volume of a polytope”. In: *Izvestia Akad. Nauk SSSR, Engineering Cybernetics* 3 (1988), pp. 216–217 (cited on page 56).

[181] C. M. Bishop. *Pattern recognition and machine learning*. New York: Springer, 2009 (cited on pages 56, 61, 64, 140).

[182] J. G. Kirkwood. “Statistical Mechanics of Fluid Mixtures”. In: *Journal of Chemical Physics* 3.5 (1935), p. 300 (cited on page 56).

[183] A. Gelman and X.-L. Meng. “Simulating normalizing constants: From importance sampling to bridge sampling to path sampling”. In: *Statistical Science* 13 (1998), pp. 163–185 (cited on page 56).

[184] F. Wang and D. P. Landau. “Efficient, Multiple-Range Random Walk Algorithm to Calculate the Density of States”. In: *Physical Review Letters* 86 (10 2001), pp. 2050–2053 (cited on page 56).

[185] M. Habeck. “Evaluation of marginal likelihoods via the density of states”. In: *International Conference on Artificial Intelligence and Statistics*. 2012, pp. 486–494 (cited on page 56).

[186] J. Skilling. “Nested sampling”. In: *AIP Conf. Proc. Bayesian inference and maximum entropy methods in science and engineering* 735 (2004), pp. 395–405 (cited on page 56).

[187] S. Martiniani, J. D. Stevenson, D. J. Wales, and D. Frenkel. “Superposition Enhanced Nested Sampling”. In: *Physical Review X* 4 (3 2014), p. 031034 (cited on page 56).

[188] M. R. Shirts and J. D. Chodera. “Statistically optimal analysis of samples from multiple equilibrium states”. In: *The Journal of chemical physics* 129.12 (2008), p. 124105 (cited on pages 56, 58–60, 98).

[189] S. Liu, J. Zhang, and B. Zhu. “Volume Computation Using a Direct Monte Carlo Method”. In: *Computing and Combinatorics*. Ed. by G. Lin. Vol. 4598. Lecture Notes in Computer Science. Springer Berlin Heidelberg, 2007, pp. 198–209 (cited on page 57).

[190] J. D. Chodera, M. R. Shirts, and K. A. Beauchamp. *Python implementation of the multistate Bennett acceptance ratio (MBAR)*. https://github.com/choderalab/pymbar. 2008 (cited on page 60).

[191] N. Xu, V. Vitelli, A. J. Liu, and S. R. Nagel. “Anharmonic and quasi-localized vibrations in jammed solids —Modes for mechanical failure”. In: *EPL* 90.5 (2010), p. 56001 (cited on page 62).

[192] V. Milman. “Surprising geometric phenomena in high-dimensional convexity theory”. In: *European Congress of Mathematics*. Basel: Birkhäuser, 1998, pp. 73–91 (cited on page 63).

[193] V. Guruswami and R. Kannan. *Computer Science Theory for the Information Age*. https://www.cs.cmu.edu/~venkatg/teaching/CStheory-infoage/. 2012 (cited on page 63).

[194] J. van Meel, L Filion, C Valeriani, and D Frenkel. “A parameter-free, solid-angle based, nearest-neighbor algorithm”. In: *The Journal of Chemical Physics* 136.23, 234107 (2012) (cited on page 64).

[195] J. Rudnick and G. Gaspari. “The shapes of random walks”. In: *Science* 237.4813 (1987), pp. 384–389 (cited on page 64).

[196] S.-W. Ye, S. Martiniani, K. J. Schrenk, J. D. Stevenson, D. Frenkel, and E. Vanden-Eijnden. “Density propagation method for surveying energy landscape geometry”. submitted. 2016 (cited on page 71).

[197] R. S. Ellis. *Entropy, large deviations, and statistical mechanics*. Vol. 271. Springer Science & Business Media, 2012 (cited on page 72).

[198] F. H. Stillinger and T. A. Weber. “Dynamics of structural transitions in liquids”. In: *Physical Review A* 28.4 (1983), p. 2408 (cited on page 72).

[199] R. Magnus Jan and H. Neudecker. *Matrix differential calculus with applications in statistics and econometrics*. John Wiley & Sons, New York, 1991 (cited on page 74).

[200] R. Aris. *Vectors, tensors and the basic equations of fluid mechanics*. Courier Corporation, 2012 (cited on page 74).

[201] T. Petrila and D. Trif. *Basics of fluid mechanics and introduction to computational fluid dynamics*. Vol. 3. Springer Science & Business Media, 2004 (cited on page 74).

[202] M. Kantardzic. *Data mining: concepts, models, methods, and algorithms*. John Wiley & Sons, 2011 (cited on page 78).

[203] D. Mehta, C. Hughes, M. Schröck, and D. J. Wales. "Potential energy landscapes for the 2D XY model: Minima, transition states, and pathways". In: *The Journal of chemical physics* 139.19 (2013), p. 194503 (cited on page 83).

[204] D. Mehta, C. Hughes, M. Kastner, and D. J. Wales. "Potential energy landscape of the two-dimensional XY model: Higher-index stationary points". In: *The Journal of chemical physics* 140.22 (2014), p. 224503 (cited on page 83).

[205] D. J. Wales and J. P. Doye. "Global optimization by basin-hopping and the lowest energy structures of Lennard-Jones clusters containing up to 110 atoms". In: *The Journal of Physical Chemistry A* 101.28 (1997), pp. 5111–5116 (cited on page 83).

[206] B. W. Silverman. *Density estimation for statistics and data analysis*. Vol. 26. CRC press, 1986 (cited on page 86).

[207] E. Weinan, W. Ren, and E. Vanden-Eijnden. "String method for the study of rare events". In: *Physical Review B* 66.5 (2002), p. 052301 (cited on page 87).

[208] W. Ren and E. Vanden-Eijnden. "A climbing string method for saddle point search". In: *The Journal of chemical physics* 138.13 (2013), p. 134105 (cited on page 87).

[209] D. Frenkel, K. J. Schrenk, and S. Martiniani. "Monte Carlo sampling for stochastic weight functions". In: *arXiv preprint arXiv:1612.06131* (2016) (cited on page 89).

[210] V. I. Manousiouthakis and M. W. Deem. "Strict detailed balance is unnecessary in Monte Carlo simulation". In: *The Journal of chemical physics* 110.6 (1999), pp. 2753–2756 (cited on page 89).

[211] N. Metropolis, A. W. Rosenbluth, M. N. Rosenbluth, A. H. Teller, and E. Teller. "Equation of state calculations by fast computing machines". In: *Journal of Chemical Physics* 21.6 (1953), pp. 1087–1092 (cited on page 90).

[212] D. Ceperley and M Dewing. "The penalty method for random walks with uncertain energies". In: *The Journal of chemical physics* 110.20 (1999), pp. 9812–9820 (cited on pages 91, 101, 102).

[213] D. Frenkel, G. Mooij, and B. Smit. "Novel scheme to study structural and thermal properties of continuously deformable molecules". In: *Journal of Physics: Condensed Matter* 4.12 (1992), p. 3053 (cited on page 93).

[214] D. Frenkel. "Speed-up of Monte Carlo simulations by sampling of rejected states". In: *Proceedings of the National Academy of Sciences of the United States of America* 101.51 (2004), pp. 17571–17575 (cited on pages 96, 97).

[215] Q. Yan and J. J. d. Pablo. "Hyper-parallel tempering Monte Carlo: Application to the Lennard-Jones fluid and the restricted primitive model". In: *Journal of Chemical Physics* 111.21 (1999), p. 9509 (cited on pages 96, 132).

[216] A. Bunker and B. Dünweg. “Parallel excluded volume tempering for polymer melts”. In: *Physical Review E* 63.1 (2000), p. 016701 (cited on pages 96, 132).

[217] H. Fukunishi, O. Watanabe, and S. Takada. “On the Hamiltonian replica exchange method for efficient sampling of biomolecular systems: Application to protein structure prediction”. In: *The Journal of chemical physics* 116.20 (2002), pp. 9058–9067 (cited on page 96).

[218] A. Barker. “Monte carlo calculations of the radial distribution functions for a proton? electron plasma”. In: *Australian Journal of Physics* 18.2 (1965), pp. 119–134 (cited on page 97).

[219] S. Franz and G. Parisi. “The simplest model of jamming”. In: *Journal of Physics A: Mathematical and Theoretical* 49.14 (2016), p. 145001 (cited on page 105).

[220] L. Corte, P. Chaikin, J. P. Gollub, and D. Pine. “Random organization in periodically driven systems”. In: *Nature Physics* 4.5 (2008), pp. 420–424 (cited on page 105).

[221] D. Hexner and D. Levine. “Hyperuniformity of critical absorbing states”. In: *Physical review letters* 114.11 (2015), p. 110602 (cited on page 105).

[222] S. Torquato and F. H. Stillinger. “Local density fluctuations, hyperuniformity, and order metrics”. In: *Physical Review E* 68.4 (2003), p. 041113 (cited on page 106).

[223] A. Donev, F. H. Stillinger, and S. Torquato. “Unexpected density fluctuations in jammed disordered sphere packings”. In: *Physical review letters* 95.9 (2005), p. 090604 (cited on page 106).

[224] T. Hull and W. Luxemburg. “Numerical methods and existence theorems for ordinary differential equations”. In: *Numerische Mathematik* 2.1 (1960), pp. 30–41 (cited on page 123).

[225] C. Vega, E. Sanz, J. L. F. Abascal, and E. G. Noya. “Determination of phase diagrams via computer simulation: methodology and applications to water, electrolytes and proteins”. In: *Journal of Physics: Condensed Matter* 20.15 (2008), p. 153101 (cited on page 128).

[226] E. W. Weisstein. *Lobatto Quadrature – from Wolfram MathWorld*. http://mathworld.wolfram.com/LobattoQuadrature.html. 2016 (cited on pages 130, 132).

[227] E. Jones, T. Oliphant, P. Peterson, et al. *SciPy: Open source scientific tools for Python*. 2001– (cited on page 132).

[228] H. Fukunishi, O. Watanabe, and S. Takada. “On the Hamiltonian replica exchange method for efficient sampling of biomolecular systems: Application to protein structure prediction”. In: *Journal of Chemical Physics* 116.20 (2002), p. 9058 (cited on page 132).

[229] A. Santos, S. B. Yuste, and M. L. De Haro. “Equation of state of a multicomponent d-dimensional hard-sphere fluid”. In: *Molecular Physics* 96.1 (1999), p. 1 (cited on pages 135, 136).

[230] E. W. Weisstein. *Jensen’s inequality. From MathWorld–A Wolfram Web Resource*. 2016 (cited on page 137).

[231] B. Singh, K. K. Sharma, S. Rathi, and G. Singh. “A generalized log-normal distribution and its goodness of fit to censored data”. In: *Computational Statistics* 27.1 (2012), p. 51 (cited on page 140).

[232] F. Pedregosa et al. “Scikit-learn: Machine learning in Python”. In: *Journal of Machine Learning Research* 12.Oct (2011), pp. 2825–2830 (cited on pages 140, 141).

[233] A. W. Bowman. “An alternative method of cross-validation for the smoothing of density estimates”. In: *Biometrika* 71.2 (1984), p. 353 (cited on page 140).

[234] P. J. Rousseeuw and K. V. Driessen. “A fast algorithm for the minimum covariance determinant estimator”. In: *Technometrics* 41.3 (1999), pp. 212–223 (cited on page 141).

[235] M. Hubert and M. Debruyne. “Minimum covariance determinant”. In: *Wiley interdisciplinary reviews: Computational statistics* 2.1 (2010), pp. 36–43 (cited on page 141).

[236] T. Popoviciu. “Sur les équations algébriques ayant toutes leurs racines réelles”. In: *Mathematica* 9 (1935), pp. 129–145 (cited on page 144).

Appendix A

Paths of steepest descent

A path of steepest descent is a curve in the $dN-$dimensional configuration space that follows the gradient of the potential. We can parametrise this path with respect to the path length s, such that $|\mathrm{d}\boldsymbol{x}_s/\mathrm{d}s| = 1$. The arc-length along the path connecting $\boldsymbol{x}_{s'}$ to $\boldsymbol{x}_{s''}$ is therefore $|s'' - s'|$. This results follows immediately from the integral defining the path length:

$$\int_{s'}^{s''} \left| \frac{\mathrm{d}\boldsymbol{x}_s}{\mathrm{d}s} \right| \mathrm{d}s = \int_{s'}^{s''} \mathrm{d}s = s'' - s' \tag{A.1}$$

Requiring that the tangent vector to the path is anti-parallel to the gradient (the potential decreases as s increases), by definition $\boldsymbol{x}_s$ satisfies:

$$\frac{\mathrm{d}\boldsymbol{x}_s}{\mathrm{d}s} = -\frac{\nabla U(\boldsymbol{x}_s)}{|\nabla U(\boldsymbol{x}_s)|} \tag{A.2}$$

where $|\nabla U(\boldsymbol{x}_s)|$ is the norm of the gradient vector. Eq. (A.2) is short hand for a system of dN first-order differential equations

$$\frac{\mathrm{d}\boldsymbol{x}_i}{\mathrm{d}s} = -\frac{\mathrm{d}U(\boldsymbol{x})}{\mathrm{d}x_i}; \;\; i = 1, \ldots, dN. \tag{A.3}$$

Requiring a solution for this set of first order differential equation amounts to a Cauchy problem and proof of the uniqueness of its solution for Lipschitz continuous functions is provided by the Cauchy-Lipschitz theorem [224]. Hence for the subset of points such that $\nabla U(\boldsymbol{x}) \neq 0$, there exist a unique solution to Eq. (A.2). In other words, a path of steepest descent is unique until it does not meet a stationary point since, in general, there are many solutions terminating at a stationary point. If $\boldsymbol{x}_0$ is a simple saddle point, then there are only two solutions starting from $\boldsymbol{x}_0$ along which the energy decreases.

This behaviour of the solutions to Eq. (A.2) can be easily verified in the neighbourhood of a stationary point $\boldsymbol{x}_0$. By aligning our dN Cartesian coordinates with the principal directions of curvature (orthogonal transformation to normal mode coordinates) and Taylor expanding $U(\boldsymbol{x})$ around this stationary point, we write:

$$U(\boldsymbol{x}_0+\Delta\boldsymbol{x}) = U(\boldsymbol{x}_0) + \sum_i^{dN} \frac{1}{2}\lambda_i \Delta x_i^2 \tag{A.4}$$

where λ_i is the i-th Hessian eigenvalue. The solution to Eq. (A.2) is then given by the linear system:

$$\frac{\mathrm{d}x_i'}{\mathrm{d}t} = -\lambda_i x_i', \tag{A.5}$$

where we made a change of variables to $\boldsymbol{x}'$ to drop the factor $|\nabla U(\boldsymbol{x})|$; note however that $\boldsymbol{x}(s) = \boldsymbol{x}'(t)$ if $\boldsymbol{x}(s_0) = \boldsymbol{x}'(t_0)$. Solution to Eq. (A.5) is then of the form:

$$x_i'(t) = x'(0)e^{-\lambda_i t}. \tag{A.6}$$

Now suppose that the path of steepest descent starting at $\boldsymbol{x}(0)$ leads to a simple saddle at $\boldsymbol{x}_0$ with only negative eigenvalue $\lambda_1 < 0$. Since the steepest descent path is now parametrised by t, such that $\mathrm{d}t = \mathrm{d}s/|\nabla U(\boldsymbol{x})|$ and $|\nabla U(\boldsymbol{x})| = 0$ at a stationary point, then we must consider the limits $t \to \pm\infty$. There are only two curves reaching the stationary point as $t \to -\infty$, $x_i'(t) = 0$ for all $i \neq 1$ and $x_1'(0)$ either positive or negative. For $t \to +\infty$, an infinite number of steepest descent paths with $x_1'(t) = 0$ approach the saddle, and therefore the potential cannot decrease along this curve as it moves away from $\boldsymbol{x}_0$ (these paths lie in the hyperplane perpendicular to the coordinate x_1'). Therefore, as anticipated, there are only two steepest descent paths leading down in energy from the saddle: they are parallel to the eigenvector associated with the only negative eigenvalue and anti-parallel to each other.

Particular care needs to be taken when saddle points have additional zero eigenvalues other than the ones corresponding to overall translation and rotation of the system. Consider for example the two dimensional surface:

$$U(x,y) = -\alpha x^2 - \beta y^2; \;\; \alpha,\beta > 0. \tag{A.7}$$

The origin $(0,0)$ is a stationary point with Hessian eigenvalues -2α and 0, but the energy is not invariant along this additional zero eigenvector as for overall translation and rotation. By solving the linear system of differential equations for the steepest descent paths, Eq. (A.2), one finds that an infinite number of paths of steepest descent approach the origin as $t \to -\infty$

and an additional one for $t \to +\infty$ along the negative axis [125]. A stationary point with an additional zero eigenvalue is known as a “degenerate” or “non-Morse” point.

Appendix B

Volume computation by the Einstein crystal method

B.1 Einstein crystal

The harmonic potential is defined as follows:

$$U_{\text{har}}(\mathbf{x}|\mathbf{x}_0,k) = \frac{k}{2}|\mathbf{x}-\mathbf{x}_0|^2 = \frac{k}{2}\sum_{i}^{N}|\mathbf{x}_i-\mathbf{x}_{i,0}|^2 \tag{B.1}$$

where $\mathbf{x}_0$ denotes the equilibrium position, the index i denotes the i-th of N particles, each with d degrees of freedom, and we have assumed that the spring constant k is the same for all directions of motion. We can compute the mean squared particle displacement for a harmonic oscillator in the canonical ensemble analytically. We start with the partition function:

$$Z_{NVT} = \left(\frac{2\pi}{\beta k}\right)^{\frac{dN}{2}}. \tag{B.2}$$

We consider the free energy for the system $F = -\beta^{-1}\ln Z$ and observe that

$$\begin{aligned}\left(\frac{\partial F(k)}{\partial k}\right)_{NVT} &= -\beta^{-1}\frac{\partial}{\partial k}\ln Z = -(\beta Z)^{-1}\frac{\partial Z}{\partial k}\\ &= \frac{\int_{-\infty}^{\infty}\mathrm{d}\mathbf{x}^{dN}\frac{1}{2}|\mathbf{x}-\mathbf{x}_0|^2 e^{-\beta k|\mathbf{x}-\mathbf{x}_0|^2/2}}{\int_{-\infty}^{\infty}\mathrm{d}\mathbf{x}^{dN} e^{-\beta k|\mathbf{x}-\mathbf{x}_0|^2/2}}\\ &= \frac{1}{2}\langle|\mathbf{x}-\mathbf{x}_0|^2\rangle_k,\end{aligned} \tag{B.3}$$

hence we can compute the mean squared distance for a dN-dimensional harmonic oscillator

$$\langle|\mathbf{x}-\mathbf{x}_0|^2\rangle_k = 2\left(\frac{\partial F(k)}{\partial k}\right)_{NVT} = \frac{dN}{\beta k}. \tag{B.4}$$

For thermodynamic integration we are interested in the limit $k \to 0$. In this limit there is no penalty for moving the system as whole, hence the mean squared displacement becomes of the order of L^2, where L is the box side length. This result means that the function $\langle|\mathbf{x}-\mathbf{x}_0|^2\rangle_k$ will be strongly peaked at $k = 0$, thus making its integration difficult. For this reason, we would like this function to vary slowly with k. This behaviour can be achieved by fixing the centre of mass of the system, so that drifting as a whole is forbidden [151].

The centre of mass is defined as:

$$\mathbf{x}_{\mathrm{CM}} = \sum_i \mu_i \mathbf{x}_i, \quad \text{where } \mu_i = \frac{m_i}{\sum_i m_i}. \tag{B.5}$$

When computing the potential energy for the harmonic spring, we must apply the following correction:

$$|\mathbf{x}^{(C)} - \mathbf{x}_0^{(C)}|^2 = \sum_i^N |\mathbf{x}_i^{(U)} - \mathbf{x}_{i,0}^{(U)} - \Delta\mathbf{x}_i^{(\mathrm{CM})}|^2, \tag{B.6}$$

where i is the index for the i-th particle and C and U denote the corrected and the uncorrected coordinates respectively. The configurational partition function requires a correction, hence we define the corrected partition function Z_{CM} with centre of mass fixed at $\mathbf{x}_{\mathrm{CM}} = \mathbf{0}$ and note that:

$$\begin{aligned} Z_{\mathrm{CM}} &= \int_{-\infty}^{\infty} \mathrm{d}\mathbf{x}^{dN} e^{-\beta k|\mathbf{x}-\mathbf{x}_0|^2/2} \delta\left(\sum_i \mu_i \mathbf{x_i}\right) \\ &= \left(\frac{\beta k}{2\pi \sum_i \mu_i^2}\right)^{d/2} \left(\frac{2\pi}{\beta k}\right)^{Nd/2} = \left(\frac{\beta k}{2\pi \sum_i \mu_i^2}\right)^{d/2} Z, \end{aligned} \tag{B.7}$$

where solution of the integral was obtained after a fair amount of algebra by rewriting the Dirac delta as the Fourier sum $\delta(\mathbf{x}) = 1/(2\pi^3) \int \mathrm{d}\mathbf{k} \exp(i\mathbf{k}\mathbf{x})$ [147, 225].

Using Eq. (B.4) we find the mean squared displacement for the constrained Harmonic oscillator:

$$\langle|\mathbf{x}-\mathbf{x}_0|^2\rangle_{\mathrm{CM}} = 2\left(\frac{\partial F^{\mathrm{CM}}(k)}{\partial k}\right)_{NVT} = \frac{(N-1)d}{\beta k}. \tag{B.8}$$

This result can be interpreted as the mean squared displacement of the $(N-1)d$ harmonic oscillator: fixing the centre of mass is equivalent to fixing one particle and integrating Eq. (B.7) over the remaining degrees of freedom by doing the change of variables $\mathbf{x}_i' = \mathbf{x}_i - \mathbf{x}_N$ (conveniently with unit Jacobian) if the N-th particle is fixed.

To conclude, let us relabel the potential as

$$U(\mathbf{x}|\mathbf{x}_0,k,\lambda) = (1-\lambda)\Phi(\mathbf{x}) + \frac{1}{2}\lambda k|\mathbf{x}-\mathbf{x}_0|^2, \tag{B.9}$$

where $\Phi(\mathbf{x})$ is an arbitrary field, it could be, for instance, an additional inter-atomic interaction independent of k or, even the zero field. Let us consider the limit $\lambda \to 0$: from the ratio of the partition functions for the constrained and unconstrained centre of mass, we find:

$$\begin{aligned}\frac{Z_{\text{CM}}(\lambda=0)}{Z(\lambda=0)} &= \frac{\displaystyle\int_{-\infty}^{\infty} \mathrm{d}\mathbf{x}^{dN} e^{-\beta\Phi(\mathbf{x})}\,\delta(\sum_i \mu_i \mathbf{x}_\mathbf{i})}{\displaystyle\int_{-\infty}^{\infty} \mathrm{d}\mathbf{x}^{dN} e^{-\beta\Phi(\mathbf{x})}} \\ &= \left\langle \delta\left(\sum_i \mu_i \mathbf{x}_i\right)\right\rangle = \mathcal{P}(\mathbf{x}_{\text{CM}} = \mathbf{0}),\end{aligned} \tag{B.10}$$

where δ is the Dirac delta function and $\mathcal{P}(\mathbf{x}_{\text{CM}} = 0)$ is the probability density of the centre of mass being at $\mathbf{0}$ when $\lambda = 0$. Hence we write:

$$Z_{\text{CM}}(\lambda=0) = Z(\lambda=0)\mathcal{P}(\mathbf{x}_{\text{CM}} = 0) \tag{B.11}$$

where $\mathcal{P}$ depends on the details of the system. If the equilibrium structure is invariant to translations, a condition that holds true in a system with periodic boundary conditions, then we can take $\mathcal{P} = 1/V_{\text{cell}}$, where V_{cell} is the smallest repeating unit in the periodic system (unit cell). This is at worst $V_{\text{cell}} = V_{\text{box}}$, while for a fcc Einstein crystal it would correspond to the Wigner-Seitz cell $V_{cell} = V_{box}/N$ [146].

B.2 Free energy calculation for solids

To compute the free energy of a system with discontinuous potential energy function (e.g., hard disks or hard spheres), we construct a reversible path to the corresponding Einstein solid (see e.g. [151]). The harmonic potential with spring constant k is switched on while maintaining the hard core interactions intact:

$$\begin{aligned}U(\mathbf{x}|\mathbf{x}_0,k) &= U_{\text{HS}}(\mathbf{x}) + U_{\text{har}}(\mathbf{x}|\mathbf{x}_0,k) \\ &= U_{\text{HS}}(\mathbf{x}) + \frac{1}{2}k|\mathbf{x}-\mathbf{x}_0|^2,\end{aligned} \tag{B.12}$$

where $\mathbf{x}_0$ are the equilibrium coordinates of the Einstein crystal and $U_{\mathrm{HS}}(\mathbf{x})$ denotes the hard core interactions. Since the reciprocal temperature β and the coupling constant k always appear in a product, changing β would simply renormalise the range of k's. In what follows, we shall assume $\beta = 1$ everywhere without loss of generality (hence, in this case, one can think of thermodynamic integration as a "k integration"). We can then compute the free energy difference between the Einstein crystal and the hard core system by evaluating the integral:

$$\begin{aligned} F_{\mathrm{HS}} &= F_{\mathrm{har}}(k_{\max}) + \Delta F \\ &\equiv F_{\mathrm{har}}(k_{\max}) - \int_0^{k_{\max}} \mathrm{d}k \left\langle \frac{\partial U(\mathbf{x}|\mathbf{x}_0, k)}{\partial k} \right\rangle_k . \end{aligned} \tag{B.13}$$

As discussed in Appendix B.1, we take the centre of mass to be fixed to avoid numerical issues in the limit $k \to 0$. For a system with fixed centre of mass, we write the free energy difference between the target and the reference state as

$$\Delta F^{(\mathrm{CM})} \equiv F^{(\mathrm{CM})} - F^{(\mathrm{CM})}_{\mathrm{har}} . \tag{B.14}$$

From the partition function of the Einstein crystal with fixed centre of mass, Eq. (B.7), and for the unconstrained crystal, Eq. (B.11), we can rewrite Eq. (B.14) and rearrange it for the free energy of the unconstrained crystal:

$$\begin{aligned} F = {} & \Delta F^{(\mathrm{CM})} + \ln\left(\mathcal{P}(\mathbf{x}_{\mathrm{CM}} = \mathbf{0})\right) \\ & + \frac{d}{2} \ln\left(\frac{2\pi \sum_i \mu_i}{k_{\max}}\right) - \frac{Nd}{2} \ln\left(\frac{2\pi}{k_{\max}}\right), \end{aligned} \tag{B.15}$$

where the last term is F_{har} and the second and third terms on the right hand side are the CM corrections for the unconstrained and the constrained solid, respectively. For a system with unit cell identical to the simulation box (with periodic boundary conditions), we have $\mathcal{P}(\mathbf{x}_{\mathrm{CM}} = \mathbf{0}) = 1/V_{\mathrm{box}}$. Assuming that all particles have unit mass we can rewrite Eq. (B.15) as

$$F = \Delta F^{(\mathrm{CM})} - \ln\left(V_{\mathrm{box}}\right) - \frac{(N-1)d}{2} \ln\left(\frac{2\pi}{k_{\max}}\right). \tag{B.16}$$

We are only left with $\Delta F^{(\mathrm{CM})}$, which can be found by evaluating the integral in Eq. (B.13). In order to do so, we would like the integrand to be a well behaved function, possibly flat, permitting Gauss-Lobatto (GL) quadrature [226]. We transform the integration variable so that

$$\begin{aligned}\Delta F^{(\mathrm{CM})} &= \int_0^{k_{\max}} \frac{\mathrm{d}k}{g(k)} g(k) \frac{1}{2} \left\langle |\mathbf{x}-\mathbf{x}_0|^2 \right\rangle_k^{(\mathrm{CM})} \\ &= \int_{G^{-1}(0)}^{G^{-1}(k_{\max})} \mathrm{d}\left[G^{-1}(k)\right] g(k) \frac{1}{2} \left\langle |\mathbf{x}-\mathbf{x}_0|^2 \right\rangle_k^{(\mathrm{CM})} ,\end{aligned} \tag{B.17}$$

where $g(k)$ is some function of k and $G^{-1}(k)$ is the primitive of the function $1/g(k)$.

To choose an appropriate $g(k)$, we note that in Eq. (B.8) for very large k the mean squared displacement for the solid is

$$\langle |\mathbf{x}-\mathbf{x}_0|^2 \rangle_{k_{\max}} = \frac{(N-1)d}{k_{\max}}. \tag{B.18}$$

For k other than $k_{\max}$, we expect the mean squared displacement to depend on some effective spring constant. Hence we write

$$\left\langle |\mathbf{x}-\mathbf{x}_0|^2 \right\rangle_k \approx \frac{(N-1)d}{(k+\xi)}, \tag{B.19}$$

such that the mean squared displacement at $k=0$ is

$$\left\langle |\mathbf{x}-\mathbf{x}_0|^2 \right\rangle_{k=0} \approx \frac{(N-1)d}{\xi}, \tag{B.20}$$

from which we find $\xi = (N-1)d/\langle |\mathbf{x}-\mathbf{x}_0|^2 \rangle_{k=0}$ [note that we can self consistently replace this definition for ξ in Eq. (B.19) to obtain an approximation for the mean squared displacement at arbitrary k]. We would like the integrand $g(k)\langle |\mathbf{x}-\mathbf{x}_0|^2 \rangle_k$ in Eq. (B.17) to be roughly constant. Given the considerations above we choose $g(k) \approx k+\xi$. One can easily verify that the integrand is now approximately constant. We can then rewrite the integral in Eq. (B.17) as

$$\begin{aligned}\Delta F^{(\mathrm{CM})} = \int_{\ln(\xi)}^{\ln(k_{\max}+\xi)} \Bigg\{ &(k+\xi) \frac{1}{2} \left\langle |\mathbf{x}-\mathbf{x}_0|^2 \right\rangle_k^{(\mathrm{CM})} \\ &\mathrm{d}\left[\ln(k+\xi)\right] \Bigg\}.\end{aligned} \tag{B.21}$$

Finally, to integrate Eq. (B.21) by GL quadrature, we require a variable, t, such that the integral upper and lower bounds are $[-1,1]$:

$$t = \frac{2\ln(1+k/\xi)-1}{\ln(1+k_{\max}/\xi)} \tag{B.22}$$

with differential

$$\mathrm{d}t = \frac{2}{\ln(1+k_{\max}/\xi)}\,\mathrm{d}\left[\ln(1+k/\xi)\right]. \tag{B.23}$$

Therefore we rewrite Eq. (B.21) as a function of t:

$$\begin{aligned}\Delta F^{(\mathrm{CM})} = \int_{-1}^{1} \Bigg\{ \mathrm{d}t \ln\left(1+\frac{k_{\max}}{\xi}\right) \\ [k(t)+\xi]\,\frac{1}{4}\left\langle |\mathbf{x}-\mathbf{x}_0|^2 \right\rangle_k^{(\mathrm{CM})} \Bigg\},\end{aligned} \tag{B.24}$$

where $k(t)$ can be found by rearranging Eq. (B.22). An example of the variable transform is shown in Fig. 2.4.

It is straightforward to perform GL quadrature for a general number of abscissas $n \geq 2$ [226], because

$$\int_{-1}^{1} \mathrm{d}t f(t) = w_1 f(-1) + \sum_{i=2}^{n-1} w_i f(t_i) + w_n f(1), \tag{B.25}$$

where w_i are the weights and t_i are the abscissas. The abscissas different from $-1, 1$ are the $n-2$ roots of $\mathrm{d}P_{n-1}(t)/\mathrm{d}t$, with P_{n-1} a Legendre polynomial. We evaluate this sum numerically using Numpy's Legendre module [227]. The weights w_i can also be evaluated numerically for general $n \geq 2$, since they are related to P_{n-1} evaluated at t_i [226]. Unless specified otherwise, for all results in this work, we choose $n = 16$ abscissas.

B.3 Sampling the integrand: Hamiltonian Parallel Tempering

To compute the integral in Eq. (B.24), we need to measure the integrand for different values of k, as given by Eq. (B.22). Equilibration of the corresponding simulations can be accelerated using extensions of the parallel tempering technique, where replicas differ in chemical potential [215] or in the potential energy function [216, 228].

The Parallel-tempering acceptance rule for a swap of configurations between replicas with different Hamiltonians follows from the condition of detailed balance:

$$\begin{aligned}&\frac{\mathrm{acc}[(\mathbf{x}_i,U_i),(\mathbf{x}_j,U_j)\to(\mathbf{x}_j,U_i),(\mathbf{x}_i,U_j)]}{\mathrm{acc}[(\mathbf{x}_i,U_j),(\mathbf{x}_j,U_i)\to(\mathbf{x}_i,U_i),(\mathbf{x}_j,U_j)]}\\ &=\frac{\exp\{-\beta[U_i(\mathbf{x}_j)+U_j(\mathbf{x}_i)]\}}{\exp\{-\beta[U_i(\mathbf{x}_i)+U_j(\mathbf{x}_j)]\}}\\ &=\exp\left\{-\beta\left[\left(U_i(\mathbf{x}_j)+U_j(\mathbf{x}_i)\right)-\left(U_i(\mathbf{x}_i)+U_j(\mathbf{x}_j)\right)\right]\right\},\end{aligned} \tag{B.26}$$

where acc$[\cdot \to \cdot]$ denotes the swap acceptance probability. For the particular case of replicas coupled to a reference state $\mathbf{x}_0$ by a harmonic potential with different coupling strengths k_i, we find the swap acceptance rule

$$\begin{aligned}&\mathrm{acc}[(\mathbf{x}_i, U_i), (\mathbf{x}_j, U_j) \to (\mathbf{x}_j, U_i), (\mathbf{x}_i, U_j)] \\ &= \min\left\{1, \exp[\frac{\beta}{2}\left[(k_j - k_i)(|\mathbf{x}_j - \mathbf{x}_0|^2 - |\mathbf{x}_i - \mathbf{x}_0|^2)\right]\right\}.\end{aligned} \tag{B.27}$$

Note that the swaps are between replicas at the same temperature β but different coupling strengths k (although it need not be). Furthermore, we choose $\beta = 1$ without loss of generality, as discussed in the previous section. Hamiltonian Parallel Tempering allows to achieve faster equilibration by swapping replicas with large k, that are close to the spherical core of the basin, with replicas with small k, that are entropically driven towards the boundaries of the basin. Hence, the swaps prevent small-k replicas from getting stuck in remote corners of the basin (for a discussion of the complex shape of basins of attraction see Sec. 4.3). To check whether the replicas are well equilibrated, we consider the correlations in the “time series” of $|\mathbf{x} - \mathbf{x}_0|_k$ *vs* number of Monte Carlo steps for each replica.

Appendix C

Polydisperse hard-sphere fluid and total accessible volume

The basins of attraction of energy minima tile the "accessible" phase space (schematically shown in Fig. 3.1b-c). This inaccessible part of the phase space arises due to hard core constraints and the existence of fluid and marginally stable states. We can write the total accessible volume as

$$-\ln \mathcal{V}_J(N,\phi) = -N \ln V_{\text{box}} + N f_{\text{ex}}(\phi) - \ln p_J(\phi_{\text{SS}}), \tag{C.1}$$

where ϕ is the volume fraction, $f_{\text{ex}(\phi)}$ is the excess free energy, which is the difference in free energy between the hard sphere fluid and the ideal gas, and $p_J(\phi_{\text{SS}})$ is the probability of obtaining a jammed packing at soft volume fraction ϕ_{SS} with our protocol (e.g. see Fig. 3.8), which accounts for the coexisting (unjammed or marginally jammed) fluid states. We can then define the probability of sampling the i-th packing as $p_i = v_i/\mathcal{V}_J$, where v_i is the volume of the basin of attraction of the packing. The total number of jammed packings is given by $\Omega = \mathcal{V}_J/\langle v \rangle$, where $\langle v \rangle$ is the unbiased average basin volume.

We can compute the excess free energy by thermodynamic integration [151]. We start by noting that $\partial F/\partial(1/V_{\text{box}}) = V_{\text{box}}^2 P$ and define the number density $\rho = N/V_{\text{box}}$, hence we write

$$f_{\text{ex}}(\rho) = \frac{F(\rho)}{N} - \frac{F^{(\text{id})}(\rho)}{N} = \int_0^\rho \mathrm{d}\rho' \left(\frac{P(\rho') - \rho'}{\rho'^2} \right). \tag{C.2}$$

By noting that the volume fraction of a polydisperse system is $\phi = v_d \rho \langle \sigma^d \rangle$ [229], where v_d is the volume of the d-dimensional unit sphere and $\langle \sigma^d \rangle$ is the d-th moment of the distribution of diameters, we can change variable and write

$$f_{\mathrm{ex}}(\phi) = \frac{F(\phi)}{N} - \frac{F^{(\mathrm{id})}(\phi)}{N} = \int_0^{\phi} \mathrm{d}\phi' \left(\frac{Z(\phi') - 1}{\phi'} \right), \tag{C.3}$$

where $Z(\phi) = P/\rho$ is the compressibility factor (we set $\beta = 1$ everywhere).

Analytical approximations for the compressibility factors for the two and three-dimensional polydisperse hard sphere fluid have been proposed. For the hard disk fluid we use the Santos-Yuste-Haro (eSYH) equation of state [229]

$$\begin{aligned} Z^{\mathrm{poly}}_{\mathrm{eSHY}}(\phi) = {} & \frac{\langle\sigma\rangle^2/\langle\sigma^2\rangle}{1 - 2\phi + (2\phi_0 - 1)\phi^2/\phi_0^2} \\ & + \frac{1}{1-\phi}\left(1 - \frac{\langle\sigma\rangle^2}{\langle\sigma^2\rangle}\right), \end{aligned} \tag{C.4}$$

where $\phi_0 = \pi/\sqrt{12}$ is the crystalline close packing fraction.

For three-dimensional fluids, depending on the volume fraction, we choose two different equations of state. For volume fraction $\phi > 0.5$, Santos *et al.* [229] suggest the following equation of state based on the Carnahan-Startling (CS) equation of state for the monodisperse fluid:

$$\begin{aligned} Z^{\mathrm{poly}}_{\mathrm{eCS}}(\phi) = 1 + {} & \left[\frac{1 + \phi + \phi^2 - \phi^3}{(1-\phi)^3} - 1 \right] \\ & \times \frac{\langle\sigma^2\rangle}{2\langle\sigma^3\rangle^2} \left(\langle\sigma^2\rangle^2 + \langle\sigma\rangle\langle\sigma^3\rangle \right) \\ & + \frac{\phi}{1-\phi} \left[1 - \frac{\langle\sigma^2\rangle}{\langle\sigma^3\rangle}^2 \left(2\langle\sigma^2\rangle^2 - \langle\sigma\rangle\langle\sigma^3\rangle \right) \right]. \end{aligned} \tag{C.5}$$

For volume fractions $\phi \leq 0.5$ the eCSK equation of state should be preferred (based on the Carnahan-Starling-Kolafa equation of state for the monodisperse fluid)

$$\begin{aligned} Z^{\mathrm{poly}}_{\mathrm{eCSK}}(\phi) = {} & Z^{\mathrm{poly}}_{\mathrm{eCS}}(\phi) \\ & + \frac{\phi^3(1-2\phi)}{(1-\phi)^3} \frac{\langle\sigma^2\rangle}{6\langle\sigma^3\rangle^2} \left(\langle\sigma^2\rangle^2 + \langle\sigma\rangle\langle\sigma^3\rangle \right). \end{aligned} \tag{C.6}$$

The excess free energy can thus be obtained by substituting one of Eq. (C.4) to (C.6) in the integral of Eq. (C.3), which can then be evaluated numerically for the desired volume fraction.

Appendix D

Power-law between pressure and basin volume

A power-law relationship between the volume of the basin of attraction of a jammed packing and its pressure was reported in Eq. (2.20). In what follows we provide insight into this expression. We observe that distributions of negative basin log-volumes, $F \equiv -\ln v_{\text{basin}}$, and log-pressures, $\Lambda \equiv \ln P$, are approximately normally distributed (see Fig. 3.2 and 3.5a). We therefore expect their joint probability to be well-approximated by a bivariate Gaussian distribution $\mathcal{B}(\phi;F,\Lambda) = \mathcal{N}(\mu,\hat{\sigma})^1$, with mean $\mu = (\mu_F,\mu_\Lambda)$ and covariance matrix $\hat{\sigma} = ((\sigma_F^2,\sigma_{F\Lambda}^2),(\sigma_{F\Lambda}^2,\sigma_\Lambda^2))$ [170]. This is consistent with the elliptical distribution of points in Figs. 2.6, 3.4. For a given random variable X, with an (observed/biased) marginal distribution $\mathcal{B}(X)$, the mean is given by $\mu_X(\phi) = \langle X\rangle_{\mathcal{B}} = \int X\mathcal{B}(\phi;X)\,\mathrm{d}X$. Similarly, the (biased) conditional expectation of F for a given Λ is [170]

$$\langle F\rangle_{\mathcal{B}(\Psi)}(\phi;\Lambda) \equiv \mathbb{E}[F|\phi;\Lambda] = \frac{\sigma_{F\Lambda}^2(\phi)}{\sigma_\Lambda^2(\phi)}(\Lambda-\mu_\Lambda(\phi))+\mu_F(\phi). \tag{D.1}$$

This is simply the linear minimum mean square error (MMSE) regression estimator for F, *i.e.* the linear estimator $\hat{Y}(X) = aX+b$ that minimizes $\mathbb{E}[(Y-\hat{Y}(X))^2]$. The expectation of the dimensionless free energy $\langle F\rangle_{\mathcal{B}(\Psi)}(\phi;\Lambda) = -\langle \ln v\rangle_{\mathcal{B}(\Psi)}(\phi;\Lambda) \geq -\ln\langle v\rangle_{\mathcal{B}(\Psi)}(\phi;\Lambda)$ [230] is the average basin negative log-volume at volume fraction ϕ and log-pressure Λ. Here the average is also taken over all other relevant, but unknown, order parameters Ψ, such that $\langle F\rangle_{\mathcal{B}(\Psi)}(\phi;\Lambda) = \int \mathrm{d}\Psi\mathcal{B}(\Psi)F(\phi;\Psi,\Lambda)$. In other words, we write the expectation of F at a given pressure as the (biased) average over the unspecified order parameters Ψ. An example of such a parameter would be some topological variable that makes certain topologies more

---

[1] When listing a function's arguments we place parameters that are held constant before the semicolon

probable than others. Note that $F(\phi,\Lambda;\Gamma)$ is narrowly distributed around $\mathbb{E}[F|\phi;\Lambda]$. To simplify the notation we write $\langle F\rangle_{\mathcal{B}(\Psi)}(\phi;\Lambda)\equiv\langle F\rangle_{\mathcal{B}}(\phi;\Lambda)$. We can thus rewrite Eq. (2.20) as

$$\begin{aligned}\langle f\rangle_{\mathcal{B}}(\phi;\Lambda) =&\lambda(\phi)\Lambda+c(\phi)\\ =&\frac{\sigma^2_{f\Lambda}(\phi)}{\sigma^2_{\Lambda}(\phi)}\Lambda-\frac{\sigma^2_{f\Lambda}(\phi)}{\sigma^2_{\Lambda}(\phi)}\mu_{\Lambda}(\phi)+\mu_f(\phi)\\ =&\frac{\sigma^2_{f\Lambda}(\phi)}{\sigma^2_{\Lambda}(\phi)}\Delta\Lambda+\mu_f(\phi)\end{aligned}\tag{D.2}$$

where $f=F/N$ is the basin negative log-volume per particle and $\lambda\equiv 1/\kappa$ is the slope of the power-law relation, which depends crucially on the packing fraction ϕ. The last equality in Eq. (D.2) highlights how $\lambda(\phi)$ controls the contributions of the fluctuations of the log-pressures $\Delta\Lambda\equiv\Lambda-\mu_{\Lambda}(\phi)$ to changes in the basin log-volume. Note that one can rewrite the ratio of fluctuations as $\sigma^2_{f\Lambda}/\sigma^2_{\Lambda}=\rho_{f\Lambda}\sigma_f/\sigma_{\Lambda}$ where $\rho_{f\Lambda}=\sigma^2_{f\Lambda}/(\sigma_f\sigma_{\Lambda})$ is the linear correlation coefficient of f and Λ. Finally, we can gain further insight into the power-law dependence by noting that

$$\lambda(\phi)\equiv\frac{\sigma^2_{f\Lambda}(\phi)}{\sigma^2_{\Lambda}(\phi)}\tag{D.3}$$

$$c(\phi)\equiv\mu_f(\phi)-\frac{\sigma^2_{f\Lambda}(\phi)}{\sigma^2_{\Lambda}(\phi)}\mu_{\Lambda}(\phi)\tag{D.4}$$

Appendix E

Data analysis

E.1 Generalised Gaussian

Assuming that the distribution of basins log-volumes $\mathcal{U}(F|N,\phi_{\mathrm{SS}})$ is unimodal, which has been verified for very small systems [32], one can fit the raw distribution $\mathcal{B}(F|N,\phi_{\mathrm{SS}})$ with a three-parameter generalised normal distribution [153, 154]

$$p(F|\mu_F,\sigma,\zeta) \equiv \frac{\zeta}{2\sigma\Gamma(1/\zeta)} \exp\left[-\left(\frac{|F-\mu_F|}{\sigma_F}\right)^{\zeta}\right], \tag{E.1}$$

where $\Gamma(x)$ is the gamma function, σ is the scale parameter, ζ is the shape parameter and $\mu_F = \langle F \rangle$ is the mean (dimensionless free energy) with variance $\sigma^2\Gamma(3/\zeta)/\Gamma(1/\zeta)$. In the limit $\zeta \to 2$ we recover the Gaussian distribution with standard deviation σ. In practice it appears to be most stable to fit the empirical biased cumulative distribution function, rather than the histogram shape [34]. Alternatively, we also tested fitting to the observed p.d.f. with the maximum-likelihood method, obtaining consistent, but more scattered, results (see Sec. 2.7).

E.2 Generalised log-normal

In Sec. 2.7.2 we have established a link between the pressure of a packing and the volume of its basin of attraction, see Eq. (2.20). In order to compute the entropy as a function of volume and pressure it is necessary to unbias the distribution of pressures with respect to the sampling bias $\exp(-F)$. We choose to describe the distribution of pressures P using the generalised log-normal distribution [231]

$$p(P|\mu_\Lambda,\sigma,\zeta) = \frac{\zeta/P}{2^{(\zeta+1)/\zeta}\sigma\Gamma(1/\zeta)} \exp\left(-\frac{1}{2}\left|\frac{\ln(P)-\mu_\Lambda}{\sigma}\right|^{\zeta}\right), \tag{E.2}$$

with the first term on the r.h.s. being the normalisation constant, $\Gamma(x)$ is the gamma function, σ is the scale parameter, ζ is the shape parameter and $\mu_\Lambda \equiv \langle \ln P \rangle$ is the mean. For $\zeta = 2$ this distribution reduces to the log-normal distribution.

E.3 Kernel density estimate

To relax the assumption that the empirical distributions can be fitted by a symmetric (generalised Gaussian) distribution, one can also describe the distributions by kernel density estimation (KDE) [181, 232]. A kernel $K(h;x)$ is a positive function controlled by the bandwidth parameter h, such that we can defined the KDE density as

$$p_{\text{KDE}}(h;x) = \frac{1}{Mh}\sum_{i=1}^{M} K\left(\frac{x-x_i}{h}\right) \tag{E.3}$$

where M is the sample size. The bandwidth acts as a smoothing parameter controlling the trade-off between bias and variance. In this work we choose the Gaussian kernel $K(h;x) \propto \exp[-x^2/(2h^2)]$. Bandwidth selection is then done using Silverman's rule of thumb as the initial guess for integrated squared error cross-validation [233]. The numerical integration step is performed, as for the generalised Gaussian description, via Eq. (2.17).

E.4 Distance based outlier detection

We remove outliers from a univariate, e.g. $\mathcal{B}(f)$, or bivariate distribution, e.g. $\mathcal{B}(f,\Lambda)$, following the distance-based outlier removal method introduced by Knorr and Ng [152]. This is applied in turn to each dimension, such that we choose to keep only those points for which at least $R = 0.5$ of the remaining data set is within $D = 3\sigma \vee 4\sigma$ (compared to the much stricter $R = 0.9988$, $D = 0.13\sigma$ required to exclude any points further than $|\mu - 3\sigma|$ for normally distributed data [152]). On our datasets we find that this procedure removes typically none and at most 0.8% of all data points.

E.5 Robust covariance estimator

Robust mean and covariance estimates of a multivariate distribution can be computed using the Minimum Covariance Determinant (MCD) estimator [232, 234] with e.g. support fraction $h/n_{\text{samples}} = 0.99$. The MCD estimator defines μ_{MCD}, the mean of the h observations for which the determinant of the covariance matrix is minimal, and $\hat{\sigma}_{\text{MCD}}$, the corresponding covariance matrix [235].

E.5.1 Elliptic envelope outlier detection

Outlier detection based on an elliptic (Gaussian) envelope criterion can be constructed using the MCD estimator. We assume a support fraction $h/n_{\text{samples}} = 0.99$ and a contamination equal to 10% [232].

E.6 Generalised sigmoid

We defined a generalised sigmoid function of the form:

$$f(a,b,\phi_0,u,w;\phi) = a - \frac{a-b}{\left(1+e^{-w(\phi-\phi_0)}\right)^{1/u}} \tag{E.4}$$

Appendix F

Connecting log-pressures to relative pressures

In this section we relate the statistics of the log-pressures of the packings to the *relative* pressures. For a given N and ϕ, with the set of pressures $\{P_i\}$, the log-pressures are given by $\Lambda_i \equiv \ln P_i$ and the relative pressures are $P_i/\langle P\rangle$. The two quantities are then simply related as

$$\ln\left(\frac{P_i}{\langle P\rangle}\right) = \ln P_i - \ln\langle P\rangle = \Lambda_i - \ln\langle P\rangle. \tag{F.1}$$

Using Jensen's inequality, we have the following bound for the first moment of the log-pressures

$$\langle\Lambda\rangle = \langle \ln P\rangle \leq \ln\langle P\rangle. \tag{F.2}$$

Therefore $\langle P\rangle \to 0$ implies $\langle\Lambda\rangle \to -\infty$.

F.1 Moments

In order to relate the means and the variances of P_i and $\Lambda_i \equiv \ln P_i$, we perform the Taylor expansion

$$\ln P = \ln\langle P\rangle + \left.\frac{d\ln P}{dP}\right|_{P=\langle P\rangle} (P - \langle P\rangle) + \ldots \tag{F.3}$$

We next compute the moments to leading order

$$\begin{aligned} \langle \ln P\rangle &\approx \ln\langle P\rangle, \\ \sigma^2(\ln P) &\approx \frac{\sigma^2(P)}{\langle P\rangle^2} = \sigma^2\left(\frac{P}{\langle P\rangle}\right). \end{aligned} \tag{F.4}$$

Thus, to first order, the variance of the log-pressures is equal to the variance of the relative pressures.

F.2 Bounds

For a fixed N and ϕ, the pressures of the individual packings are bounded as

$$0 < P_{\min} \leq P_i \leq P_{\max}. \tag{F.5}$$

where $P_{\max}$ and $P_{\min}$ are determined by the packing fraction ϕ, independent of system size, and are physically set limits [118, 174, 175]. We can therefore use Popoviciu's inequality on variances [236], yielding

$$\sigma^2(P) \leq \frac{1}{4}\left(P_{\max} - P_{\min}\right)^2, \tag{F.6}$$

which is also bounded. The relative pressure fluctuations are therefore bounded as

$$\sigma^2\left(\frac{P}{\langle P\rangle}\right) \leq \frac{1}{4}\frac{\left(P_{\max} - P_{\min}\right)^2}{\langle P\rangle^2}. \tag{F.7}$$

We thus find that the variance of the relative pressures $\sigma^2\left(\frac{P}{\langle P\rangle}\right)$ can diverge only when $\langle P\rangle \to 0$, which is precisely where the unjamming transition occurs.

Appendix G

Projection of volumetric density onto a reference surface

Let us defined $\nu_{\partial\gamma}(\boldsymbol{x})$ as the projection of the (uniform) density in $V_{\Gamma\backslash\gamma}$ onto a reference surface $\partial\gamma$, such that

$$\int_{\partial\gamma} \nu_{\partial\gamma}(\boldsymbol{x}) \mathrm{d}\sigma(\boldsymbol{x}) = \int_{\gamma} \rho(\boldsymbol{x},\infty) \mathrm{d}\boldsymbol{x}, \tag{G.1}$$

where we assume that the trajectories evolve according to Eq. (5.1) and $\rho(x,\infty)$ is determined by the continuity equation Eq. (5.2) subject to the initial condition Eq. (5.3).

Substituting the integral with respect to t of Eq. (5.2) for $\rho(\boldsymbol{x},\infty)$ in Eq. (G.1) and applying the divergence theorem gives

$$\begin{aligned} &\int_{\partial\gamma} \nu_{\partial\gamma}(\boldsymbol{x}) \mathrm{d}\sigma(\boldsymbol{x}) \\ &= \int_{\partial\gamma} \left[\int_0^\infty |\hat{\boldsymbol{n}}(\boldsymbol{x}) \cdot \boldsymbol{\nabla} U(\boldsymbol{x})| \rho(\boldsymbol{x},t) \mathrm{d}t \right] \mathrm{d}\sigma(\boldsymbol{x}) \\ &= \int_{\Gamma} \left[\int_0^\infty |\boldsymbol{\nabla} g(\boldsymbol{x}) \cdot \boldsymbol{\nabla} U(\boldsymbol{x})| \rho(\boldsymbol{x},t) \mathrm{d}t \right] \delta[g(\boldsymbol{x})] \mathrm{d}\boldsymbol{x}, \end{aligned} \tag{G.2}$$

where we have parametrized the reference region boundary $\partial\gamma = \{\boldsymbol{x} : g(\boldsymbol{x}) = 0\}$. Noting that

$$\rho(\boldsymbol{x},t) = \frac{1}{V_{\Gamma\backslash\gamma}} \int_{\Gamma\backslash\gamma} \delta[\boldsymbol{x} - \boldsymbol{X}(t,\boldsymbol{y})] \mathrm{d}\boldsymbol{y}, \tag{G.3}$$

Eq. (G.2) can be written as

$$\begin{aligned}
&\int_{\partial\gamma} \nu_{\partial\gamma}(\boldsymbol{x})\mathrm{d}\sigma(\boldsymbol{x}) \\
&= \frac{1}{V_{\Gamma\setminus\gamma}} \int_{\Gamma} \left\{ \int_0^\infty |\boldsymbol{\nabla} g(\boldsymbol{x}) \cdot \boldsymbol{\nabla} U(\boldsymbol{x})| \right. \\
&\qquad \left. \times \left[\int_{\Gamma\setminus\gamma} \delta[\boldsymbol{x} - \boldsymbol{X}(t,\boldsymbol{y})]\mathrm{d}\boldsymbol{y} \right] \mathrm{d}t \right\} \delta[g(\boldsymbol{x})]\mathrm{d}\boldsymbol{x} \\
&= \frac{1}{V_{\Gamma\setminus\gamma}} \int_0^\infty \int_{\Gamma\setminus\gamma} |\boldsymbol{\nabla} g[\boldsymbol{X}(t,\boldsymbol{y})] \cdot \boldsymbol{\nabla} U[\boldsymbol{X}(t,\boldsymbol{y})]| \\
&\qquad \times \delta\{g[\boldsymbol{X}(t,\boldsymbol{y})]\}\mathrm{d}\boldsymbol{y}\mathrm{d}t.
\end{aligned} \tag{G.4}$$

Making the change of variable $\boldsymbol{x} = \boldsymbol{X}(t,\boldsymbol{y})$ in Eq. (G.4) gives

$$\begin{aligned}
&\int_{\partial\gamma} \nu_{\partial\gamma}(\boldsymbol{x})\mathrm{d}\sigma(\boldsymbol{x}) \\
&= \frac{1}{V_{\Gamma\setminus\gamma}} \int_0^\infty \int_{\Gamma_t} |\boldsymbol{\nabla} g(\boldsymbol{x}) \cdot \boldsymbol{\nabla} U(\boldsymbol{x})| \delta[g(\boldsymbol{x})] \det\left[\frac{\partial \boldsymbol{y}}{\partial \boldsymbol{x}}\right] \mathrm{d}\boldsymbol{x}\mathrm{d}t,
\end{aligned} \tag{G.5}$$

where the region Γ_t is given by the mapping of $\Gamma \setminus \gamma$ via $\boldsymbol{X}(t,\cdot)$. Since $\partial\gamma \subset \Gamma_t$, we may use the Dirac delta function $\delta[g(\boldsymbol{x})]$ to re-express the volume integral over Γ_t as a surface integral over $\partial\gamma$. Noting also that $\boldsymbol{y} = \boldsymbol{X}(-t,\boldsymbol{x})$ if $\boldsymbol{x} = \boldsymbol{X}(t,\boldsymbol{y})$, and defining the Jacobian matrix $\mathrm{J}(\boldsymbol{x},t) \equiv \frac{\partial}{\partial \boldsymbol{x}}\boldsymbol{X}(-t,\boldsymbol{x})$, we get

$$\begin{aligned}
&\int_{\partial\gamma} \nu_{\partial\gamma}(\boldsymbol{x})\mathrm{d}\sigma(\boldsymbol{x}) \\
&= \int_{\partial\gamma} \left\{ \frac{1}{V_{\Gamma\setminus\gamma}} |\hat{\boldsymbol{n}}(\boldsymbol{x}) \cdot \boldsymbol{\nabla} U(\boldsymbol{x})| \int_0^\infty \det[\mathrm{J}(\boldsymbol{x},t)]\mathrm{d}t \right\} \mathrm{d}\sigma(\boldsymbol{x}).
\end{aligned} \tag{G.6}$$

Since the choice of the reference region γ is arbitrary, the integrands on both sides of Eq. (G.6) must be equal. This proves Eq. (5.4).